Investigation of Loss of Synchronism Phenomenon in Synchronous Machines and Protection Using Trajectory of Relative Speed

by

Kasun Chamara Samarawickrama

A Thesis submitted to the Faculty of Graduate and Postdoctoral Studies of

The University of Manitoba

in partial fulfillment of the requirements of the degree of

Doctor of Philosophy

Department of Electrical and Computer Engineering

University of Manitoba

Winnipeg

Abstract

The "loss of synchronism" condition in a synchronous machine is a critical state where the rotor fails to stay synchronized with the stator magnetic field. This can be caused by various factors, including system disturbances and power system instabilities. A machine undergoing a loss of synchronism may experiences torsional stresses, increased rotor iron currents and winding stresses in their mechanical systems. Synchronous machine loss of synchronism protection is employed to promptly disconnect a machine operating asynchronously to avoid damage or degradation.

This thesis explores the loss of synchronism phenomenon in synchronous generators and introduces a novel loss of synchronism detection method based on the estimated relative speed of the rotor. The proposed algorithm utilizes readily available terminal voltage, current and machine parameters to estimate the rotor speed following a disturbance. It identifies loss of synchronism condition if the estimated relative speed tends to increase during a swing cycle. This method is computationally simple, easy to implement, and faster than impedance-based techniques under certain conditions. The sensitivity and security of this method is evaluated through time-domain simulations under various power system conditions. The performance of the proposed method is also compared against well established loss of synchronism

protection schemes.

The occurrence of loss of synchronism in synchronous condensers has not been extensively studied, primarily due to its rarity in traditional power systems. However, with the increasing integration of inverter-based resources and associated grid issues, synchronous condensers have become more common. The literature indicates a considerable gap in understanding the loss of synchronism phenomenon in synchronous condensers, particularly under conditions where inverter-based resources dominate the power grid. This thesis examines the loss of synchronism phenomenon in synchronous condensers, including theoretical analysis using phasor diagrams of realistic scenarios. It also investigates the distinction between loss of synchronism and the pole slipping phenomenon, which has led to failures in traditional impedance-based schemes. The proposed relative speed-based method is applied to synchronous condensers and its effectiveness is demonstrated in situations where traditional schemes have failed.

Additionally, effectiveness of the proposed method in weak grids with a high penetration of inverter-based resources is analysed using a modified IEEE 39 bus system.

Acknowledgements

This thesis is an outcome of years of hard work. I may not have made it through without the support of some wonderful people. It's an honor for me to extend my warm acknowledgements to all of them at this point.

First, I would like to express my sincere gratitude to my advisor Dr. Athula Rajapakse for his constant moral support, invaluable guidance, and continuous encouragement throughout the research work. It was a great privilege to work under his supervision. I would also like to thank my co-advisor Dr. Nuwan Perera for his valuable suggestions and encouragement.

I wish to express my sincere gratitude to the advisory Committee members for their many helpful comments and feedback to improve the quality of the thesis. The technical and financial support received from Manitoba Hydro and Electranix Corperation is gratefully acknowledged.

Last but not least, I would like extend my extreme gratitude to my beloved parents for all their love and guidance throughout my life. Without them, I would not be the person who I am today. The biggest acknowledgement goes to my loving wife, Nisansala, and my children, Deeghayu and Sarala, for their patience, understanding, and encouragements whenever I most needed them.

Dedication

To my loving parents.

Contents

List of Tables

List of Figures

List of Abbreviations

$2LG$	Two Lines to Ground
$3LG$	Three Lines to Ground
$BESS$	Battery Energy Storage Systems
BRK	Breaker
CT	Current Transformer
$DFIG$	Doubly-Fed Induction Generator
DFT	Discrete Fourier Transformation
EHV	Extra High Voltage
EMT	Electromagnetic Transient
FRT	Fault Ride Through
GSC	Grid Side Converter
GSU	Generator Step-Up
HV	High Voltage
IBR	Inverter Based Resource
$IEEE$	Institute of Electrical and Electronics Engineers
$IGBT$	Insulated-Gate Bipolar Transistor
LG	Lines to Ground

LL	Line to Line
LOE	Loss of Excitation
$LVRT$	Low Voltage Ride Through
MSC	Machine Side Converter
OEM	Original Equipment Manufacture
P	Active Power
PI	Proportional-Integral
PLL	Phase Lock Loop
$PMSG$	Permanent Magnet Synchronous Generator
POI	Point of Interconnection
PPC	Power Plant Controller
$PSRC$	Power System Relaying Committee
PSS	Power System Stabilizers
PV	Photovoltaic
Q	Reactive Power
RMS	Root Mean Square
$ROCOV$	Rate of Change of Voltage
RSC	Rotor Side Converter
$SCMVA$	Short Circuit MVA
SCR	Short Circuit Ratio
SCV	Swing Center Voltage
SEL	Schweitzer Engineering Laboratories

$SMIB$	Single Machine Infinite Bus
SNR	Noise to Signal Ratio
VSC	Voltage Source Converters
VT	Voltage Transformer
WF	Wind Farm
WTG	Wind Turbine Generator

Chapter 1

Introduction

This chapter presents the background, motivation, and the major research objectives. A brief review of the loss of synchronism phenomenon, impedance relationship and different types of loss of synchronism protection schemes are also provided. It further explains the impact of loss of synchronism conditions on synchronous machines and emphasizes the importance of loss of synchronism protection. The chapter concludes with an overview of the organization of the thesis.

1.1 Background

Power systems subject to a broad range of disturbances due to various reasons such as lightning strikes, high wind/storms, equipment failures, human errors, system overloading. Large disturbances may cause disconnection of generation and loads impacting customers and consequently, the economy in general. Despite recent growth of Inverter Based resources (IBR), synchronous generators plays crucial role in elec-

tricity generation and stable operation of the power grids. Certain disturbances may cause oscillations in the power flow between a synchronous machine or a group of synchronous machines and the rest of the system or between two interconnected systems. These oscillating power flows are referred to as power swings. They result in fluctuating network voltages, and large oscillating power flows and consequent voltage instability or angular instability. Angular instability results in loss of synchronism of one or more synchronous machines. If a loss of synchronism occurs, the machines or the systems operating asynchronously must be separated immediately to avoid widespread outages and equipment damage [8]. To mitigate the effect of these disturbances, it is a common practice to provide controls and protection schemes. These schemes are designed to avoid voltage or angular instability and minimize the effects of the disturbance.

An effective mitigation method to contain such a disturbance leading to angular instability is through controlled separation of the system using loss of synchronism protection schemes. The controlled separation can be achieved by separating the system by tripping a transmission line(s) or by disconnecting a machine(s) from the system. Based on the electrical location of controlled separation, different loss of synchronism protection schemes are employed. i.e. if the swing centre (the location of a two-source equivalent system where the voltage value is zero when the angles between sources are 180° apart) places within the machine or step-up transformer impedance, machine loss of synchronism scheme takes the control action or if the swing centre occurs within a transmission line, line out-of-step scheme takes the control action. The focus of this research is mainly on synchronous machine loss

of synchronism protection, specifically those operating in generator or synchronous condenser mode.

When a machine loses its synchronism with the system, the voltages and currents oscillate at the slip frequency. Slip frequency is the difference between the frequency of the machine that lost the synchronism and the frequency of the rest of the power system. These oscillations produce pulsating torques, winding stresses and high rotor iron currents, which can be greater than a three-phase fault at the machine terminals [9]. All of these factors are potentially damaging the machine. Therefore, it is generally recommended that the machine be separated from the system without a delay.

In the 1970s, the rotating machinery subcommittee of the Power Systems Relaying Committee of the IEEE Power and Energy Society prepared a report on the need for and the methods of accomplishing synchronous machine loss of synchronism protection [8, 10–12]. As a result, a wide range of loss of synchronism protection schemes for synchronous machines have been developed. These include approaches based on impedance, rate of change of impedance, synchrophasor, equal area criterion, etc. Further details on existing methods and their pros and cons are discussed in Chapter 2. Since the settings for most conventional loss of synchronism protection schemes rely on both generator and system data, determining appropriate settings typically require complex procedures that rely on detailed time-domain simulations, a process that is both complex and time-consuming [13–15]. Thus, the development of easily configurable and accurate loss of synchronism protection methods to enhance reliability of power systems is required.

1.2 Loss of Synchronism

Loss of synchronism occurs when a synchronous generator is no longer able to maintain a constant angular position (or rotor angle) relative to the synchronous reference frame of the interconnected power system. This occurs due to a sustained imbalance between mechanical input and electrical output power, leading to instability as governed by the swing equation. The phenomenon is often referred to as loss of synchronism or out-of-step condition [16]. The terms loss of synchronism and out-of-step are used interchangeably throughout this thesis to refer same phenomenon.

However, pole slipping condition is different from loss of synchronism phenomena and terminologies cannot be used interchangeably even though they may occur around the same time in certain situations. Also it is important to note that loss of synchronism does not always result in pole slipping.

1.2.1 Impedance Relationship

An effective way to comprehend the loss of synchronism phenomenon is by analysing the impedance trajectory seen from the machine terminals. During a loss of synchronism condition, between a machine and the rest of the system or between two machines, the impedance seen at the machine terminal varies depending on the voltage and the angular difference between two systems. Appropriate protective devices calculate this variation of impedance to determine loss of synchronism [17–20].

The best way to illustrate this variation of impedance is by using a simple equivalent system consisting of two machines with internal voltages of $E_a\angle\delta_a$ and $E_b\angle\delta_b$

as shown in Figure 1.1. Assume that δ_b is lagging with respect to δ_a. The phasor relationship of the above system is shown in Figure 1.2.

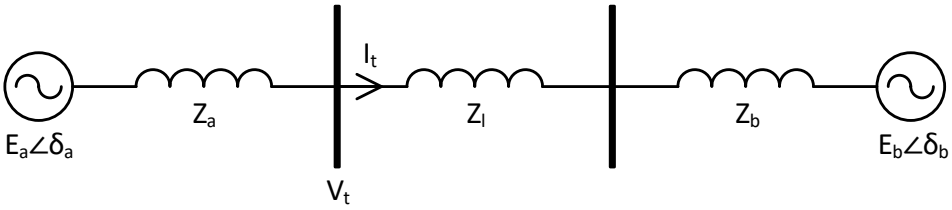

Figure 1.1: A simple equivalent system consisting of two synchronous machines

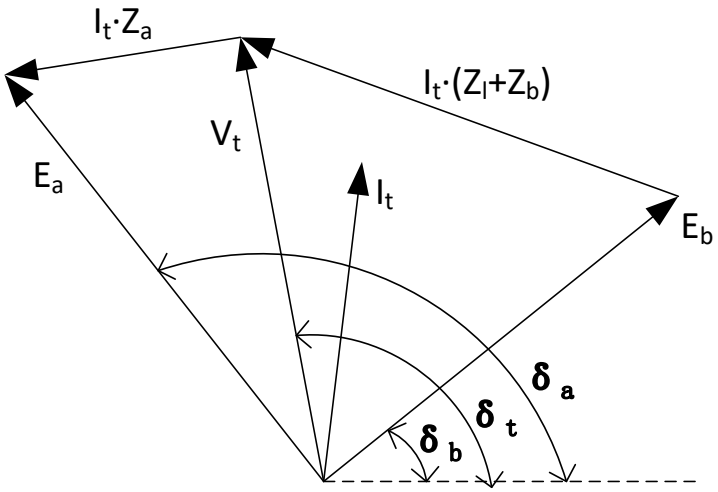

Figure 1.2: Voltage and current phasors of the system shown in Figure 1.1

The impedance seen by the relay at the generator-a terminals can be calculated as:

$$V_t = E_a - I_t \cdot Z_a = I_t \cdot (Z_l + Z_b) + E_b \tag{1.1}$$

$$Z_t = \frac{V_t}{I_t} = Z_l + Z_b + \frac{E_b}{I_t} \tag{1.2}$$

The voltage phasors shown in Figure 1.2 can be converted into impedance phasors by dividing by the current phasor I_t (see Figure 1.3).

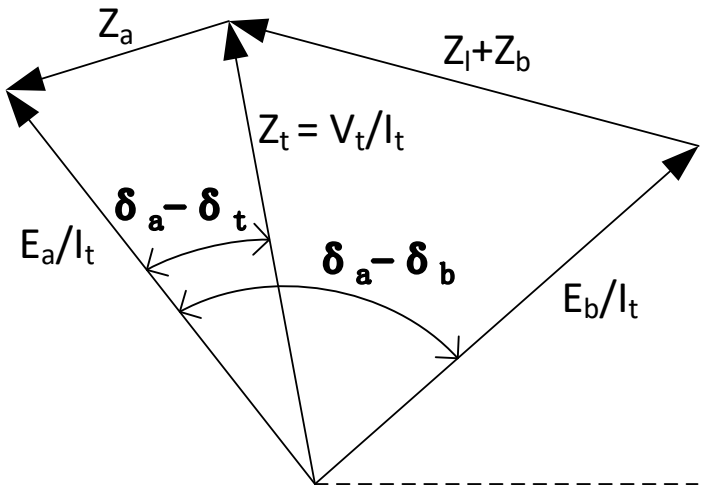

Figure 1.3: Impedance phasor relationship of the system shown in Figure 1.1

Let's place the impedance phasors of Figure 1.3 in real and imaginary axis plane (see $A-B-O-D-A$ in Figure 1.4). An oscillation may cause E_a and δ_a to change with respect to its reference. Hence, the terminal voltage (V_t), terminal current (I_t) and the vector V_t/I_t (AO) also vary w.r.t its steady state values.

If a severe disturbance occurs then the power angle δ ($\delta = \delta_a - \delta_t$) increases and the impedance seen by the relay will decrease to the value AO', increasing the angle $AO'D$. The locus of the impedance seen by the relay during an oscillation is a straight line if $|E_a| = |E_b|$, as shown in Figure 1.4. If $|E_a|$ is not equal to $|E_b|$, the impedance locus is a family of circles centred on the BD axis (the derivation of impedance loci for different $|E_a|/|E_b|$ ratios are provided in Chapter 4, Section 4.2.3). If the angle BOD increases to 120° and goes beyond, the system is not likely to recover, i.e. the

stability is likely to be lost. This can be determined more precisely with transient stability studies.

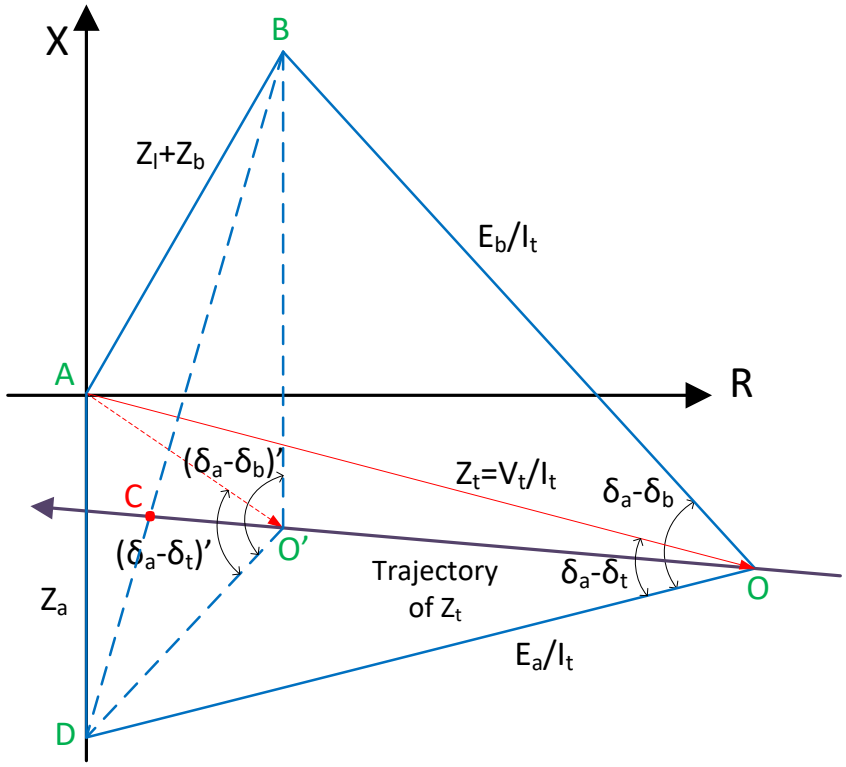

Figure 1.4: Impedance seen by the relay during a power swing plotted in the R-X plane

The point where the impedance locus intersects the total impedance line between B and D is called the electrical centre of the system (C in Figure 1.4). At this point, the two machines are 180° out of phase with each other. As the locus keeps moving to the left, the angular separation increases beyond 180°, thereafter the two systems become in-phase again. Once the two machines are back in-phase again with each other they have completed one slip cycle.

1.2.2 Power Angle Relationship

Another way to explain the loss of synchronism is by using the relationship between the generator active power output P and its power angle δ described in a Power Angle Curve as shown in Figure 1.5. Starting from $\delta = 0$, the power transferred increases as δ increases. The power transferred between two machines (in the system depicted in Figure 1.1) reaches the maximum value P_{max} when δ is 90°. After that point, further increase in δ will result in a decrease of power transfer. During normal operations of a generator without losses, the mechanical power P_0 from a prime mover is converted to the same amount of electrical power and transferred over the transmission line. The angle difference under this balanced normal operation is δ_0.

In general, a fault is modelled as a shunt impedance Z_f between the faulted point and the ground, as shown in Figure 1.6. Fault impedance Z_f can be found from the interconnection of sequence networks based on the fault type.

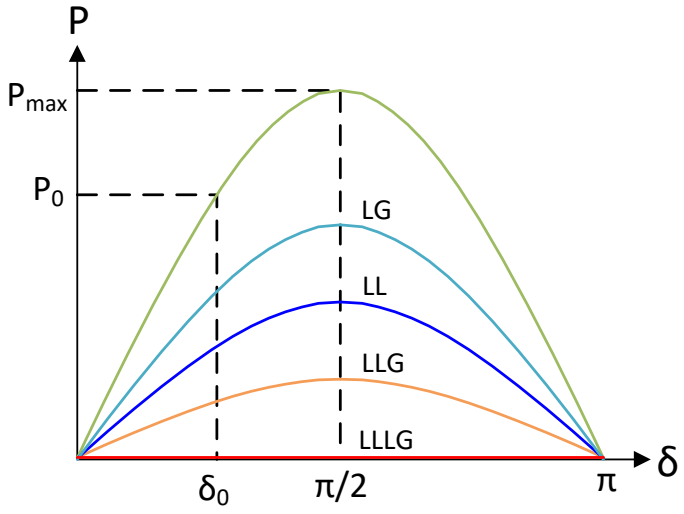

Figure 1.5: Power angle relationship of the system shown in Figure 1.6 for different types of faults

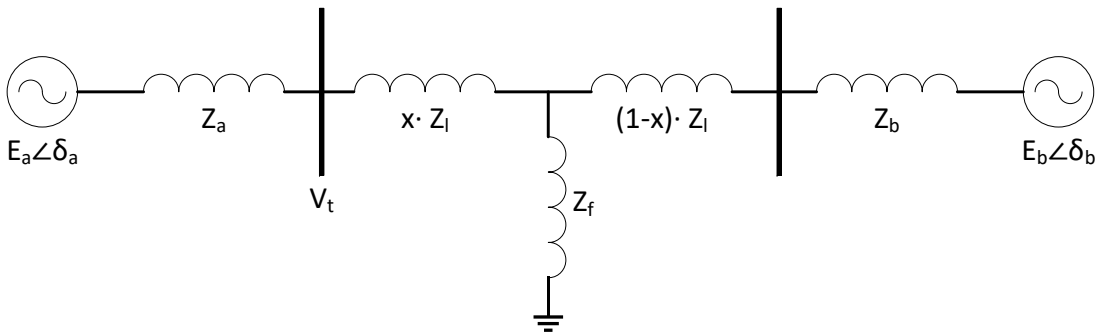

Figure 1.6: The equivalent system shown in Figure 1.1 with a fault on the transmission line between machine A and B at x per-unit distance from the machine A end

When a fault occurs on the transmission line at x per-unit distance from the machine A end, the effective impedance between the two machines will increase based on the type of fault in the system. Hence the amount of power transmission is reduced as shown in Figure 1.5. As a result, the electric torque that counters the mechanical torque is also decreased. If the mechanical power is not reduced during the period of the fault, the generator rotor will accelerate with a net surplus of torque input.

Assume that the equivalent two generator system in Figure 1.1 initially operates at a balance point of δ_0, transferring electric power P_0. After a fault, the power output is reduced to P_f, the generator rotor therefore starts to accelerate, and δ starts to increase. At the time that the fault is cleared when the angle difference reaches δ_c, there is decelerating torque acting on the rotor because the electric power output P_c at the angle δ_c is larger than the mechanical power input P_0. However, because of the inertia of the rotor system, the angle does not start to go back to δ_0 immediately. Rather, the angle continues to increase to δ_f when the energy lost during deceleration in area A2 is equal to the energy gained during acceleration in area A1. This is the

so-called equal-area criterion.

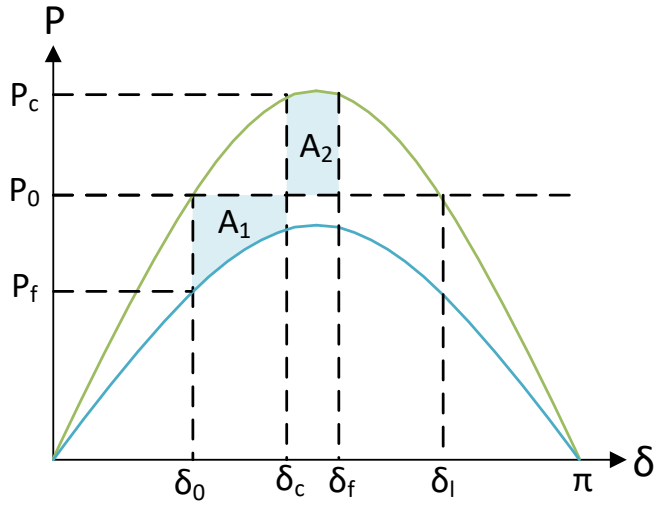

Figure 1.7: Power angle relationship of the system shown in Figure 1.6 for a stable power swing

If δ_f is smaller than δ_l, then the system is transiently stable as shown in Figure 1.7. With sufficient damping, the angle difference of the two generators eventually goes back to the original balance point δ_0. However, if area A2 is smaller than area A1 at the time the angle reaches δ_l, then further increase in angle δ will result in an electric power output that is smaller than the mechanical power input. Therefore, the rotor will accelerate again and δ will increase beyond recovery. This is a transiently unstable scenario, as shown in Figure 1.8. When an unstable condition exists in the power system, one equivalent generator rotates at a speed that is different from the other equivalent generator of the system. This condition is referred as a loss of synchronism or an out-of-step condition of the power system.

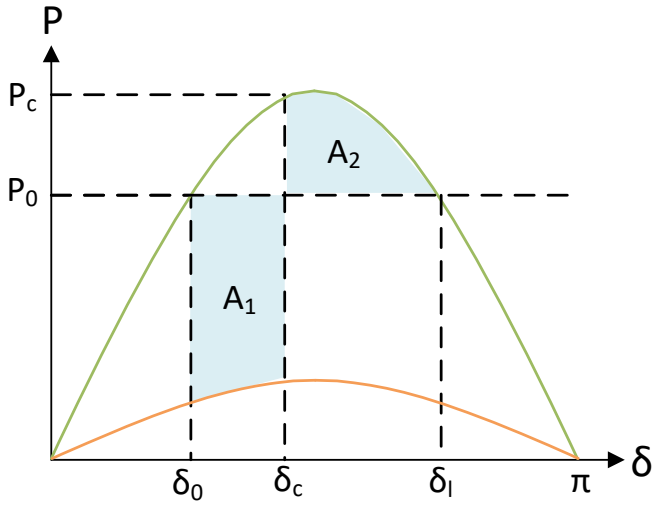

Figure 1.8: Power angle relationship of the system shown in Figure 1.6 for an unstable power swing

1.3 Effects on Synchronous Machines Operating in Loss of Synchronism

The synchronous machine is "synchronized" to the power system by closing its circuit breaker when the voltage, phase angle and frequency of the machine are within an acceptable tolerance to the same of the connecting system. In normal conditions, equilibrium exists between the prime mover mechanical power (in case of a generator), machine electrical power and their losses. Disturbances on the power system, such as faults, switching of lines, loads or generators can disrupt this equilibrium and may cause a loss of synchronism condition. Generally, a loss of synchronism condition occurs when the disturbance is so severe and the machine's mechanical system cannot respond fast enough to the changes of electrical system.

The loss of synchronism condition in synchronous machines causes torsional stresses

in its mechanical system (turbine-generator shaft in generators or flywheel-generator shaft in synchronous condensers) as the prime mover/flywheel tries to maintain synchronous speed with the electrical system. This can result in, pulsating torques, winding stresses and high rotor iron currents [9].

The pulsating torques occur because, as the machine swings past 180° relative to the system, the torque is negative and trying to decelerate the rotor to bring the prime mover/flywheel back into synchronism with the power system. As the machine swings past 0°, the torque changes to positive and trying to accelerate the rotor to bring the prime mover/flywheel back in phase with the system.

Winding stresses occur because, as the machine swings through 180° from the system, a 2 pu voltage is applied across the system and machine impedance. If the system impedance is smaller than the machine impedance (which is common in modern power systems), the magnitude of the current can be greater than the three-phase short circuit current. The synchronous machine and the transformer windings are not protected for currents greater than the short circuit level [8].

High rotor iron currents occur because the machine rotor slips relative to the system. These are similar to the currents induced in a squirrel cage of an induction motor. Since no squirrel cage is present in synchronous machines, these currents have to flow in the rotor iron, amortisseur (damper) windings as well as in the wedges of the rotor windings.

All of these effects are potentially damaging the synchronous machine. Therefore, it is recommended that the machine be separated from the system without a delay. In hydro generators and synchronous condensers, the system may have the possibility

to get back into synchronism after few swing cycles. Therefore, some generator and condenser owners take their unit offline only if it experiences a certain number of swing cycles.

1.4 Loss of Synchronism Protection

The principle behind loss of synchronism protection is quite clear: ensure that no power system components are tripped during stable swings, but protect the system during unstable or loss of synchronism conditions. When different areas or interconnected systems of a power system fall out of synchronism, it's essential to quickly and automatically isolate these areas to prevent damage to equipment and avoid major system outages. Uncontrolled tripping of circuit breakers during such conditions can lead to undesirable outcomes and pose safety risks to utility workers. Thus, controlled tripping of specific components is needed to avoid equipment damage, widespread outages, and to mitigate the impact of the disturbance.

Loss of synchronism protection can be divided into two categories: transmission line out-of-step protection and synchronous machine loss of synchronism protection. Each type comes with distinct challenges and requires tailored protection methods. Recognizing the differences between loss of synchronism conditions impacting transmission lines and those affecting machines is essential for ensuring the reliability of the power system.

1.4.1 Transmission Line Out-of-Step Protection

Out-of-step condition is classified as transmission line out-of-step if the swing center is located on a transmission line impedance rather than on a generator impedance (including Generator Step-Up (GSU) transformer). Essentially, this means that the loss of synchronism occurs between different segments of the power system that are linked by a transmission line. This typically happens during severe disturbances, such as faults or significant load or generation changes, leading to phase angle differences across the transmission line that are too large to be managed. Such loss of synchronism conditions are contained by separating the systems operating asynchronously by tripping a transmission line(s).

Loss of synchronism schemes specifically designed for line protection are typically employed in this scenario. They are generally employed in specific scenarios where the risk of loss of synchronism conditions is higher, but they are less frequently encountered compared to other protection methods due to the complexity and unique nature of such events in transmission lines. Some of the well established impedance based loss of synchronism protection schemes includes, single blinder, double blinder (vertical, quadrilateral, concentric circle) and mho circle. These protection schemes are not commonly used for tripping transmission line(s) but for loss of synchronism blocking feature of distance protection schemes.

This thesis does not cover the topic of line out-of-step protection.

1.4.2 Synchronous Machine Loss of Synchronism Protection

Prior to the interconnection of power systems, the electrical center during a loss of synchronism event was located within the transmission system. As a result, the impedance trajectory could easily be detected by line out-of-step relaying schemes, allowing the power system to be separated without tripping generators. However, with the introduction of High Voltage (HV) and Extra High Voltage (EHV) systems, large conductor-cooled generators, fast-response voltage regulators, and the expansion of transmission networks, generator and system impedances have undergone significant changes. Generator and step-up transformer impedances have increased, while system impedances have decreased. Consequently, the electrical center now often occur within or close to the generator or the step-up transformer, areas that are protected by differential relaying, which does not detect power swings. Therefore, adequate machine loss of synchronism protection schemes are essential for today's power system to disconnect the machines undergo loss of synchronism conditions.

Figure 1.9 illustrates the impedance trajectories of unstable power swings obtained using the simple equivalent network represented in Figure 1.1 for three different machine to system impedance ratios. The trajectories were calculated using (1.3) which was derived for the equivalent network in terms of voltages and impedances (derivation of (1.3) is presented in Chapter 4, Section 4.2.3). The voltage magnitudes of the two generators were assumed constant during the power swing. As shown, the circle formed by the impedance locus increases in diameter, and the electrical centre moves away from the generator impedance region into system impedance region as

the system impedance increases.

$$Z_t(k,\delta) = \frac{Z_a + Z_l + Z_b}{1 - \frac{1}{k\angle\delta}} - Z_a \tag{1.3}$$

where;

$$k = E_a/E_b \tag{1.4}$$

$$\delta = \delta_a - \delta_b \tag{1.5}$$

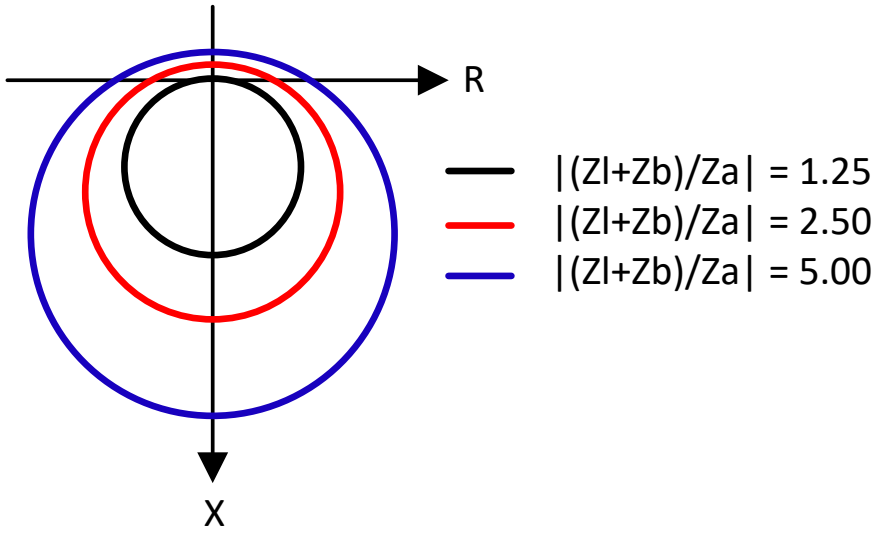

Figure 1.9: Impedance trajectories for different system to machine impedance ratio of the simple equivalent network represented in Figure 1.1

1.5 Motivation

Typical unit protection schemes, such as differential, restricted earth fault (REF), distance protection with directional element or general protection methods, such as over/under voltage, over current and over/under frequency relays will not protect a synchronous machine during a loss of synchronism condition. The loss of excitation relay may provide some degree of protection but can not be relied on to detect loss of

synchronism condition under all system considerations. Therefore, loss of synchronism relay is introduced to separate the machine from the system during loss of synchronism events [21].

The common challenge for most of the existing loss of synchronism protection schemes is that the complex setting calculation procedures. Relay manufacturers usually suggest a method for making preliminary settings. These preliminary settings cannot be relied upon without validating them using a transient stability study. Since sufficient system information to properly set this relay is seldom available, the protection engineer may have to rely on these preliminary settings. The lack of system information makes it difficult to determine how closely these settings are matching to the optimum values or if the preliminary settings accomplish the desired result [16].

Further, these preliminary settings may deviate from their optimum values when the system has a high penetration of inverter-based resources (IBRs) such as wind, photovoltaic (PV), and battery energy storage systems (BESS). The trajectory of impedance and its speeds may affected by the controlling effect of IBRs, hence preliminary settings may affect.

Therefore, the primary motivation of this research is to introduce an easily settable (or setting free) loss of synchronism scheme to protect the synchronous generators and synchronous condensers during a loss of synchronism event. The loss of synchronism phenomenon is directly related to the rotor angle of the machine concerned. Therefore a method based on the rotor angle or its rate of change, which is directly related to the speed of rotation, is likely to result in a setting free or easily settable algorithm.

Furthermore, the literature reveals a significant gap in understanding the loss

of synchronism phenomenon in synchronous condensers, especially in systems where IBRs dominate the power grid. The integration of IBRs, known for their rapid control response and low inertia, has introduced new dynamics and complexities that traditional systems have not previously faced. This highlights the need for further research to effectively predict and manage loss of synchronism events in grids with a high presence of IBRs. Thus, another key motivation of this research is to provide a comprehensive analysis of loss of synchronism conditions in synchronous condensers within systems with high penetration of IBRs.

1.6 Objectives and Contributions

The primary goal of this research is to develop a machine loss of synchronism protection scheme that is either easily configurable or requires no manual settings. Additionally, a key aim of this study is to gain a deeper understanding of the loss of synchronism phenomenon in synchronous condensers within power systems that have a high penetration of IBRs.

The key contributions of the research include:

1. Development of a loss of synchronism protection scheme for synchronous machines using their rotor speed. This involves developing two algorithms: one for estimating rotational speed using terminal measurements and machine parameters and another for detecting loss of synchronism conditions using the estimated rotor speed.

2. Validation of the above proposed algorithms using detailed time domain sim-

ulations. This includes the analysis of sensitivity and security of the proposed method for various influencing factors such as generator configuration, measurement errors, system faults, small disturbances, etc. and comparison of performance of the proposed method against well established and promising new methods.

3. Investigation of applicability of the proposed method for loss of synchronism protection in weak grids with high penetration of inverter based generation.

4. Analysis of the loss of synchronism phenomenon in synchronous condensers and clarification of the loss of synchronism and pole slipping phenomenons.

5. Application of the above proposed method for loss of synchronism protection of synchronous condensers and validation of its performance by comparing against well established methods.

1.7 Thesis Overview

This chapter provides the introduction giving necessary background to the research, motivation, and key objectives. The rest of the thesis is organized as follows.

Chapter 2 presents a literature review on loss of synchronism protection for synchronous machines. It discusses well-established protection schemes currently in use, along with innovative methods introduced in recent studies. The review covers loss of synchronism protection of both synchronous generators and synchronous condensers.

Chapter 3 presents the proposed loss of synchronism protection scheme, emphasiz-

ing two main algorithms: the relative speed estimation algorithm and the loss of synchronism detection algorithm. It includes the implementation of the proposed scheme in an electromagnetic transient (EMT) program along with other well-established and innovative protection methods. Additionally, this chapter examines the sensitivity and security of the proposed approach under various influencing factors. A comprehensive performance comparison is provided, evaluating the proposed method against well-established and innovative protection techniques.

Chapter 4 explores the loss of synchronism phenomenon in synchronous condensers and the underlying theory using phasor diagrams of realistic scenarios. It analyses the impedance trajectory under various power system conditions and discusses the distinction between loss of synchronism and pole slipping, particularly in the presence of IBRs. The proposed loss of synchronism protection scheme is applied to synchronous condensers, and its performance is assessed by comparing it to other protection schemes using detailed time domain simulations.

Chapter 5 presents a case study conducted to evaluate the performance of the proposed method in weak grids with high penetration of IBRs using a modified IEEE 39 bus system. Two IBR integration levels which covers 200 simulation scenarios are included in the study scope.

Finally, a summary of the thesis, major conclusions, key contributions and future works are provided in Chapter 6.

Chapter 2

Loss of Synchronism Protection of Synchronous Machines

2.1 Introduction

This chapter reviews several traditional and novel loss of synchronism protection schemes used for both synchronous generators and synchronous condensers. The advantages and disadvantages of traditional protection methods are also discussed in this chapter.

2.2 Synchronous Generator Loss of Synchronism Protection

A variety of loss of synchronism protection schemes have been developed for synchronous generators, including well established traditional methods, as well as innova-

tive emerging techniques that show potential for enhanced performance and reliability. Some of these methods are discussed in section 2.2.1 and 2.2.2.

2.2.1 Traditional Generator Loss of Synchronism Protection Schemes

The conventional method for detecting a loss of synchronism condition involves analyzing the impedance trajectory observed at the generator's terminals. During a loss of synchronism condition, the impedance varies based on the voltage and the angular difference between the generator and the system.

When the two systems are in phase with each other (i.e. the angular difference between two systems is zero), the voltage at the generator terminal will be at a maximum and the current will be at a minimum. However, when the two systems are perfectly out of phase with each other (i.e. 180° apart), the voltage at the terminals of the generator will be at a minimum and the current will be at a maximum. Appropriate protective devices and the associated logic measure this variation of voltages and currents to determine the loss of synchronism condition [22, 23]. Few key traditional loss of synchronism protection schemes are discussed below.

Loss of Excitation Relaying

Although loss of excitation (LOE) relaying is applied primarily to protect the generator under a loss of excitation condition, this impedance based scheme can be used to detect a loss of synchronism condition under certain circumstances [10, 24]. The typical characteristics of a commonly used LOE relay is shown in Figure 2.1.

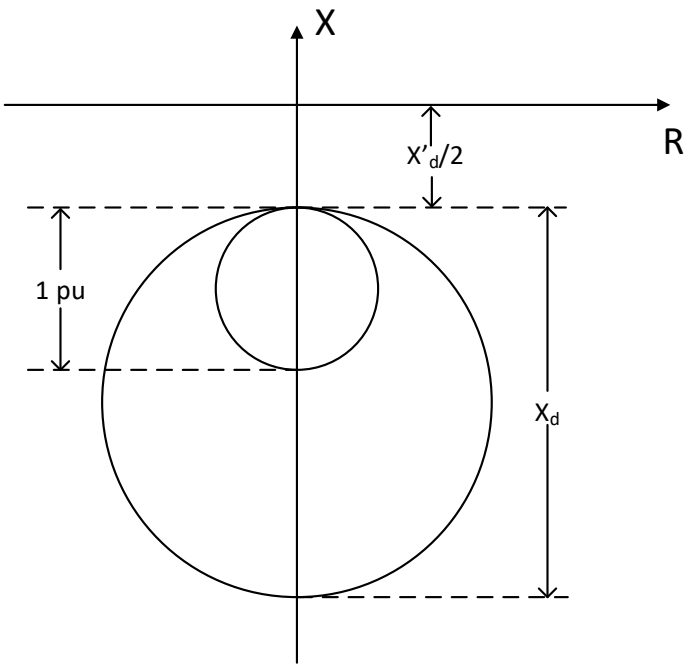

Figure 2.1: Generator loss of synchronism protection using LOE relay

The LOE characteristic is set with a time delay to ride through stable swings and system transients. The schemes will operate for impedances that stay within their operating characteristics longer than their time delay setting.

Mho Scheme

This scheme uses a standard distance relay (a Mho circle with no offset). Generally, the impedance look into the generator is calculated using the current and voltage measurements at the high side of the generator step-up transformer (GSU). The relay will immediately trip if the swing impedance enters the relay characteristic circle. This scheme also protects the generator from unintentional energization and also provide back up protection for multiphase faults in the generator and GSU. Figure 2.2 shows a typical Mho scheme.

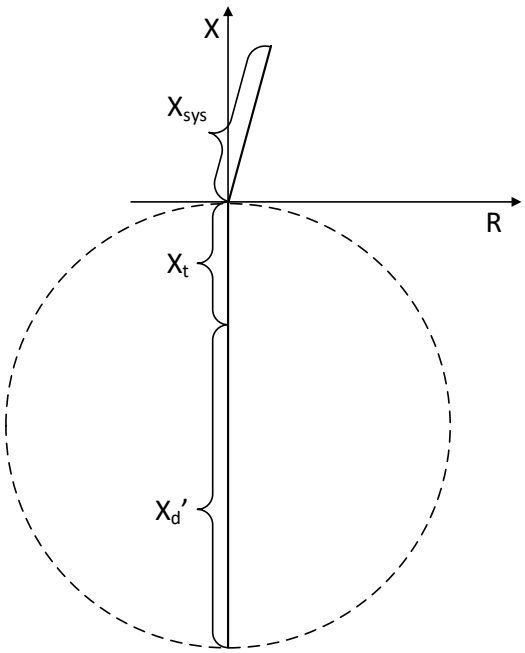

Figure 2.2: Generator loss of synchronism protection using Mho scheme

Single Blinder Scheme

This particular function uses one pair of blinders along with a supervisory offset Mho element as shown in Figure 2.3. The operating area is restricted to the region between blinders within the Mho circle (the hatched area in Figure 2.3). The positive sequence impedance must start outside of both blinders and then enter and remain within the operating area for a time greater than the time delay to pick up the trip signal. If these requirements are satisfied, then the trip signal is issued when the positive sequence impedance leaves the opposite blinder or supervisory Mho circle (i.e if the impedance enter through right blinder ($R1$) and leaves through the left blinder ($-R$) then the trip signal will be issued at either left blinder (location B) or at the exit of the mho circle (location C)) [25]. This scheme is secure against false

trips because the trip condition is only declared after the swing has already passed the exit blinder (beyond 180°), i.e. stable recovery is not possible.

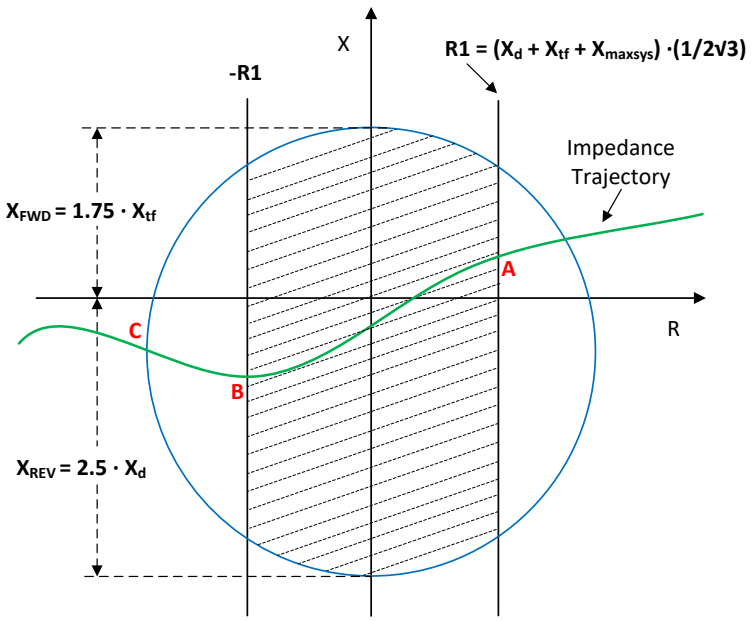

Figure 2.3: Generator loss of synchronism protection using single blinder scheme

Double Blinder Scheme

This is an extension of the single blinder scheme described above. In this scheme, there are two blinders on each side of the resistance axis in the R-X plane. Typically the two blinders on the left-half plane are the mirror images of those on the right-half plane. If the time spent between outer and inner blinders (R_o and R_i) is longer than the time delay setting, the scheme interprets the event as a loss of synchronism condition.

The scheme logic is initiated when the swing locus crosses the outer blinder R_o, at a separation angle of δ_1 as shown in Figure 2.4. The scheme only commits to take any action when the swing locus crosses the inner blinder R_i. At this point, the scheme

logic makes the loss of synchronism trip decision at a separation angle of δ_2. The swing may leave both inner and outer blinders in either direction and tripping will take place as the impedance locus leaves the supervisory Mho circle (in Figure 2.4, the relay trips at a separation angle of δ_3). Therefore, the inner blinder must be set such that the separation angle δ_2 is large enough that the system cannot recover.

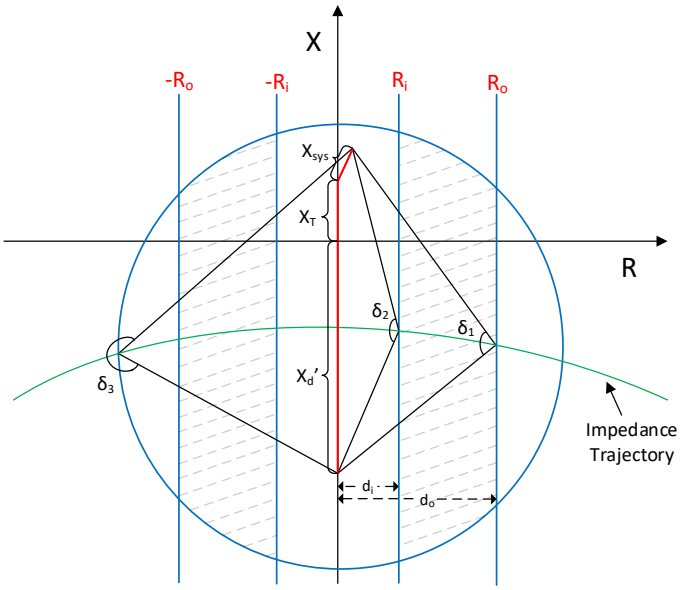

Figure 2.4: Generator loss of synchronism protection using double blinder scheme

Double Lens Scheme

In the double lens scheme, the outer impedance characteristic is concentric around the inner one. This is typically accomplished with either two additional characteristics, which are used specifically for the power swing function, or with an additional outer impedance characteristic that is concentric around one of the existing distance protection characteristics. A supervisory mho element is included in the double lens scheme to obtain further security.

As shown in Figure 2.5, the outer element operates when the swing impedance enters its characteristic. If the measured impedance remains between the outer and inner lenses (between L_o and L_i) for a period longer than the time delay setting, the scheme recognize this as an unstable condition. Once the swing has been detected and the impedance has entered the inner characteristic, the swing can now leave the inner and outer lenses in either direction and tripping will take place at the exit of Mho circle or outer lens. Therefore, the inner element must be selected in such a way that it will respond only to unstable swings.

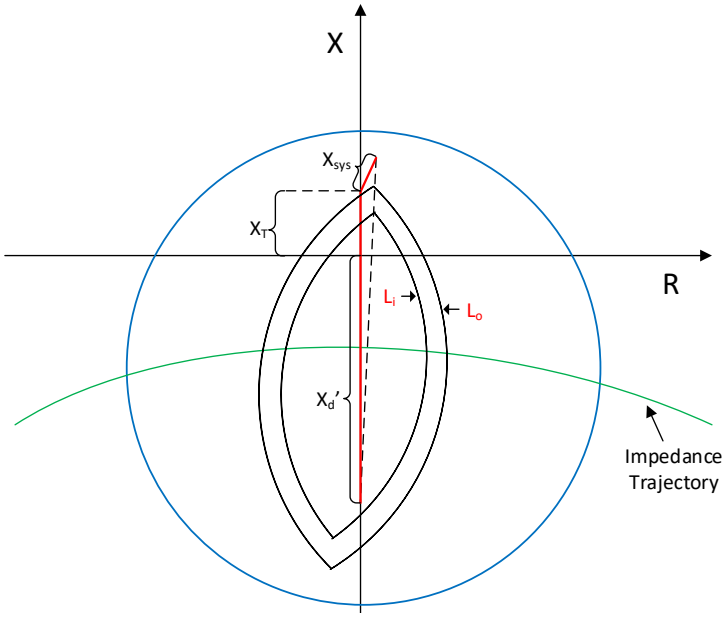

Figure 2.5: Generator loss of synchronism protection using double lens scheme

Triple Lens Schemes

The triple lens scheme is an extension of the double lens scheme but somewhat increased flexibility and complexity. The impedance elements are set in conjunction with several timers that represent the separation angle difference between inner, mid-

dle, and outer characteristic at the maximum expected swing rate. Depending on the setting for each characteristic, the actual shape may be a lens, circle, or tomato [11].

The outer element operates when the swing impedance enters its characteristic. If the swing impedance remains between the outer and middle characteristics for a period longer than a delay time of t_1, it is recognized as a power swing condition and loss of synchronism blocking asserts. As the swing impedance proceeds from the middle to inner characteristic in a period longer than a delay time of t_2 (t_1 also having expired), then enters the inner characteristic and remains there for a period at least longer than a delay time of t_3, then the trip decision is made. If an "early" trip mode is set, the trip is executed. If a "delayed" trip mode is set, the trip is not executed until the impedance leaves the outer characteristic after having spent at least t_4 delay time between the inner and outer characteristics.

Figure 2.6 illustrates the impedance elements of the triple lens loss of synchronism scheme. The separation angles δ_1 to δ_3 (outer, middle, inner lenses respectively) are similar to the double lens scheme.

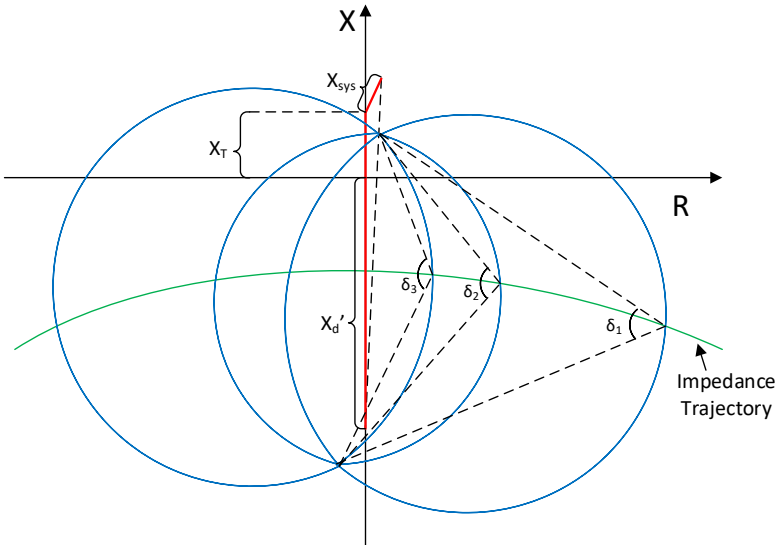

Figure 2.6: Generator loss of synchronism protection using triple lens scheme

Concentric Circle Scheme

The concentric circle loss of synchronism scheme is similar to the double lens scheme. In fact, it uses two concentric circles instead of two blinders or lenses. The operation and setting calculation is similar to the double blinder scheme. The inner circle may either be part of the loss of synchronism characteristic or the outermost distance element. The concentric circle scheme is more commonly implemented for electromechanical relay schemes, but occasionally may also be used in electronic or older microprocessor relays. The concentric circle scheme is more commonly used for loss of synchronism blocking, but can also be used for tripping with additional logic [8]. The concentric circle scheme is illustrated in Figure 2.7.

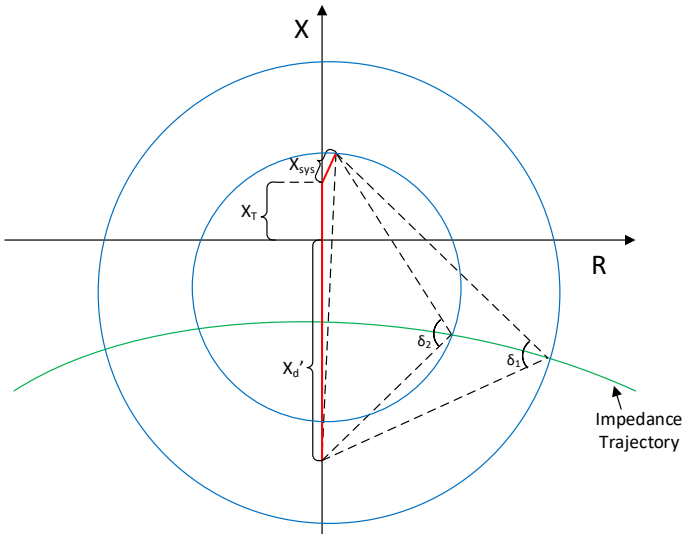

Figure 2.7: Generator loss of synchronism protection using concentric circle scheme

2.2.2 Novel Loss of Synchronism Protection Schemes

There are several novel loss of synchronism protection schemes introduced for transmission line protection and can be used for generator protection application in the future [8]. Most of these schemes are still in the research level and only a few methods have implemented by major commercial relay manufactures. As an example, Schweitzer Engineering Laboratories (SEL) has implemented rate of change of swing center voltage scheme in their transmission line protection relay [26]. Three key novel algorithms are discussed below.

Rate of Change of Swing Center Voltage Scheme

Swing Center Voltage (SCV) is defined as the voltage at the location of a two-source equivalent system (Figure 1.1) where the voltage value is zero when the angles between two sources are 180° apart. When a two-source system loses its stability

and goes into a loss of synchronism condition, the angle difference of the two sources (δ) will increase as a function of time [27]. Figure 2.8 illustrates the voltage phasor diagram of a general two source system with swing centre voltage.

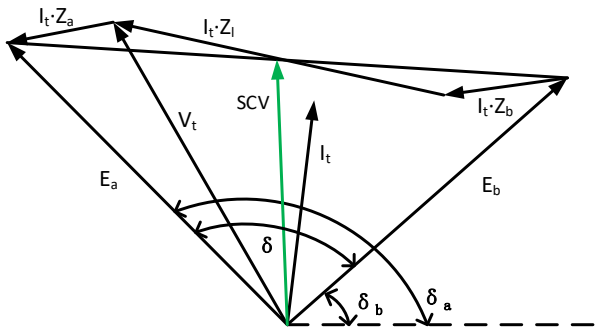

Figure 2.8: Swing centre voltage of a two-source equivalent system

For a homogeneous system with the system impedance angle close to 90°, and source voltage at each end are equal, i.e. $E_a = E_b = E$, an approximation of swing centre voltage can be written as follows;

$$SCV = E \cdot cos(\frac{\delta}{2}) \tag{2.1}$$

The absolute value of the SCV is at its maximum when the angle between two sources is zero, and this value is at its minimum (or zero) when the angle is 180°. This property has been exploited to detect a power swing by looking at the rate of change of SCV. The time derivative of SCV then becomes the following:

$$\frac{d(SCV)}{dt} = -\frac{E}{2} \cdot sin(\frac{\delta}{2}) \cdot \frac{d\delta}{dt} \tag{2.2}$$

The derivative of SCV is not dependant on the network impedance and that it reaches its maximum when the angle between two machines is 180° and zero when the angle between two machines is zero. Therefore, detection of loss of synchronism condition is straightforward by analyzing the rate of change of SCV [8].

Rate of Change of Resistance (Rdot) Scheme

This technique uses the apparent resistance and its rate of change to detect a loss of synchronism condition [28], [29]. The operating characteristics of the Rdot relay is given by;

$$(R - R_1) + T_1 \cdot \dot{R} \leq 0 \tag{2.3}$$

R is the apparent resistance measured by the relay and $\dot{R}$ is the rate of change of it. R_1 and T_1 are relay-setting parameters. The above characteristic of the Rdot relay can be visualized in the R-Rdot plane as shown in Figure 2.9. Rdot relay operates when the power swing trajectory crosses the Rdot characteristic defined in (2.3).

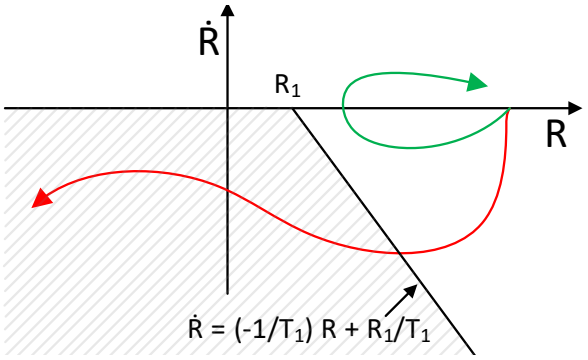

Figure 2.9: Generator loss of synchronism protection using Rdot scheme

Rate of Change of Impedance Scheme

In this algorithm, the impedance is calculated in each time step and compared with the previous time step value. When a considerable variation detected in the calculated impedance, a loss of synchronism situation is assumed. The next impedance that should be calculated in the next time step is predicted based on the impedance difference of the previously measured impedances. If the prediction is correct, then it is proven that this is a travelling impedance (i.e. towards unstable direction) and power swing condition is declared [8].

In this method, a delta impedance setting is not required, because the algorithm automatically considers any delta impedance that is measured between two consecutive calculations and sets the delta impedance for the next calculation. This leads to a dynamic calculation of the delta impedance and an automatic adaptation to the change of the power swing impedance. Also, the delta time setting is also not required because it is determined by the calculation time step of the algorithm.

2.2.3 Pros and Cons of Traditional Methods

This section discusses about pros and cons of traditional loss of synchronism protection schemes for synchronous generators and highlight the need of a new loss of synchronism protection scheme.

The LOE scheme discussed in section 2.2.1 measures the impedance looking into the generator, therefore it cannot detect swings passing through the GSU. The offset of LOE scheme in Figure 2.1 will also preclude the detection of swings within the

generator but close to its terminals. Because of these limitations, this scheme cannot be relied upon to protect the generator against all loss of synchronism conditions. With the introduction of new and better schemes, LOE scheme for loss of synchronism protection is considered as a legacy scheme.

In the Mho scheme discussed in section 2.2.1, the relay is normally set to see the generator transient reactance ($X_d{}'$) plus the GSU impedance (X_t). This setting would not detect slow moving swings where the generator synchronous reactance (X_d) would be the appropriate model. Further, this scheme is usually implemented in electromechanical relays. Such relays often provide minimal useful diagnostic information. A separate disturbance/event recorder may be necessary to determine the event characteristics, which can then be analyzed to determine the actual cause of a trip. The Mho scheme is also considered as a legacy scheme in loss of synchronism protection.

The blinder, lens and concentric circle schemes discussed in Section 2.2.1 provides reliable protection but requires extensive simulation studies for setting the blinders or lens. These schemes actuate only for non-recoverable swings which pass through the generator or GSU. Since these schemes use several timers for added security, calculation of settings is complex.

A scheme utilizing the rate of change of swing center voltage (SCV) is discussed in section 2.2.2. The major disadvantage of this scheme is that the approximation used in the calculation of SCV is valid only for the system impedance angle close to 90°. As discussed, SCV is estimated using (2.1) which assumes equal source voltages and that the SCV phasor is perpendicular to the $E_a - E_b$ phasor - conditions that hold only when the system impedance angle is 90°. Consequently, deviations from

this angle result in increased error in the estimated SCV.

Section 2.2.2 also discuss about a rate of change of resistance (Rdot) and rate of change of impedance based schemes, where the terminal resistance or impedance and its rate of change is use to detect an unstable swing. These schemes cannot control the angular separation at which the trip signal is issued.

Several equal area criteria based schemes are discussed in [30–37]. An adaptive scheme described in [32] uses wide area measurement and computes the post disturbance power angle when any major element in the system is tripped. This scheme requires measuring and communication equipment at all important locations in the system. The scheme described in [33, 34] detects an unstable swing by monitoring the reactive power, real power and rate of change of real power. The setting of the rate of change of real power threshold is based on the maximum slip frequency and hence requires extensive simulation studies. The scheme discussed in [35] measures the total area under the power vs time curve during the first swing cycle and initiates tripping when the total area is less than or equal to zero.

A loss of synchronism detection technique using the angular velocity and acceleration of the terminal voltage is described in [38]. Tripping is issued by monitoring the angular velocity at the instant where the acceleration crosses over from a negative to a positive value.

Reference [39] discusses a scheme similar to [38] but uses speed deviation and power deviation. For the swing to be stable, the speed deviation should be negative at the instant where the power deviation becomes positive.

A state plane approach for detecting a loss of synchronism condition is discussed

in [21]. It detects an unstable swing based on the computation of critical clearing time. The calculation of critical clearing time is based on the state plane trajectory analysis. This scheme detects a loss of synchronism condition by monitoring the fault clearing time and comparing it with the critical clearing time.

The scheme discussed in [35] and [39] detects a loss of synchronism condition when the post fault electrical power is above the mechanical power input to the generator.

All the schemes discussed in [21, 33–35, 38, 39] have the disadvantage that the separation angle at which tripping is issued cannot be adjusted. This is a critical point if the breaker is not designed for loss of synchronism duty. The ability of above schemes to allow few pole slips intentionally has not been discussed. Further, these schemes cannot distinguish the difference between a swing passing through the generator and the system.

A flux-based method for loss of synchronism protection of synchronous generators is described in [40]. The angular velocity and acceleration calculated from the measured magnetic flux are used to detect the loss of synchronism condition. The trip signal is issued at the point where the polarity of the angular acceleration changes from a negative to a positive value and the angular velocity is greater than the rated value. The main drawback of this method is the requirement of physical sensors to measure the stator magnetic flux.

Reference [41] introduces a method that uses wavelet transform to detect power swings as well as faults during a power swings. The major disadvantage of this scheme is that high computational cost.

Overall, above methods have demonstrated shortcomings in detecting loss of syn-

chronism condition of a synchronous generator. These shortcomings highlight the pressing need for the development of a novel approach to address this challenge.

2.3 Synchronous Condenser Loss of Synchronism Protection

Currently, only a limited number of loss of synchronism protection schemes have been designed for synchronous condensers, relying on measured terminal parameters, machine characteristics, and system data. These include well-established impedance-based approaches as well as techniques based on field or phase currents. Section 2.3.1 provides an overview of some of these methods, while Section 2.3.2 elaborates on their advantages and disadvantages. Section 2.3.3 emphasizes the gaps in the literature regarding the understanding of the loss of synchronism phenomenon in synchronous condensers, especially in scenarios where inverter-based resources (IBRs) play a dominant role in the power grid.

2.3.1 Traditional Synchronous Condenser Loss of Synchronism Protection Schemes

A widely recognized and commonly used loss of synchronism relay operates based on the positive-sequence impedance measured at the terminals of the synchronous condenser [8, 42]. This approach is also employed to detect loss of synchronism conditions in both transmission and generation systems. Consequently, various imple-

mentations exist, including Mho circles, vertical blinders, lenses, and concentric circles [1, 8, 10, 11, 24, 25]. These are examined in detail in above Section 2.2.1 under generator loss of synchronism protection. Furthermore, several other conventional loss of synchronism schemes for synchronous condensers are discussed below.

Notch Filter Scheme

Notching relay [43] is another commonly used loss of synchronism detection scheme for Synchronous Condensers. Under normal operating conditions, the field current of synchronous machines is a pure dc signal. Power swings introduce an ac component that in many cases causes the field current to exceed certain threshold setting. Notching relays are configured to count these instances and operate if a maximum number is reached within a given time [44]. Notching relays may also operate on the reactive power because it exhibits a similar behaviour as the field current. In this case, a special attention is paid to the filtering used in computing the reactive power [43].

Field AC Overcurrent Scheme

Field AC over-current element described in [44, 45] uses a similar technique as to notching relay. Instead of counting the swing cycles, field AC over-current element use a high or band pass filter to remove the dc component from the field current and operate based on the AC content.

Phase Overcurrent Scheme

Phase over-current elements have also been used in many application to detect a loss of synchronism condition. Loss of synchronism conditions are usually associated with currents that are well above those at the desirable operating condition. Overcurrent elements are effective in detecting those conditions [45, 46].

Speed Measurement Scheme

By directly monitoring the rotational speed of the shaft and the power system frequency, loss of synchronism conditions can be determined [47]. This is typically implemented as an over speed protection scheme where measured rotor speed to be exceeded a threshold speed limit.

2.3.2 Pros and Cons of Traditional Methods

This section discusses about pros and cons of traditional loss of synchronism protection schemes for synchronous condensers and highlight the need of a novel loss of synchronism protection scheme.

As discussed in Section 2.2.3, Mho scheme would not detect slow moving swings, where the synchronous reactance (X_d) would be the appropriate model as oppose to transient reactance ($X_d{}'$). The blinder, lens and concentric circle schemes provides reliable protection but calculating settings for these schemes is more challenging and requires detailed dynamic simulations incorporating both machine and the system data [13–15].

Compared to positive-sequence impedance methods above, notching relays are at a disadvantage as they only operate after a certain number of pole slipping events have happened. Similar to notching relay, field ac overcurrent methods also have the disadvantage that they only operate after a certain number of pole slipping events have happened.

The main drawback of speed measurement scheme is the requirement of physical sensors to measure the rotor speed. Proper filtering is also required in this method due to high signal to noise ratio of the measured signal.

Phase overcurrent is a straightforward scheme to configure. However, it cannot distinguish between stable and unstable power swings as the operating principle simply relies on the measured current magnitude.

Overall, aforementioned methods have shown limitations in accurately detecting the loss of synchronism condition in synchronous condensers. These shortcomings highlight the pressing need for the development of an innovative and more effective approach to address these challenges.

2.3.3 Loss of Synchronism Phenomenon in Synchronous Condensers

Synchronous generators have been extensively analyzed for their loss of synchronism behavior, resulting in a well-documented framework for predicting and mitigating such events. However, synchronous condensers, despite their increased usage in modern power systems, have not received the same level of scrutiny. The literature

indicates a considerable gap in understanding the loss of synchronism phenomenon in synchronous condensers, particularly under conditions where IBRs dominate the power grid. The integration of IBRs, characterized by their fast controls and low inertia has introduced new dynamics and complexities. This has led to a recognition of the need for more detailed investigations to accurately predict and manage loss of synchronism events in systems with a high penetration of IBRs.

2.4 Concluding Remarks

Over the years, numerous loss of synchronism protection schemes have been designed to ensure controlled separation and prevent system failures. Some of the widely used schemes for synchronous generators are ranging from traditional impedance-based methods such as Mho circles, blinders, and lens schemes to advanced approaches like rate of change of swing center voltage, resistance, or impedance. While traditional schemes rely on analysing impedance trajectories, modern techniques emphasize dynamic variables to enhance responsiveness and adaptability to the evolving complexities of power systems. Nevertheless, these methods often face challenges related to intricate configuration requirements, computational intensity, and limited flexibility.

Synchronous condensers also employ similar impedance-based techniques, alongside other approaches like notching relays, field AC overcurrent, phase overcurrent, and speed measurement schemes. These methods also encounter challenges and limitations, including delayed responses, difficulty in distinguishing between stable and unstable swings, and dependence on physical sensors.

A notable gap in the literature is identified on the understanding of loss of synchronism conditions in synchronous condensers. While synchronous generators benefit from a well-established framework for managing such conditions, synchronous condensers have not been examined with the same depth, especially in power grids dominated by inverter-based resources (IBRs). The unique dynamics of IBRs, including their fast control actions and low inertia, introduce new challenges, highlighting the necessity for advanced and more precise loss of synchronism protection strategies.

Chapter 3

Generator Loss of Synchronism Protection Using Trajectory of Relative Speed

3.1 Introduction

The rotational speed acts as a direct indicator of loss of synchronism conditions, as disturbances causing energy imbalances within a machine lead to speed variations. In fact, rotor speed variations resulting from power system disturbances trigger the loss of synchronism condition. Therefore, generator speed serves as a valuable metric for detecting loss of synchronism scenarios. Building on this principle, a novel loss of synchronism protection scheme has been developed, utilizing the trajectory of the generator's relative rotational speed.

This chapter is structured as follows: Section 3.2 outlines the development of the

proposed scheme, detailing the estimation of relative speed and the loss of synchronism detection algorithms. Section 3.3 describes the implementation and validation of the proposed scheme in PSCAD/EMTDC. Section 3.4 presents the results of case studies conducted to assess the sensitivity and security of the proposed method under various system conditions, including the validation of omitting stator transients in the speed estimation algorithm. Lastly, Section 3.5 provides the concluding remarks for this chapter.

3.2 Methodology

The proposed method detects the loss of synchronism condition of a generator using its relative speed (difference between its actual speed and the synchronous speed) vs time trajectory ($\Delta\omega$ vs t plot). The relative speed can be calculated using the terminal voltage and current quantities along with generator parameters or can be directly obtained via physical speed sensors. Generally physical speed sensors have high signal to noise ratio (SNR) and not very desirable. The proposed algorithm monitors the relative speed trajectory following a fault and declares the loss of synchronism condition if it follow a certain pattern. This technique is computationally simple, easy to implement and observed to be fast compared to traditional impedance based methods. This method is validated using time-domain simulations performed under different system conditions and various types of disturbances to assess its effectiveness and reliability. A basic connection diagram of the proposed loss of synchronism relay is depicted in Figure 3.1.

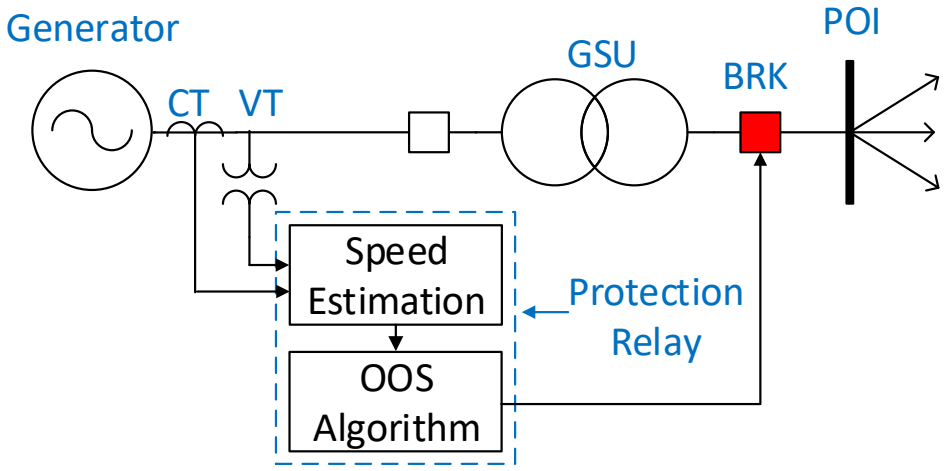

Figure 3.1: Basic connection diagram of the proposed loss of synchronism relay

If the speed of the generator is not readily available, it can be estimated using generator parameters and its terminal quantities (voltage and current measurements). The effect of stator transients on the calculation of relative speed is not essential for the purpose of loss of synchronism detection. Therefore, stator transients can be neglected in the calculation. Further details of stator transients are discussed in Section 3.2.3 and the assumption of neglecting stator transients in the loss of synchronism detection algorithm is validated in Section 3.4.2.

3.2.1 Estimation of Relative Rotational Speed

The estimation of relative speed using its terminal quantities and generator parameters is given below. The per unit value of instantaneous electrical power output from the generator is calculated as;

$$P_t = \frac{v_a \cdot i_a + v_b \cdot i_b + v_c \cdot i_c}{S_{base}} \tag{3.1}$$

where;

v_a, v_b, v_c = instantaneous terminal phase to neutral voltages

i_a, i_b, i_c = instantaneous terminal currents

S_{base} = rated MVA of the generator

Per unit electrical power loss due to stator resistance is calculated as;

$$P_r = \frac{(i_a^2 + i_b^2 + i_c^2) \cdot R_s}{S_{base}} \tag{3.2}$$

Where R_s is the stator resistance and S_{base} is the rated MVA of the generator. Therefore, the converted power in the generator is,

$$P_e = P_t + P_r \tag{3.3}$$

where; P_t = output electrical power and P_r = resistive losses in the stator. From the rule of energy conservation, the pre-fault mechanical power is calculated as, $P_m = P_e$. The calculated pre-fault mechanical power is smoothed by applying digital RMS calculation as in (3.4) or sending through a low pass filter to remove any high frequency content in it. The calculation of digital RMS (X) of an instantaneous signal $x(t)$ is given in (3.4).

$$X = \sqrt{\frac{1}{N} \cdot \sum_{n=1}^{N} [x(t - (N-n)\Delta t)]^2} \tag{3.4}$$

where, N = number of samples per cycle, t = present time and Δt = sample time, which is calculated as;

$$\Delta t = \frac{1}{f \cdot N} \tag{3.5}$$

with f being the base frequency. Therefore, average mechanical power is calculate as;

$$P_m = \sqrt{\frac{1}{N} \cdot \sum_{n=1}^{N} \left[P_e(t - (N-n)\Delta t)\right]^2} \tag{3.6}$$

Assuming the governor's response is comparatively slow, and the mechanical power is constant during the fault and immediate post fault period, the relative speed ($\Delta\omega$) is calculated using (3.3), (3.6) and the swing equation [48] as;

$$\frac{2H}{\omega_s} \cdot \frac{d^2\delta}{dt^2} = P_a = P_m - P_e \tag{3.7}$$

$$\Delta\omega = \frac{d\delta}{dt} = \int_{t_0}^{t} \frac{\omega_s}{2H} \left(P_m - P_e\right) dt \tag{3.8}$$

where;

H = inertia constant of the generator (s)

ω_s = rated speed of the generator (in per unit, $\omega_s = 1$), and

P_a = acceleration power

The use of instantaneous power instead of positive-sequence active power is driven by several considerations. Accurate phasor estimation typically requires windowed data acquisition, filtering, and discrete Fourier transform–based or equivalent algorithms to extract magnitude and phase information. These processes introduce

additional computational complexity, memory requirements, and processing latency, particularly when high sampling rates are used. In contrast, proposed approach that avoid explicit phasor estimation reduce both algorithmic complexity and execution time, making it more suitable for fast-acting protection and control applications.

Phasor extraction typically introduces a one-cycle delay and also eliminates higher order harmonics caused by transients. Therefore, use of positive sequence active power delays the activation of pickup logic resulting in increased error in the estimated relative speed. In addition, power associated with harmonics and distortions are also excluded from the active power calculation, introducing error in the estimation of total air-gap power responsible for rotor acceleration.

Pickup and Reset Logic of Speed Estimation Algorithm

Pickup logic functions by freezing the pre-disturbance electrical power (P_e) at the time of disturbance, allowing it to be designated as the mechanical power input (P_m) to the machine. Essentially, pickup logic serves as a rapid disturbance detector, identifying fluctuations in instantaneous active power to determine whether the relay should activate. It operates by monitoring changes in instantaneous active power, specifically, if $|Pe_n - Pe_{n-1}| > \Delta P_{pickup}$, the relay is triggered, and P_m is held constant.

Reset logic is activated when the pickup signal remains active for a specified duration (T_{reset}) and the estimated relative speed ($\Delta\omega$) falls below a predefined threshold ($\Delta\omega_{reset}$). This ensures that any discrepancies caused by an incorrect P_m alignment do not lead to an unnecessary relay operation during stable power swings.

A block diagram of the proposed speed estimation algorithm is depicted in Figure

3.2. The accuracy and effectiveness of the relative speed estimation algorithm is evaluated by comparing the estimated values against the actual/measured counterparts in Section 3.4.1.

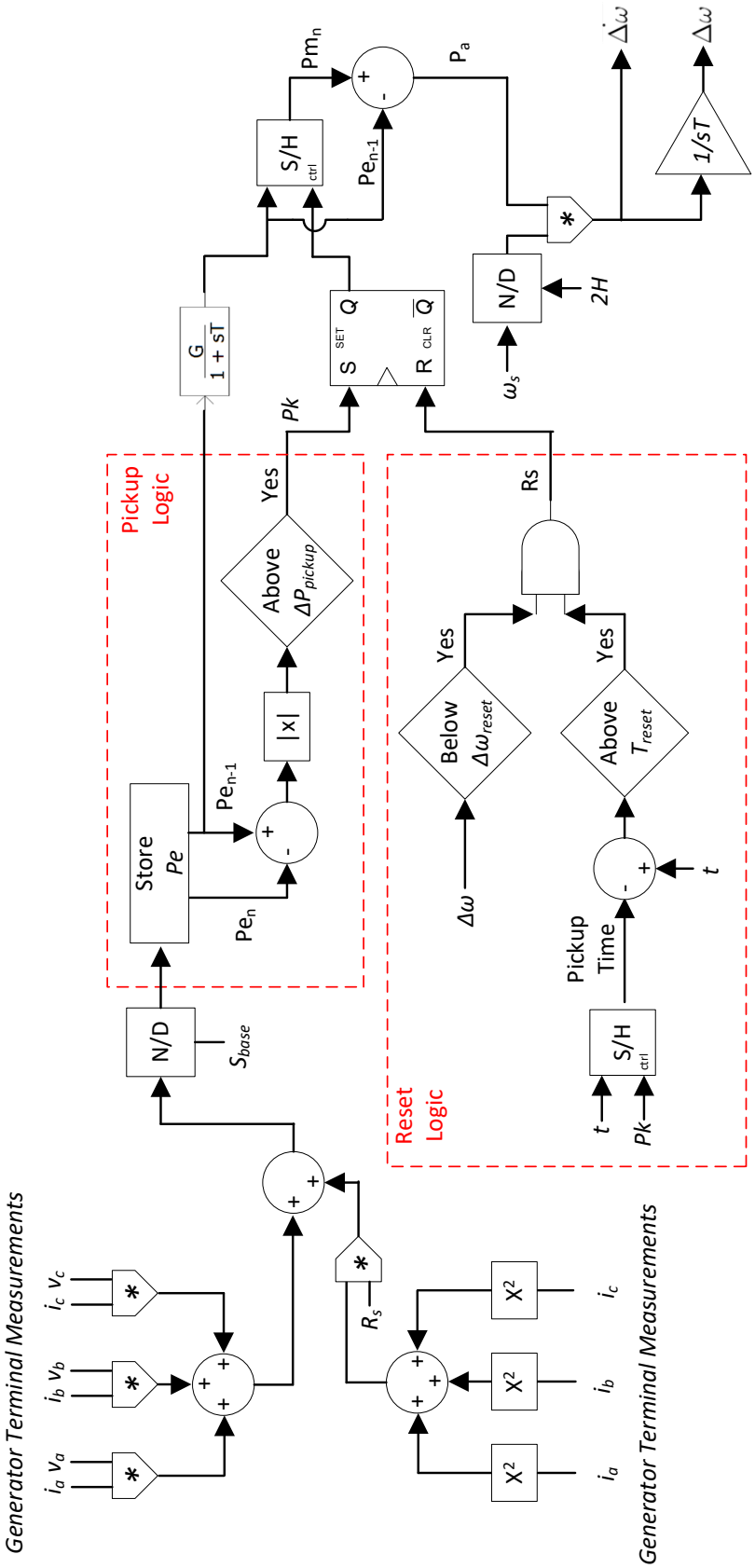

Figure 3.2: Estimation of relative speed using terminal measurements and machine parameters

3.2.2 Loss of Synchronism Detection Algorithm

In the proposed method, the loss of synchronism is detected using post fault relative speed vs time characteristics. Two examples of the relative speed vs. time characteristics, for stable and unstable power swings are shown in Figure 3.3b. These power swings are derived using five bus test system from IEEE PSRC generator protection tutorial [1], wherein a permanent three-phase-to-ground (3LG) fault is applied at location A (see Figure 3.3a), followed by the disconnection of line $L45$ after 100 ms (stable power swing) and 239 ms (unstable power swing), respectively. The test system parameters can be found in Appendix A.1.

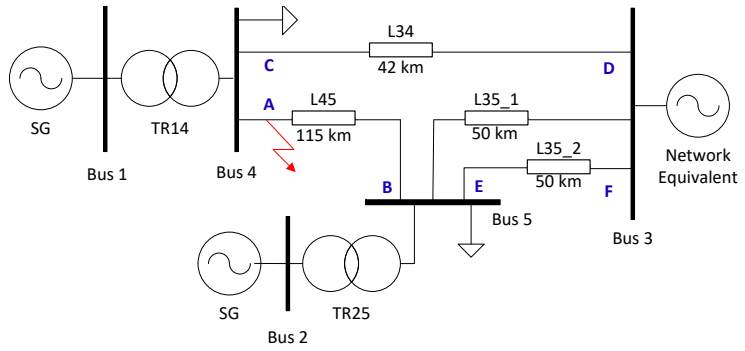

(a)

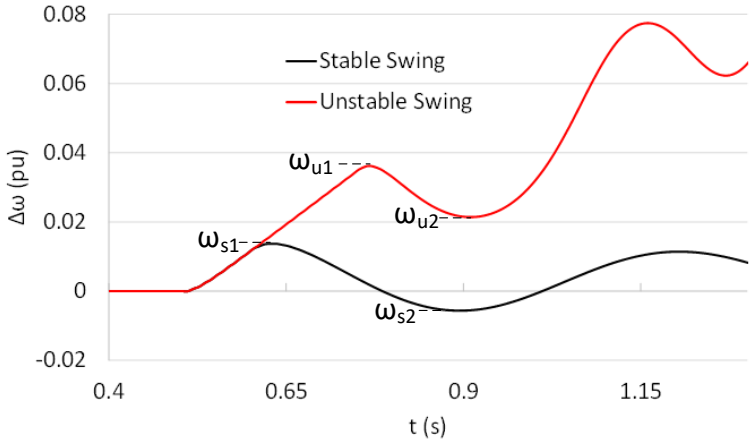

(b)

Figure 3.3: (a) Five bus test system from IEEE PSRC generator protection tutorial [1], (b) Relative speed ($\Delta\omega$) trajectories for stable and unstable power swings

At steady state, the generator speed is 1 pu - i.e. relative speed is zero. During the fault, relative speed increases until the fault is cleared. In the example shown in Figure 3.3b, both faults are applied at 0.5s and cleared at 0.6s (6 cycles) and 0.75s (15 cycles) creating stable and unstable power swings, respectively. Once the fault is cleared, the relative speed changes based on the stability of the power swing. For a stable power swing, relative speed oscillates around time axis and eventually settles at zero. For an unstable power swing, the relative speed keeps increasing and poles keep slipping until the generator trips.

The above-described nature of a generator's relative speed after fault clearance is used in the proposed algorithm to detect a loss of synchronism condition. The proposed algorithm declares a power swing as an unstable swing if the relative speed measured at the fault clearance ($\Delta\omega_{u1}$) and at the first minimum (or maximum) ($\Delta\omega_{u2}$) have the same polarity. Similarly, a stable condition is declared if the relative speed measured at the fault clearance ($\Delta\omega_{s1}$) and at the first minimum (or maximum) ($\Delta\omega_{s2}$) have opposite polarities. The algorithm can be set to check the polarity of second and two consecutive minimums and maximums instead of the first two if the generator allows one or more pole slips. Minimums and maximums of the relative speed trajectory are identified by the zero crossings of the derivative of relative speed.

Pickup and Reset Logic of Loss of Synchronism Detection Algorithm

The relay pickup and reset functions are based on the comparison of estimated relative speed against a user defined threshold settings. These threshold settings are not active protection settings where the timing of the trip signal is affected. They are

rather a set of settings where the activation and deactivation of the relay is based on. These threshold settings ensure security against unintended relay activation caused by minor speed variations observed during normal operation. If the estimated speed exceeds the pick up threshold value, the loss of synchronism relay picks up and starts storing the relative speeds at maximums (or minimums) in an array of memory to be used by the loss of synchronism detection function.

The reset function operates when the relative speed at a minimum (or a maximum) is lower than the reset threshold value for a period longer than two cycles of the electromechanical oscillation. It is highly unlikely that the power swing will be unstable once the relative speed reduced beyond the reset threshold for a period of two cycles (unless a secondary power swing occurs before the first swing is fully settled). In other words, the two-cycle setting ensures that the oscillation is well damped. The calculation of two-cycle period is based on the slip frequency which is dynamically calculated using the zero crossings of the relative speed.

A block diagram of the proposed loss of synchronism detection algorithm is depicted in Figure 3.4. This approach is easy to implement and effectively identifies both first-swing and multi-swing transient instabilities in a system after a major disturbance. Additionally, setting up the relay configurations for this method is simple, reducing the time and effort required by utility engineers.

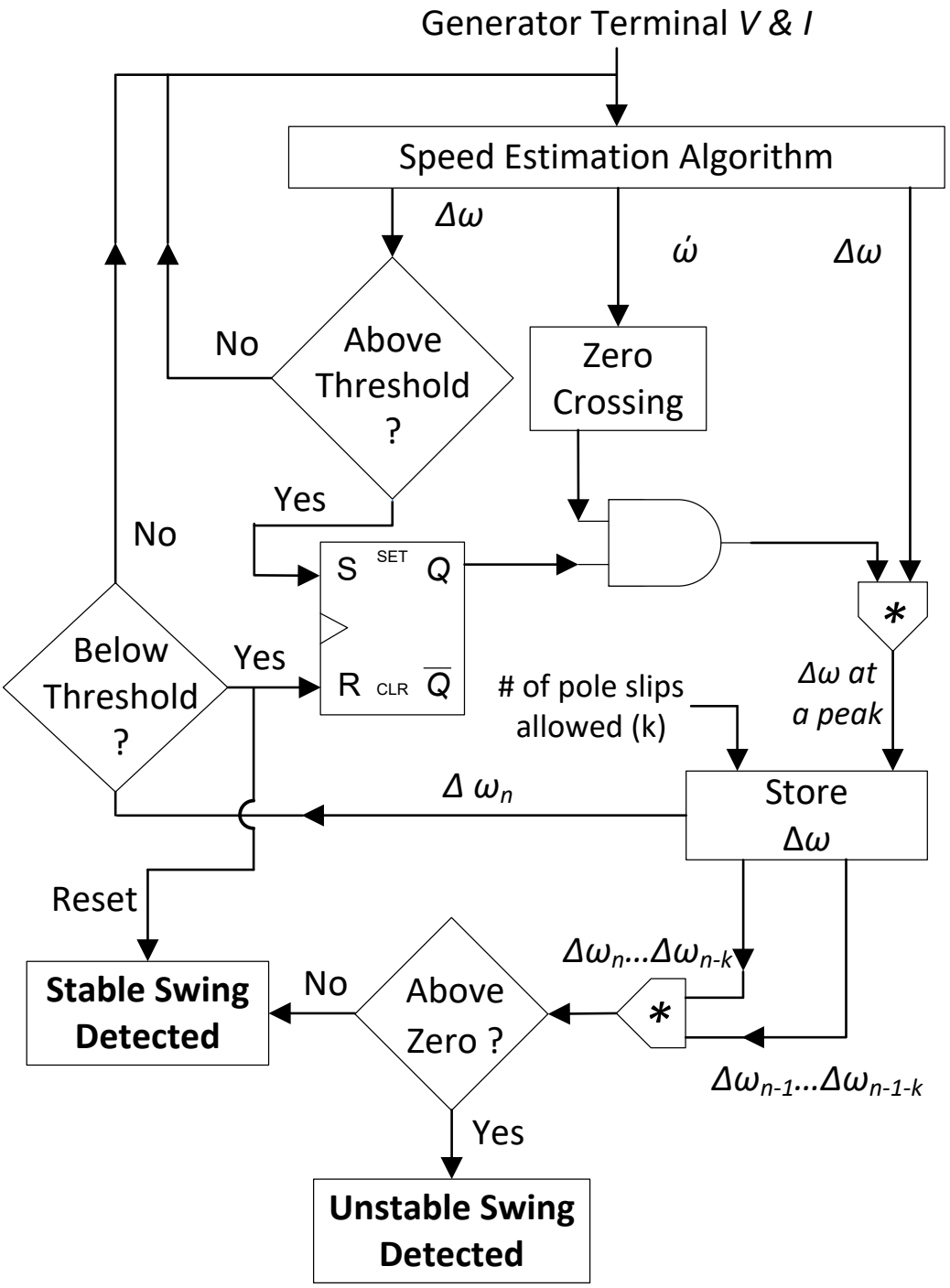

Figure 3.4: schematic of proposed loss of synchronism detection method

3.2.3 Effect of Stator Transients on Relative Speed

The effect of stator transients on the calculation of generator's relative speed is analyzed in this section. Equations for the synchronous generator stator circuit voltage can be written as [48, 49];

$$v_a = \frac{\mathrm{d}\psi_a}{\mathrm{d}t} - Ri_a = p\psi_a - Ri_a \tag{3.9a}$$

$$v_b = p\psi_b - Ri_b \tag{3.9b}$$

$$v_c = p\psi_c - Ri_c \tag{3.9c}$$

where;

v_a, v_b, v_c = instantaneous stator induced EMF (L-G)

i_a, i_b, i_c = instantaneous stator currents in phases a, b, c

R = armature resistance per phase

p = differential operator d/dt

The flux linkage in the phase a at any instant is given by

$$\psi_a = -l_{aa}i_a - l_{ab}i_b - l_{ac}i_c + l_{afd}i_{fd} + l_{akd}i_{kd} + l_{akq}i_{kq} \tag{3.10}$$

where;

l_{aa}, l_{bb}, l_{cc} = self inductance of stator windings

l_{ab}, l_{bc}, l_{ca} = mutual inductance between stator windings

l_{afd}, l_{akd}, l_{akq} = mutual inductance between stator and rotor windings

i_{fd}, i_{kd}, i_{kq} = field and amortisseur circuit currents

Similar expressions apply to flux linkages of windings b and c. The negative sign associated with the stator winding currents is due to their assumed direction. All the inductances in (3.10) are functions of the rotor position and are thus time-varying.

As explained in Section 3.2.1, the instantaneous electrical power output from the generator is calculated as;

$$P_t = v_a \cdot i_a + v_b \cdot i_b + v_c \cdot i_c \tag{3.11}$$

Phase voltages and currents can be converted into corresponding $dq0$ components using Park's transformation [50] shown in (3.12).

$$\begin{bmatrix} x_d \\ x_q \\ x_0 \end{bmatrix} = \frac{2}{3} \begin{bmatrix} cos(\theta) & cos(\theta - \frac{2\pi}{3}) & cos(\theta + \frac{2\pi}{3}) \\ -sin(\theta) & -sin(\theta - \frac{2\pi}{3}) & -sin(\theta + \frac{2\pi}{3}) \\ \frac{1}{2} & \frac{1}{2} & \frac{1}{2} \end{bmatrix} \begin{bmatrix} x_a \\ x_b \\ x_c \end{bmatrix} \tag{3.12}$$

Applying Park's transformation on (3.11) gives;

$$P_t = \frac{3}{2}(v_d \cdot i_d + v_q \cdot i_q + 2 \cdot v_0 \cdot i_0) \tag{3.13}$$

(3.9a) to (3.9c) are basic equations for phase voltages in terms of phase flux

linkages and currents. Application of the $dq0$ transformation on (3.9a) to (3.9c) gives [48];

$$v_d = p\psi_d - \psi_q p\theta - Ri_d \tag{3.14a}$$

$$v_q = p\psi_q + \psi_d p\theta - Ri_q \tag{3.14b}$$

$$v_0 = p\psi_0 - Ri_0 \tag{3.14c}$$

The angle θ is the angle between the axis of phase a and the d-axis. The term $p\theta$ represents the angular velocity (ω_r) of the rotor. Substituting v_d, v_q and v_0 in (3.13) with (3.14a) to (3.14c) and rearranging, an expression for P_t can be obtained as;

$$\begin{aligned} P_t = \frac{3}{2}[&(i_d p\psi_d + i_q p\psi_q + 2i_0 p\psi_0) \\ &+ (\psi_d i_q - \psi_q i_d)\,\omega_r \\ &- \left(i_d^2 + i_q^2 + 2i_0^2\right) R] \end{aligned} \tag{3.15}$$

$$P_t = P_{st} + P_e - P_r \tag{3.16}$$

where;

P_{st} = Rate of change of armature magnetic energy

P_e = Power transferred across the air gap

P_r = Armature resistance loss

Ideally, the electrical power responsible for the acceleration or deceleration of the rotor is the power transferred across the air-gap. Therefore, in the exact calculation of relative speed in (3.8), the term P_e should be calculated using both "armature resistance loss" and "rate of change of armature magnetic energy".

The term "rate of change of armature magnetic energy" or in other words the transformer voltage term ($p\psi_d$, $p\psi_q$) represents the stator transients, which prevent ψ_d and ψ_q from changing instantaneously. It is the phenomenon that produces the dc offset in the fault currents. The omission of $p\psi_d$, $p\psi_q$ terms would therefore, eliminate the dc offset and its related effects on the dynamic performance of the generator.

The stator transients usually exist during a fault or disturbance and decay within a much shorter time compared to the time scale of rotor speed variations.Therefore, the effect of transient currents can be ignored without much error. Further, the proposed loss of synchronism detection method is not affected by neglecting stator transients because the loss of synchronism condition usually occurs when the disturbance is cleared where the stator transients are minimal.

3.3 EMT Simulation Model

EMT simulations are essential for loss of synchronism protection studies, primarily because they capture protection relay behavior that depends on instantaneous voltage and current waveforms, as well as fast system dynamics including those introduced by IBRs and non-linear effects such as control limiters and commutation phenomena, all of which can significantly affect stability margins and relay performance during

loss of synchronism events.

Implementation of the proposed scheme and other well established methods in an EMT program is discussed in following sections.

3.3.1 Implementation of Proposed Loss of Synchronism Protection Scheme

The proposed loss of synchronism protection method is implemented as a custom component in PSCAD/EMTDC Version 4.6.3. The model is built using control blocks and custom components that were written using Fortran 95 programming language and compatible for Intel Fortran compiler version 9.0 or higher. The relay calculations are performed at 32 samples per cycle (time step of 520.833μs). The rate of 32 samples per cycle is selected to ensure accurate calculation of pre-disturbance active power, which is essential for reliable rotor speed estimation. Since the relay calculation time step is not an integer multiple of the PSCAD simulation time step, which is 10 μs, the voltage and current measurement samples are obtained by interpolating relevant values of each calculation time stamp (e.g. measurements at 520μs and 530μs are interpolated to obtain the values at 520.833μs). The implementation of two algorithms are discussed below.

Relative Speed Estimation Algorithm

At each relay calculation step, the instantaneous active power is determined (as shown in (3.11)) and compared with its previous time step value to compute the active power difference (ΔP). If ΔP exceeds the pickup threshold (ΔP_{pickup}), the

relative speed estimation algorithm is activated, freezing the mechanical power at that moment as the power transferred across the air-gap. This corresponds to the sum of instantaneous electrical power and resistive losses, assuming stator transients are negligible (see (3.16)). From that point onward, the algorithm begins calculating ($\Delta\omega$) until the reset logic is triggered. If the algorithm is not activated (i.e.ΔP remains below the threshold), the generator's mechanical power input is assumed to be equal to the power transferred across the air-gap.

When expressed in p.u., acceleration torque is equal to acceleration power (assuming the machine rotates at synchronous speed). Therefore, all power values are converted into per unit values on the machine base. Then the relative speed is calculated by integrating the swing equation of the machine (3.8) by applying trapezoidal integration. This gives,

$$\Delta\omega = \frac{\omega_s}{2H} P_m - \frac{\omega_s}{2H} \left[\left(\frac{P_e(t_1) + P_e(t_2)}{2} (t_2 - t_1) \right) \right] \tag{3.17}$$

where; t_2 and t_1 are time stamps of present and previous time steps, respectively.

The machine inertia constant and the stator resistance are the only input data used other than the measured voltages and currents. The rated speed is added to the output of integrator ($\Delta\omega$) to obtain the machine speed (ω) for comparison purposes.

Loss of Synchronism Detection Algorithm

The two main outputs of the speed estimation algorithm, namely, relative speed ($\Delta\omega$) and the rate of change of speed ($\Delta\dot{\omega}$ - which is linearly proportional to accel-

eration power) are used as inputs for the loss of synchronism detection algorithm. The relay pickup and reset functions are implemented using level comparators and a Set/Reset latch model. If relative speed is greater than the pickup threshold, then the relay picks up and latches until the reset function activates.

The pickup and reset thresholds of relative speed are set to 0.01 pu and 0.005 pu. These thresholds are chosen such a way that the relay will not pick up for minor system oscillations and also pick up fast enough during power swings to detect the first pole slip. In other words, the final decision of the relay or the timing of the trip signal is not affected by this threshold setting (unless the threshold setting is too large and misses the first pole slip).

Once the relay is picked up, the relative speed at every positive and negative maximum is stored in an array of memory until a trip or reset signal is issued. The maximum/minimum point of relative speed is detected by observing the zero crossing of rate of change of speed ($\dot{\omega}$) trajectory. Adjacently stored relative speeds are multiplied with each other and compared against zero using a level comparator to detect whether the speed oscillation is stable or unstable. If the adjacent speeds have the same sign, the speed is either continuously increasing or decreasing. Hence the algorithm declares an unstable power swing and issues a trip signal. The number of relative speed pairs to check can be adjusted based on number of pole slips allowed before tripping. Similarly, if the adjacent relative speeds have different signs, indicating that the speed oscillation is damping, the algorithm declares that the oscillation is stable and a trip signal will not be issued. Ultimately, when the stored relative speed is less than the reset threshold, relay rest signal is issued.

3.3.2 Implementation of Other Loss of Synchronism Algorithms

To compare the performance of the proposed method against existing generator loss of synchronism methods, a well established traditional method and a relatively novel terminal voltage based method from literature were implemented in PSCAD/EMTDC. Double blinder method [1, 8, 11, 25] and the rate of change of voltage (ROCOV) method [3] were selected as the candidates for comparison purposes. The ROCOV method is originally developed for transmission line out-of-step protection in reference [3] and the same concept is applied for generator loss of synchronism protection in this thesis.

Double Blinder Schemes

The double blinder scheme was implemented as a custom component, following the operational principles described in Schweitzer generator relay instruction manual [51]. This implementation utilizes a Direct Fourier Transformation (DFT) algorithm paired with an anti-aliasing filter to compute positive sequence phasors, with a sampling rate of 32 samples per cycle. At each processing time step, impedance is calculated and evaluated based on the principles of the double blinder scheme outlined in Schweitzer instruction manual. A general explanation of these operational principles is provided in Section 2.2.1 of Chapter 2.

The settings for the double blinder scheme depend on the maximum slip frequency observed during loss of synchronism conditions, making the settings highly

system-specific rather than solely dependent on machine parameters. Consequently, a detailed stability study is required to determine accurate settings. To achieve this, an EMT stability study was conducted using the test system described in Section 3.4, and the settings were calculated based on the results of this study in conjunction with guidance from the SEL-700G manual. Additional details on the setting calculations are provided in Appendix B.2.

ROCOV Schemes

This scheme uses the generator terminal voltage magnitude as a key indicator of post-disturbance transient instability in the power system. The two primary transient stability indicators employed are the generator terminal voltage deviation ΔV and the rate of change of ΔV ($ROCOV$). These indicators are computed as follows:

$$\Delta V = Vmag - 1 \tag{3.18}$$

$$\frac{\mathrm{d}}{\mathrm{d}t}\Delta V = \frac{\mathrm{d}}{\mathrm{d}t}Vmag = ROCOV \tag{3.19}$$

where, $Vmag$ is the measured voltage magnitude in pu, and $ROCOV$ is rate of change of voltage (pu/s).

An example post-disturbance trajectories of the generator power angle, terminal voltage and corresponding $ROCOV - \Delta V$ are shown in Figures 3.5, 3.6, and 3.7, respectively. These examples are derived using five bus test system from IEEE PSRC generator protection tutorial [1], wherein a permanent three-phase-to-ground (3LG) fault is applied at location A (see Figure 3.3a), followed by the disconnection of line

$L45$ after 100 ms (stable power swing), 238 ms(marginally stable power swing) and 239 ms (unstable power swing), respectively. Trajectories in the $ROCOV - \Delta V$ plane are shown starting one 60 Hz cycle after fault clearance for better clarity. When the system is stable, the operating point takes a spiral trajectory and converges to a point on the ΔV axis. When the power system is unstable, the trajectory diverges - i.e. the operating point moves away from the origin farther into the 2nd, 3rd or 4th quadrant of the $ROCOV - \Delta V$ plane.

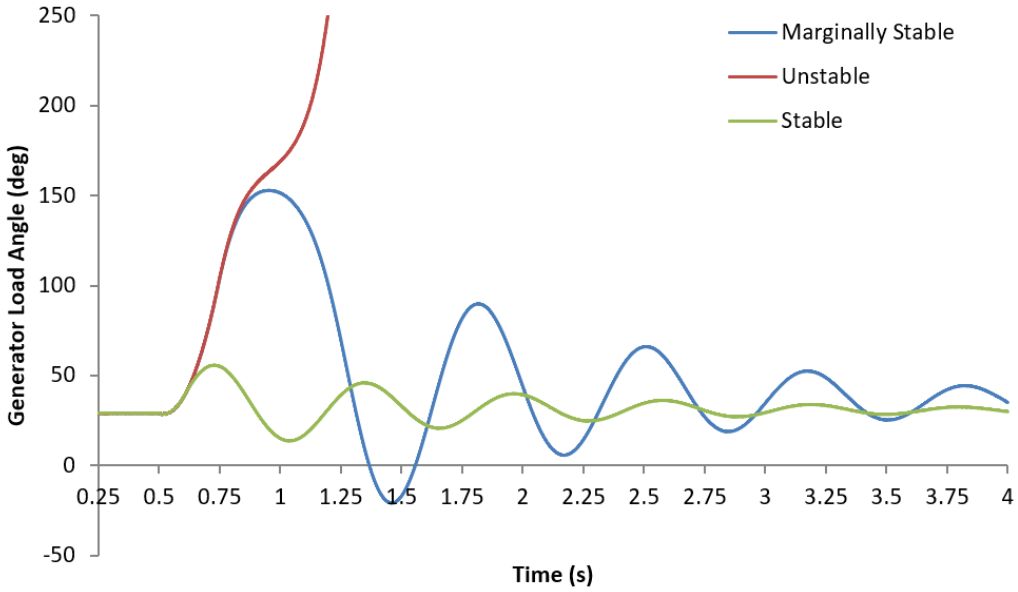

Figure 3.5: Generator power angle during stable, marginally stable, and unstable power swings

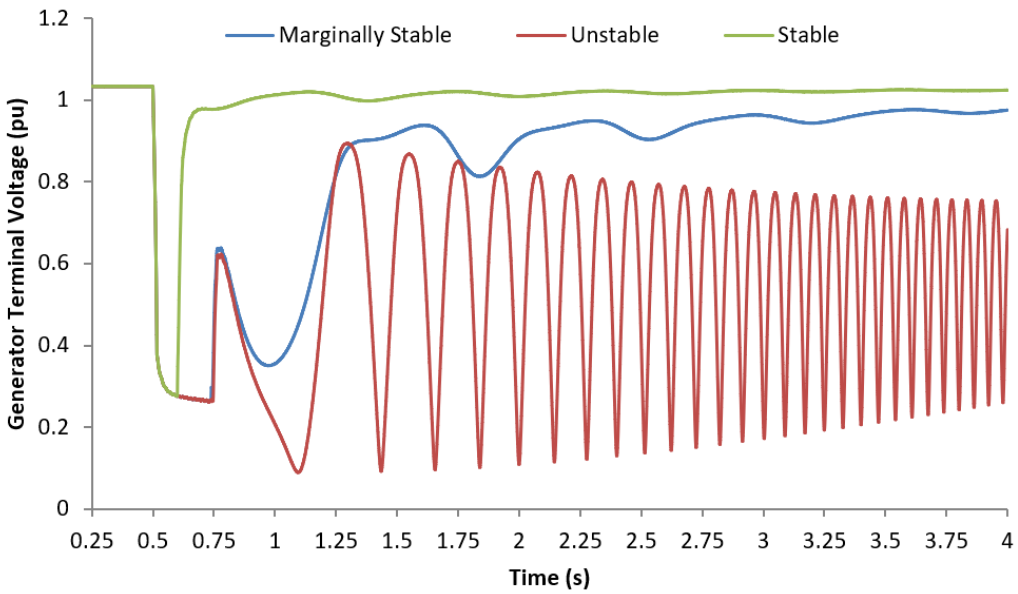

Figure 3.6: Generator terminal voltage during stable, marginally stable, and unstable power swings

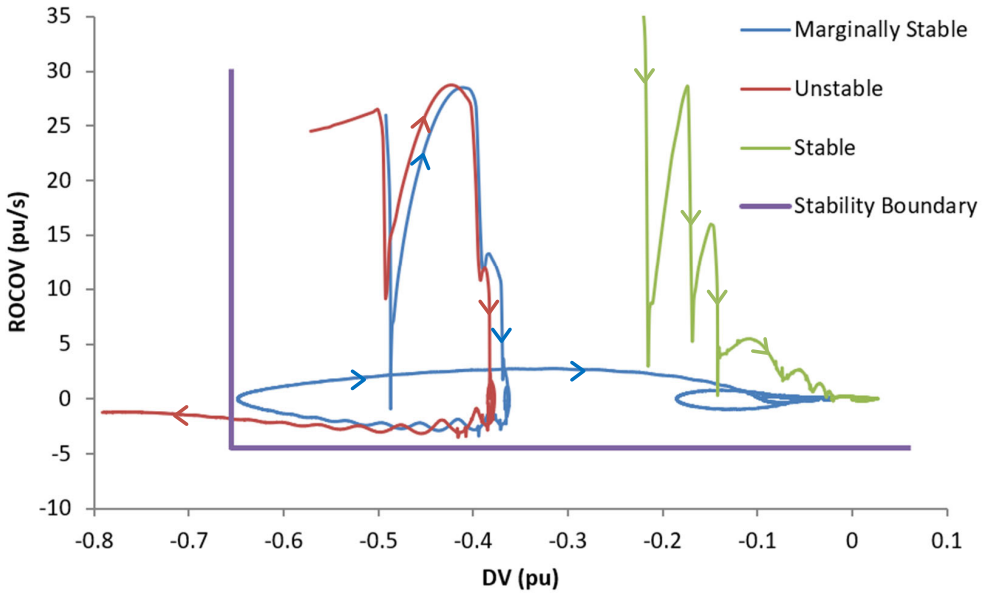

Figure 3.7: Plot of $ROCOV$ vs. ΔV during stable, marginally stable, and unstable power swings

If the post-disturbance operating point (i.e., the trajectory following fault clear-

ance) crosses the stability boundary from the stable region into the unstable region, the generator is identified as unstable. This scheme also implemented as a custom component in PSCAD/EMTDC. Additional details on the setting calculations (i.e. stability boundary) are provided in Appendix B.4.

3.4 Case Study: Performance Validation

To evaluate the performance of the proposed method, several validation and sensitivity studies were conducted. This includes;

- Validation of estimated relative speed
- Sensitivity for,
  - stator transients
  - generator configuration
  - measurement errors
  - system faults
  - small disturbances

All these tests were conducted using the five bus test system referred in the "IEEE tutorial on the protection of synchronous generators" by Power System Relaying Committee (PSRC) [1]. This test system was chosen because its ring topology makes it well-suited for studying loss of synchronism conditions. Disconnecting a transmission line to open the ring network creates a weaker connection to the far-end generator, providing a realistic scenario for loss of synchronism analysis. Additionally, its sim-

plicity reduces the number of variables in the system, making result analysis more straightforward.

A single line diagram of the test network is depicted in Figure 3.8. The network and generator parameters can be found in Appendix A.1.

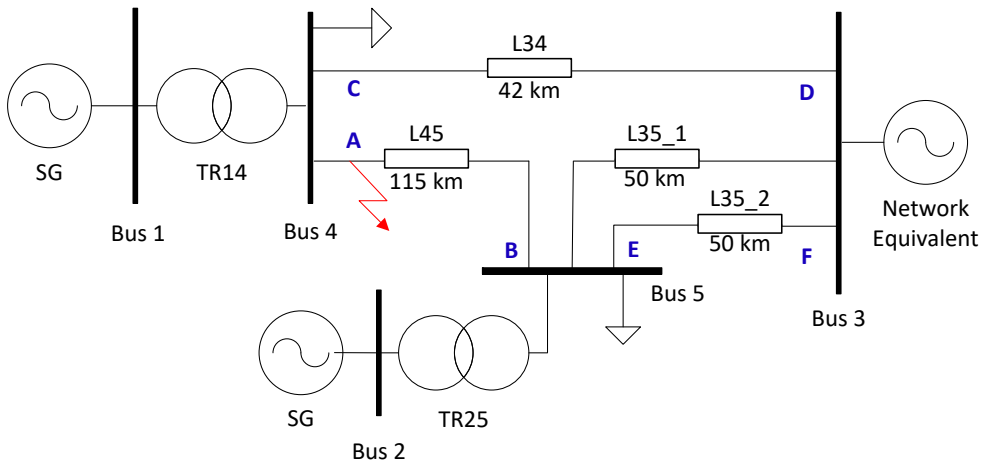

Figure 3.8: Five bus test system from IEEE PSRC generator protection tutorial [1]

All the transmission lines in the test network were implemented in PSCAD/EMTDC using travelling wave based Bergeron models. Active and reactive power loads were represented with constant impedance models. The network equivalent representation was evaluated using both a voltage source behind an impedance and a synchronous machine model to assess the influence of grid-side dynamics. The results indicated that the grid-side dynamic effects were negligible; therefore, the voltage source behind an impedance (E behind Z) representation was adopted for the case studies. The test network was first modelled in PSS/E [52] software platform and then converted into PSCAD/EMTDC using E-TRAN conversion tool [53] to achieve correct initial

conditions (i.e. voltage magnitudes and angles of generator buses and transformer tap settings).

The study details, results, and analysis for each case are provided in Sections 3.4.1 and 3.4.2.

3.4.1 Validation of Estimated Relative Speed

The accuracy and performance of the relative speed estimation algorithm are assessed by comparing the estimated values with the machine model counterparts. Various disturbances were introduced to the test system and the resulted relative speeds were recorded. The estimated relative speed obtained through the proposed algorithm is then compared with the actual relative speed (derived from the internal ω output obtained from the solution of machine differential equations in the PSCAD machine model).

Below are two example plots illustrating the estimated speed under stable and unstable scenarios. These scenarios correspond to the following disturbances:

1. Stable Scenario: a bolted LG fault at location A (in Figure 3.8) and clear it by tripping the line $L45$ after 200 ms

2. Unstable Scenario: a bolted 3LG fault at location A (in Figure 3.8) and clear it by tripping the line $L45$ after 600 ms

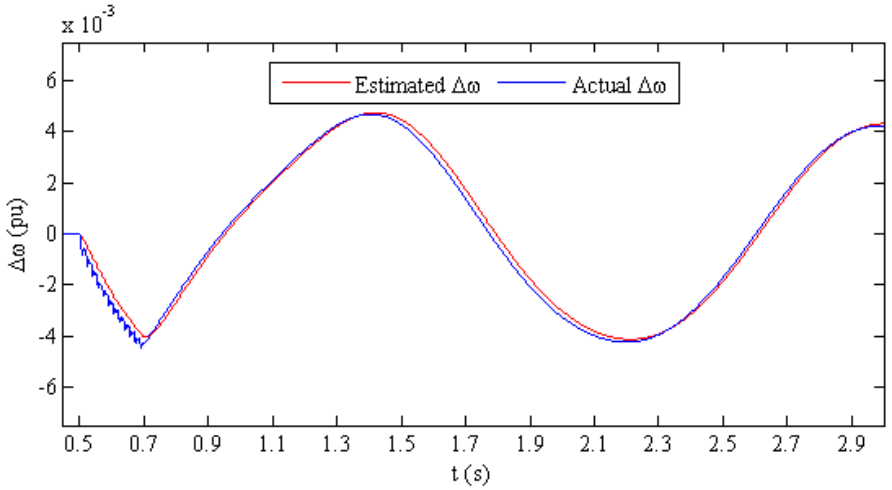

Figure 3.9: Comparison of estimated relative speed against actual: stable scenario

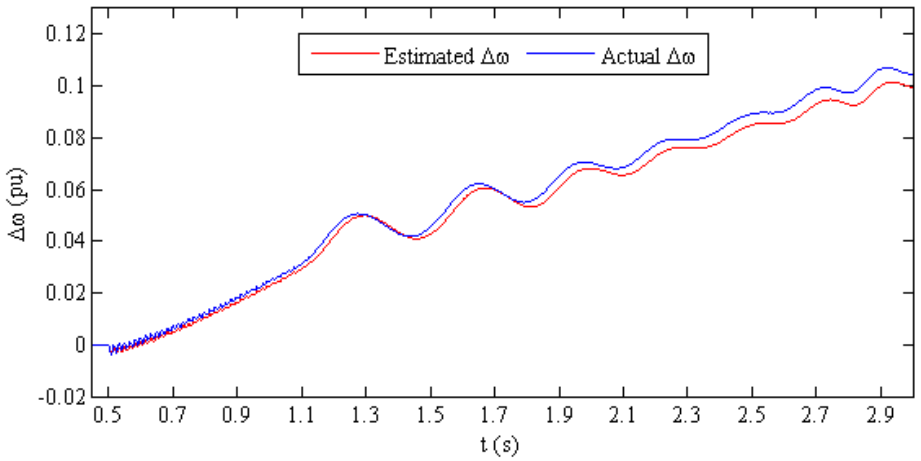

Figure 3.10: Comparison of estimated relative speed against actual: unstable scenario

As demonstrated above, the estimated relative speed closely aligns with the actual speed within the time window of interest. The amplitude discrepancy observed between the estimated and actual relative speeds at later points in time is attributed to integration errors caused by neglecting stator transients. However, these differences are negligible during the initial swings, which are the critical factor for loss of synchronism detection algorithm.

3.4.2 Sensitivity Analysis

Sensitivity of the proposed method to , stator transients, different types of exciters, governors, power system stabilizers (PSS), inertia constants (H), CT and VT errors, system faults, line opening, load and generator tripping were investigated. These sensitivities are categorized under five sections as below.

- Stator Transients - 2 scenarios
- Generator configuration - 5 scenarios
- Measurement errors - 5 scenarios
- System Faults (large disturbances) - 96 scenarios
- Tripping without faults (small disturbances)- 7 scenarios

All the sensitivity tests were performed on the same five bus example network described in section 3.4. All together, hundred and fifteen (115) different scenarios were analysed. Details of each category above are explained below.

Sensitivity For Stator Transients

Two tests were performed to validate the assumption of neglecting the effect of stator transients on the calculation of relative speed. A fault is applied on the bus 4 end of the transmission line between bus 4 and bus 5 ($L45$) and the line was tripped to clear the fault. The duration of the fault was adjusted to 6 cycles and 15 cycles to create stable and unstable power swings. The calculation of stator transients was done by using (3.14) and (3.15) with inputs comprising the generator rotor speed

and $dq0$ components of the stator fluxes, voltages and currents available via internal monitoring signals of PSCAD synchronous machine model [54].

Figure 3.11 shows the calculated rotor speed by neglecting and including the stator transients for the stable and unstable power swings, respectively. The traces where the relative speed is calculated by including stator transients show a slight oscillation during fault, which decays after the fault is cleared. In fact the oscillation amplitude decayed during the fault itself. Since loss of synchronism condition generally occurs after the fault clearance, the effect of stator transients for the proposed technique is negligible. Furthermore, as illustrated in Figure 3.11, the timing of the maximum and minimums in the relative speed trajectory remains unchanged regardless of whether stator transients are considered. Consequently, the inclusion or omission of stator transients does not influence the loss of synchronism trip decision or speed of operation. The amplitude difference between the relative speeds in Figure 3.11 is due to the error accumulated from the integration due to omission of stator transients.

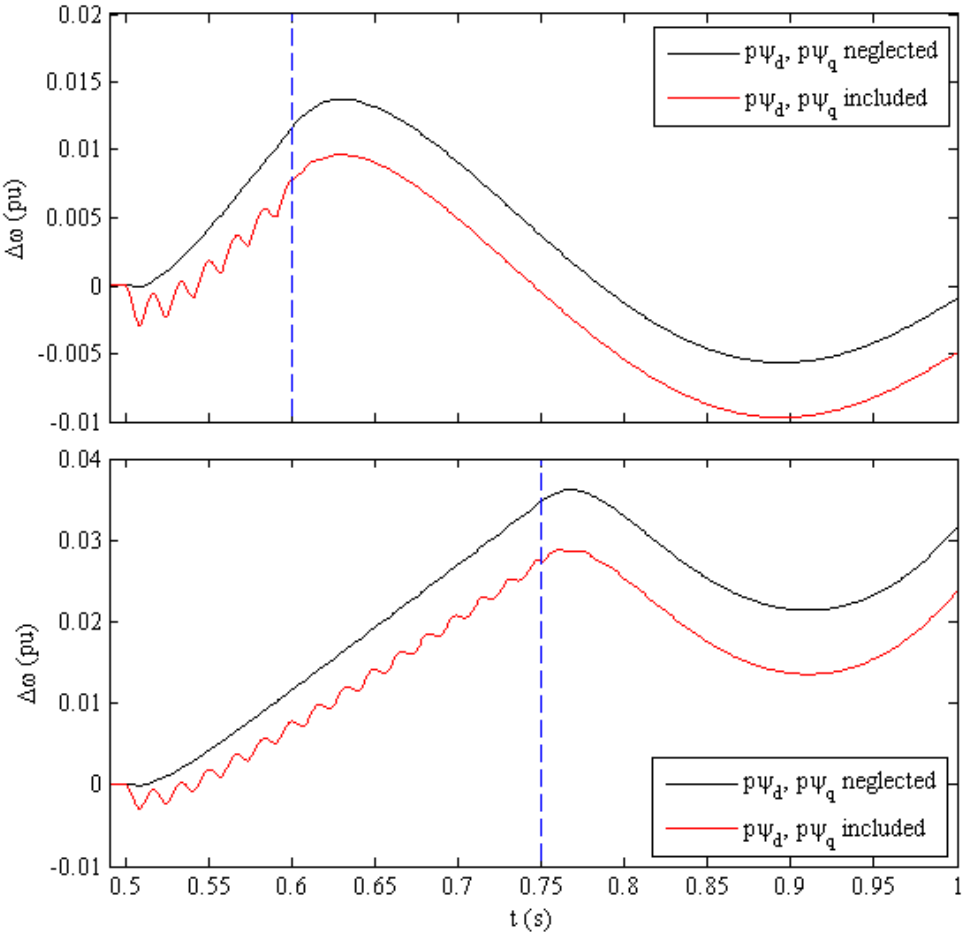

Figure 3.11: Effect of neglecting stator transients on estimated relative speed (fault clearance is shown in blue dotted line)

Sensitivity for Generator Configuration

To analyse the sensitivity of the proposed method on the generator configuration, a number of standard exciters, governors and PSSs were used with the proposed relay model in EMT simulations. For the sensitivity tests of inertia constant a ±10% and ±20% errors were introduced to the generator's inertia.

Results showed that the effect from exciter, governor and PSSs was minimal during

the focused period due to large mechanical and electrical time constants involved. Therefore, significant differences were not observed in the calculated speed and the comparison plots were omitted. The results of inertia constant tests are depicted in Figure 3.12. Under different inertia constants, the estimated speed is deviating from its actual value. However the timestamps of the maximums and minimums are more or less aligned with each other. Therefore, the trip decisions are made at around the same time in all cases regardless of the magnitude of the error introduced if the decision is made after the first or second pole slip. It is possible that the relay can mis-operate if the magnitude of error makes the calculated relative speed stop crossing the x-axis during the first minimum. The magnitude of error required for a mis-operation is based on how stable the power swing is and whether the relay allowed a single pole slip.

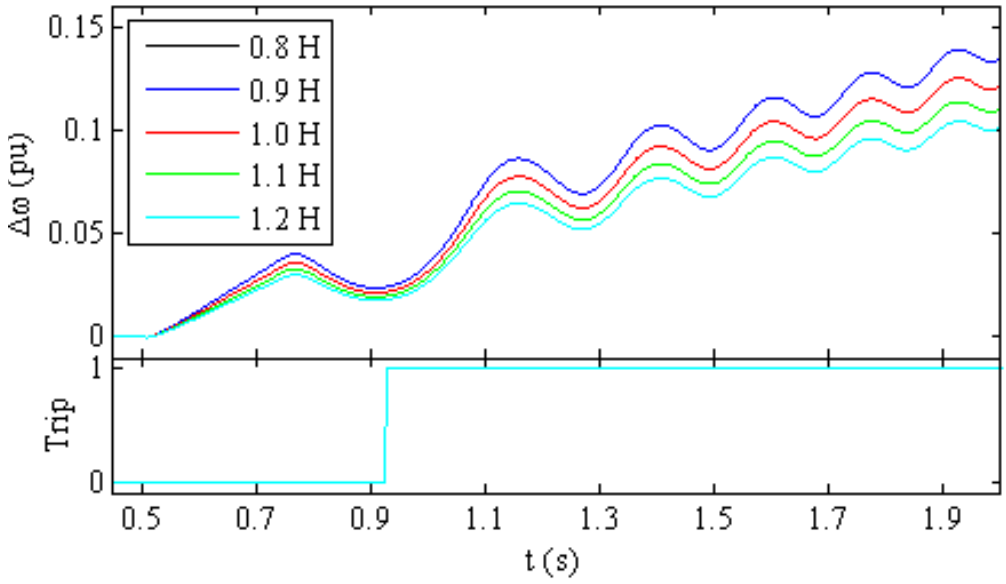

Figure 3.12: Sensitivity of the relative speed to inertia constant

Sensitivity for Measurement Errors

To mimic the errors of measurement devices, a ±10% and ±20% errors were introduced to measured terminal voltages and currents.

The results are depicted in Figure 3.13. Similar to inertia constant tests results, the estimated speed is deviating from its actual and the timestamps of the maximums and minimums are more or less aligned with each other. Therefore, the trip decisions are made at around the same time in all cases regardless of the magnitude of the error introduced.

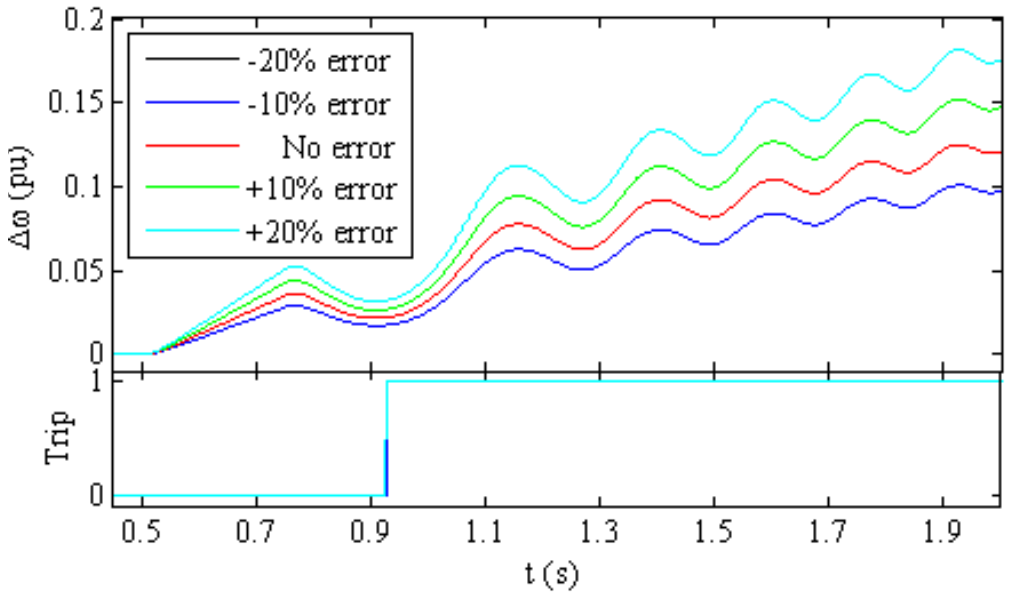

Figure 3.13: Sensitivity of the relative speed to measurement errors

Sensitivity for System Faults

Unique fault scenarios were simulated to test the sensitivity and security of the proposed method. This includes;

- Four fault types - LG, LLG, LLLG and LL
- Six fault locations - Location A-F in Figure 3.8
- Two fault durations - 200 ms and 600 ms
- Two fault impedances - 0.001 and 5 ohms

Therefore, in total Ninety six (96 = 4 x 6 x 2 x 2) scenarios were simulated.

Long-duration faults, such as those persisting beyond 100 ms, typically represent breaker failure scenarios or the operation of backup protection following the failure of the primary protection scheme. Power systems are generally designed such that, under correct operation of primary protection, loss-of-synchronism conditions are unlikely to occur. However, failures of primary protection or circuit breakers can lead to prolonged fault durations, thereby increasing the likelihood of loss-of-synchronism events. Accordingly, extended fault durations are applied in the studies to realistically emulate loss-of-synchronism conditions.

Summary of the test results is tabulated in Table 3.1. As shown below, the majority of simulated scenarios created stable power swings (81 out of 96) and as expected, relay did not pick up for any of those stable swings. Fifteen (15) scenarios out of ninety six (96) observed to have unstable power swings. The proposed algorithm issued the trip signal at the first pole slip in all unstable scenarios except for one. It missed the first pole slip in one scenario due to not normal post fault behaviour of relative speed. However, loss of synchronism detection algorithm issued the trip signal at the second pole slip (see Figure 3.17). Overall, the proposed algorithm has shown success rate of 98.96% for system faults. Plots of a selected stable and an unstable scenario are depicted in Figures 3.14 and 3.15, respectively. Those are related

to bolted LG and 3LG faults at location A (in Figure 3.8) with 200ms and 600ms clearing times.

Table 3.1: Statistical results summary of system fault events

Description	**Number of Scenarios**		
	Simulated	**Detected Correctly**	**Mis/Delayed Operation**
Unstable Power Swings	15	14	1
Stable Power Swings	81	81	0
Total	96	95	1
Total as %	100 %	98.96 %	1.04 %

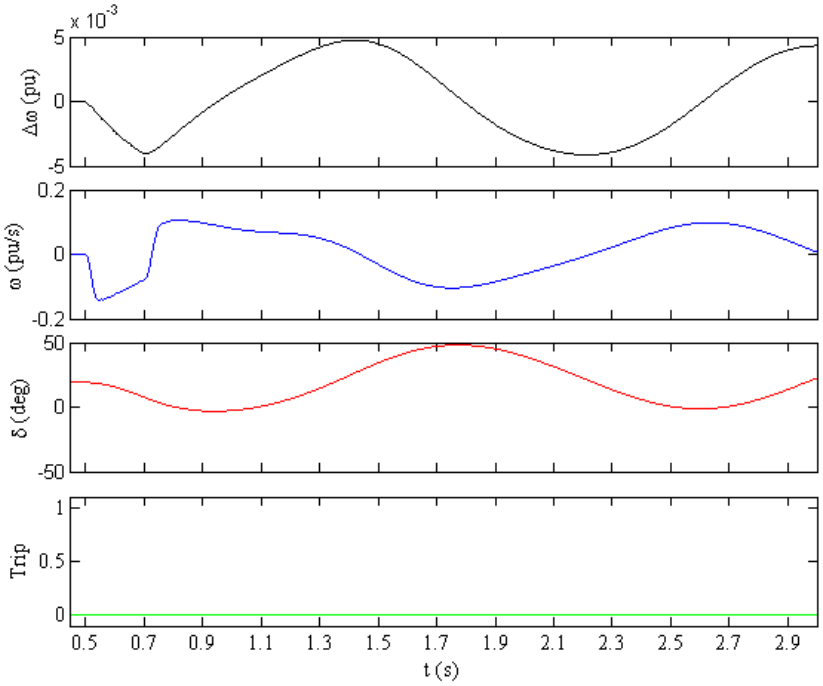

Figure 3.14: Relative speed ($\Delta\omega$), rate of change of relative speed ($\dot{\Delta\omega}$), power angle (δ) and loss of synchronism detection signals during a stable scenario

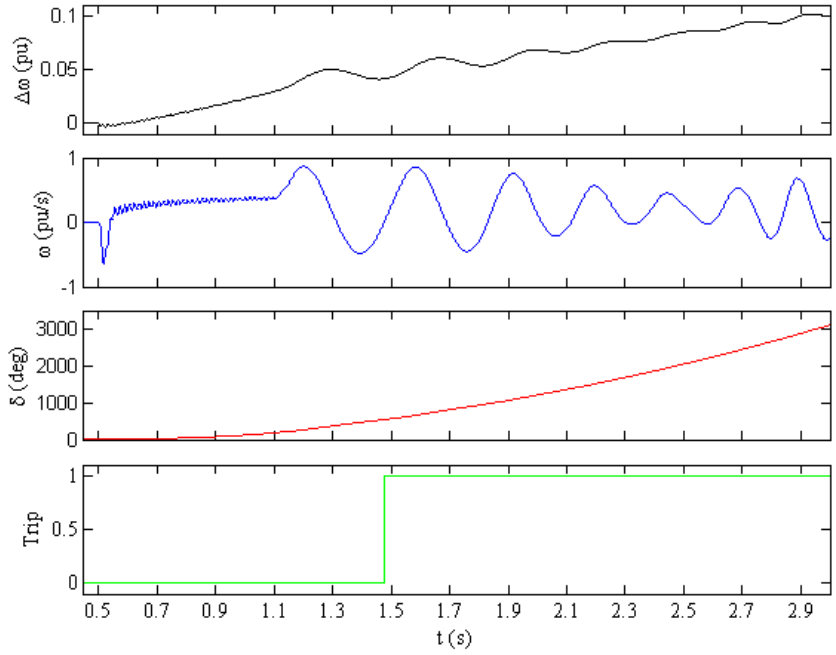

Figure 3.15: $\Delta\omega$), rate of change of relative speed ($\dot{\Delta\omega}$), power angle (δ) and loss of synchronism detection signals during an unstable scenario

Sensitivity for Small Disturbances

Seven (7) unit tripping scenarios with no faults were analysed under this category. This includes four transmission line openings ($L34$, $L45$, $L35\_1$ and $L35\_1 + L35\_2$), two load disconnections (at bus 4 and 5) and one generator disconnection (for this disturbance, the test system is slightly modified by duplicating the generator at bus 2 for the purpose of tripping one). Five out of seven scenarios created stable power swings in the test network. Unstable power swings were created in the bus 4 load tripping scenario and the bus 2 generator tripping scenario. In all seven scenarios, the relay successfully detected stable or unstable power swings. Figure 3.16 shows the results of generator tripping scenario where loss of synchronism condition is occurred due to deceleration of the machine.

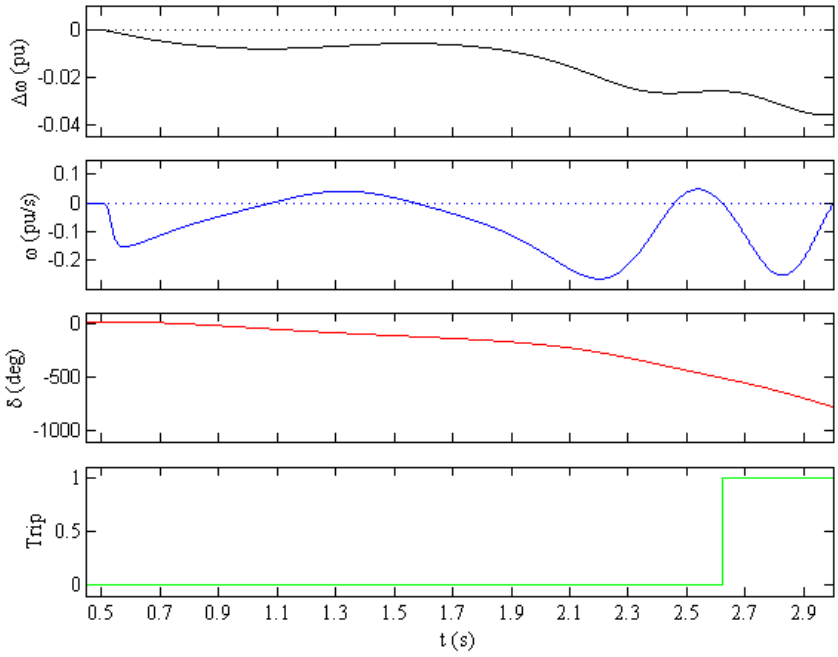

Figure 3.16: Generator loss of synchronism condition due to deceleration

3.4.3 Possible Mis/Delayed Operation Scenarios

In one of the simulated scenarios (see Figure 3.17) out of the 96 fault cases analyzed in Section 3.4.2, the loss of synchronism detection algorithm failed to identify the first pole slip. However, it successfully detected the second pole slip and issued the trip signal accordingly. This scenario is unique in that the rotor decelerated during the fault but accelerated in the post-fault region. As a result, the first and second maximums of the relative speed crossed the zero axis with opposite polarities, which the loss of synchronism detection algorithm interpreted as a stable condition.

The third maximum, occurred on the same side as the second maximum (as expected due to loss of synchronism condition), with adjacent maximums having the same polarity. This triggered the loss of synchronism detection algorithm. In sum-

mary, there is a possibility that the proposed method might miss the first pole slip in scenarios where the rotor accelerates during the fault and decelerates (and goes loss of synchronism) in the post-fault region, or vice versa.

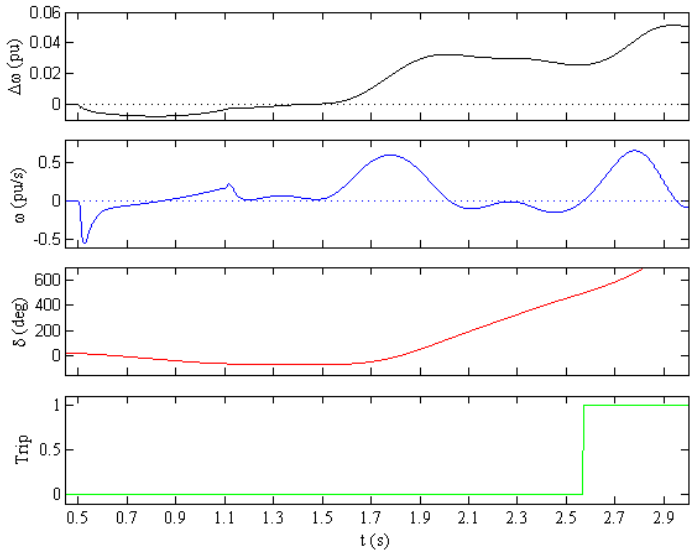

Figure 3.17: Marginal mis-operation of the proposed algorithm at the first pole slip but correct operation at the second slip

3.4.4 Comparison with Other Methods

The performance of the proposed method was evaluated in comparison with the double blinder and rate of change of voltage (ROCOV) schemes [3]. Both schemes were implemented in PSCAD/EMTDC, as outlined in Section 3.3.2. The same fault scenarios described in Section 3.4.2 were used for performance comparison. The results for a stable and an unstable scenario are presented in Figures 3.18 through 3.22.

As shown in Figure 3.22, the ROCOV scheme delivered the fastest tripping for an unstable power swing. Unlike impedance base methods or the proposed method (where the trip decision is made using two measured quantities), the ROCOV trip

decision is made based on a single measured quantity crossing of a user-defined boundary. Therefore, ROCOV characteristic can be highly influenced by the dynamics of rest of the system. Hence it is difficult to calculate a single ROCOV settings which works for all the conditions. In other words, generalization the operation of ROCOV scheme is strenuous. The settings used for this example is obtained by several time domain simulation iterations ranging from stable power swings to highly unstable power swings for many network conditions. Figure 3.19 shows the user-define boundary and the ROCOV vs DeltaV trajectories.

Compared to the double blinder scheme, the proposed method has operated faster (see Figure 3.22). This is because the proposed method has issued the trip signal at the first pole slip while the double blinder scheme has issued the trip signal when the calculated impedance is leaving the supervisory Mho circle following the first pole slip (i.e. trip on the way out). When the blinder scheme is set to "trip on the way in", faster trip timings were observed. This is because the "trip on the way in" scheme issues trip signals prior to actual pole slip. Figure 3.18 shows the impedance trajectories, blinders and supervisory Mho circle used in the study. In addition, impedance based schemes are inherently slower compared to the instantaneous value based techniques due to use of Discrete Fourier Transform (DFT) based phasor calculation technique. The blinder and timer settings were determined as detailed in Appendix B.2.

Figure 3.20 shows the estimated relative speed trajectories used by the proposed method to detect a loss of synchronism condition. The proposed algorithm detected the loss of synchronism condition at the second maximum/minimum of the unstable

ω vs t trajectory at around 0.9s. The instantaneous voltages and currents which were used to estimate relative speed in the proposed algorithm along with the estimated speed are depicted in Figure 3.21.

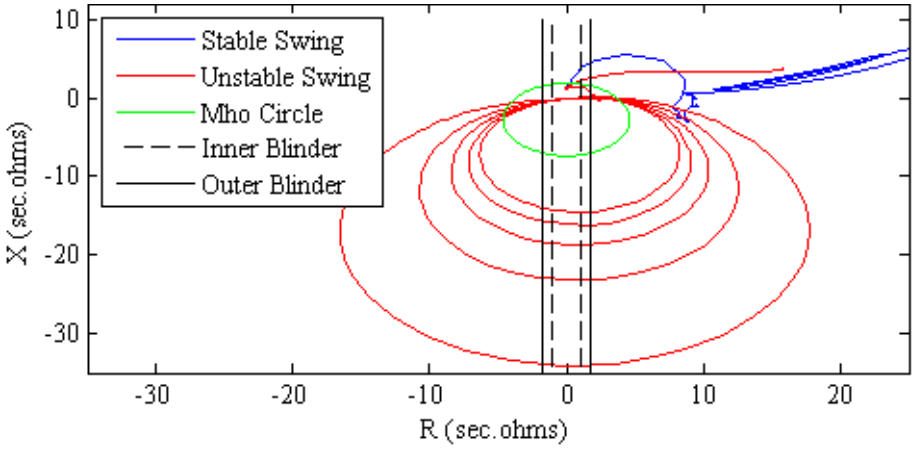

Figure 3.18: Impedance trajectories of the double blinder scheme

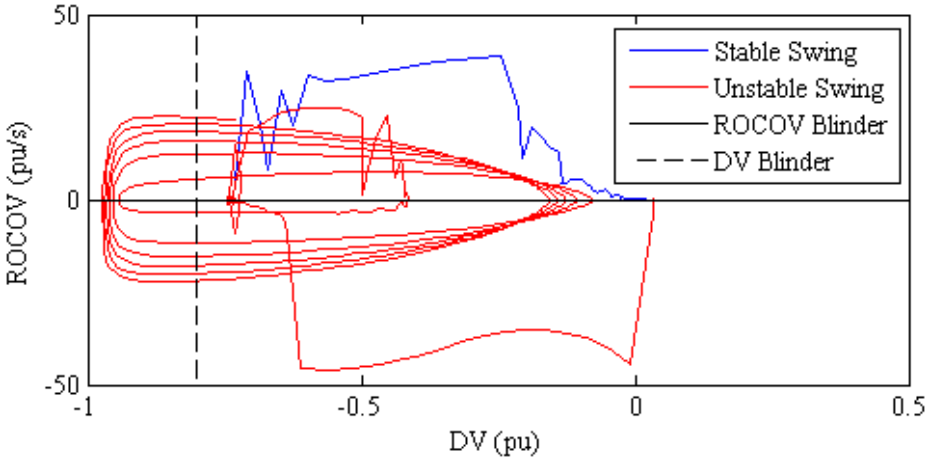

Figure 3.19: ROCOV vs DeltaV trajectories of ROCOV loss of synchronism scheme

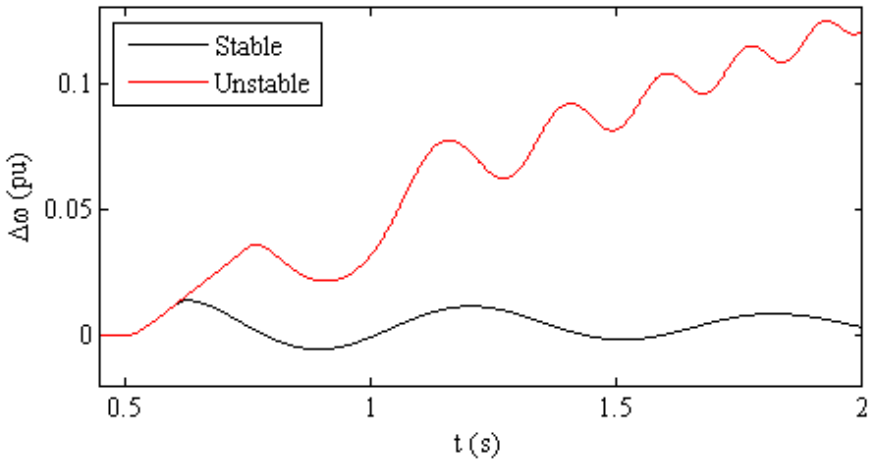

Figure 3.20: ω vs t trajectories used by the proposed method

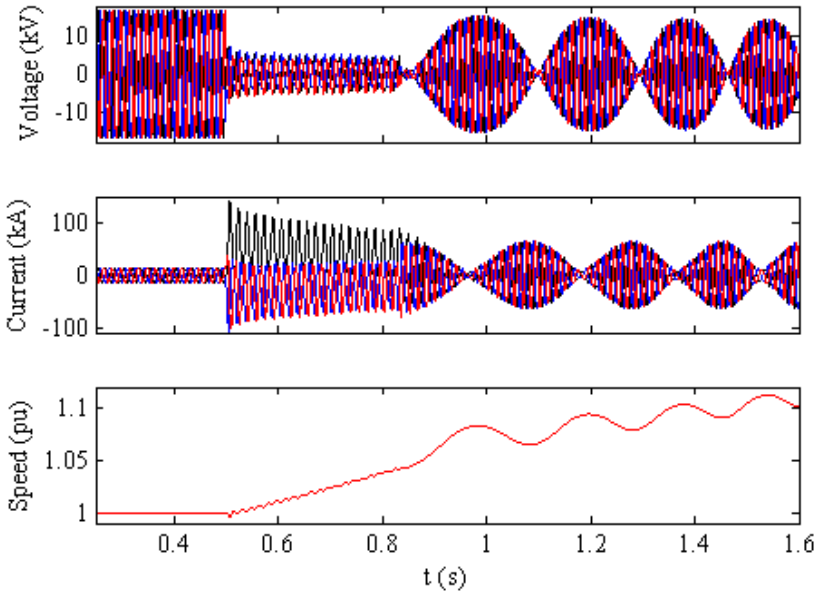

Figure 3.21: Generator terminal voltage, current and speed for the unstable scenario

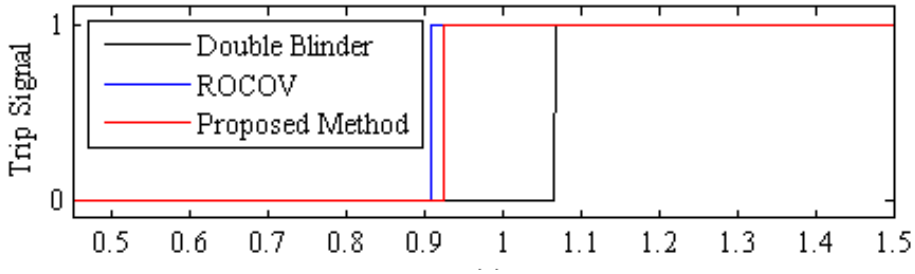

Figure 3.22: Trip timings of double blinder, ROCOV and proposed loss of synchronism schemes for the unstable power swing

3.5 Concluding Remarks

Generator speed serves as a direct indicator of a loss of synchronism condition, as disturbances causing energy imbalances in a generator lead to speed variations. Based on this principle, a novel approach for detecting loss of synchronism conditions in synchronous generators is proposed. This method utilizes estimated relative rotor speed to detect loss of synchronism condition. The method comprises two key components: a "speed estimation algorithm" and an "loss of synchronism detection algorithm". The speed estimation algorithm calculates the relative speed and its rate of change using terminal voltage and current measurements, along with generator parameters. To validate the accuracy of the estimated relative speed, sensitivity studies were performed, addressing generator data variations, measurement errors, and stator transients. These calculated relative speed values are then used as inputs for the loss of synchronism detection algorithm.

The loss of synchronism detection algorithm evaluates rotor speed variations following a disturbance, identifying a loss of synchronism condition if the relative speed consistently increases or decreases within a swing cycle. It classifies a power swing as unstable if the relative speed at fault clearance and the first minimum (or maximum) share the same polarity. Alternatively, the algorithm can be configured to assess the polarity of subsequent minimums and maximums, accommodating scenarios where the generator allows one or more pole slips.

The proposed relative speed based method was implemented as a custom component in PSCAD/EMTDC. Time-domain simulation tests demonstrated its effective-

ness, with results comparable to or better than those of traditional methods, such as double-blinder loss of synchronism relays and rate-of-change-of-voltage (ROCOV) relays. The method offers enhanced reliability and security, with less critical threshold settings that reduce the need for frequent adjustments based on network conditions.

Chapter 4

Synchronous Condenser Loss of Synchronism Phenomenon and Protection

4.1 Introduction

In traditional power systems, synchronous condensers were primarily employed for voltage and reactive power support. Conversely, in present, the emphasis has shifted towards leveraging synchronous condensers for enhancing short circuit strength and providing inertia support. Hence, synchronous condensers are now being observed in remote regions with high penetration of inverter-based resources (IBRs). Disturbances in these remote regions are more likely to result in voltage and/or angular instabilities which may ultimately result in loss of synchronism (also known as out-of-step (OOS) condition) of synchronous condensers. These instabilities or oscillations

increase mechanical stresses on their shafts. High rotor iron currents and increased winding stress may also be observed as subsequent consequences [9]. All of these effects are potentially damaging to the synchronous condenser or reducing its life time. Prompt disconnection of the systems or synchronous condensers which are operating asynchronously is important to avoid such undesired outcomes [8].

Currently, a few methods exist for providing loss of synchronism protection for synchronous condensers using measured terminal quantities, machine data, and system information. However, these methods exhibit limitations in reliably detecting loss of synchronism conditions in synchronous condensers. A detailed discussion on traditional loss of synchronism protection methods for synchronous condensers, along with their advantages and drawbacks, is provided in Chapter 2, Section 2.3.

To overcome these limitations, the proposed relative speed-based loss of synchronism detection scheme, originally designed for synchronous generators, is applied to synchronous condensers. The effectiveness of the proposed method for loss of synchronism detection in synchronous condensers is validated through EMT simulations, and its sensitivity to various power system parameters is thoroughly analyzed.

This chapter is organized as follows. Section 4.2 analyzes the loss of synchronism phenomenon in synchronous condensers. Section 4.3 clarifies the loss of synchronism and pole slipping phenomenons in synchronous condensers. Application of proposed loss of synchronism protection scheme for synchronous condensers is discussed in Section 4.4. In Section 4.6, the results of three unique case studies performed using modified Kundur's two-area test system are discussed. Finally, concluding remarks are presented in Section 4.7.

4.2 Loss of Synchronism Phenomenon of a Synchronous Condenser

If the network adjacent to a synchronous condenser is subjected to a large disturbance its terminal voltage angle deviates relative to the rest of the system, typically, the voltage angle oscillates while the synchronous condenser is still in synchronism with the power system. This oscillation can becomes either stable or unstable, based on the magnitude of the oscillation. If the voltage angle deviation exceeds a certain critical value, then the synchronous condenser loses its synchronism with the system. Often synchronous condensers resynchronize with the system after few swing cycles; however, in certain instances, they may continue to accelerate, potentially leading to sustained instability. This behaviour is primarily influenced by the active power dynamics in the synchronous condenser (SC) subsystem during the fault, as well as the overall system's post-fault recovery characteristics.

4.2.1 Synchronous Condenser Loss of Synchronism

Loss of synchronism of a synchronous condenser is analysed under two unique scenarios. Namely,

1. Loss of synchronism of a synchronous condenser without nearby IBRs
2. Loss of synchronism of a synchronous condenser with near by IBRs

Above two scenarios are analysed in detailed below.

Loss of synchronism of a synchronous condenser without nearby IBRs

To derive the power-angle relationship necessary for determining the critical clearing angle of a fault nearby a synchronous condenser, a two-machine test system illustrated in Figure 4.1 is employed. In this configuration, the synchronous condenser is modelled as a voltage source behind an impedance, while the rest of the system is represented by an equivalent generator connected through a transmission line. The internal voltage of the synchronous condenser, the voltage at the POI, and the voltage of the equivalent generator are denoted as $E_a\angle\delta_a$, $V_t\angle\delta_t$, and $E_b\angle\delta_b$, respectively. Since the synchronous condenser neither generates nor consumes significant active power, the angles δ_a, δ_b, and δ_t are assumed to be in phase. The minor active power absorption to compensate resistive losses in the synchronous condenser is neglected for this analysis.

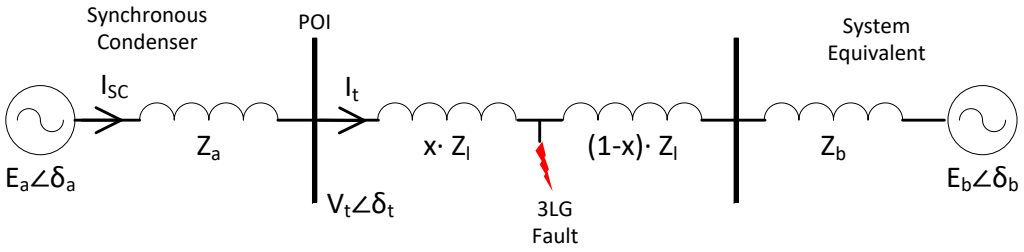

Figure 4.1: The test system consisting of two machines with a temporary 3LG bolted fault at mid line

Under steady-state conditions, all voltage angles within the test network are approximately equal, resulting in negligible angle differences and, consequently, insignificant active power flow. A temporary three-phase-to-ground bolted fault is then applied at the midpoint of the transmission line connecting the synchronous condenser

and the equivalent generator. During the fault, the system effectively splits into two electrically decoupled subsystems, forming two distinct islands. The island containing the synchronous condenser lacks any devices capable of generating or absorbing active power. As a result, the synchronous condenser neither accelerates nor decelerates during the fault period.

Following fault clearance, the voltage angle of the synchronous condenser remains effectively unchanged from its pre-fault value, and the frequency remains nearly constant. While there may be a slight deceleration due to uncompensated resistive losses, the impact is minimal and does not significantly affect system dynamics. Consequently, the voltage angle remains nearly constant, and the system is expected to remain stable regardless of the fault duration.

Figure 4.2 illustrates the terminal voltage angle of the SC subsystem relative to the system. Since no active power source is available in the SC subsystem during the fault period, the accelerating energy (i.e., area A_1) would be zero. As a result, the two subsystems would not experience a loss-of-synchronism condition. Thus, area A_2 is always greater than area A_1, independent of the fault duration. Therefore, the concept of a critical clearing angle is not applicable for a synchronous condenser operating independently within the subsystem formed during the fault.

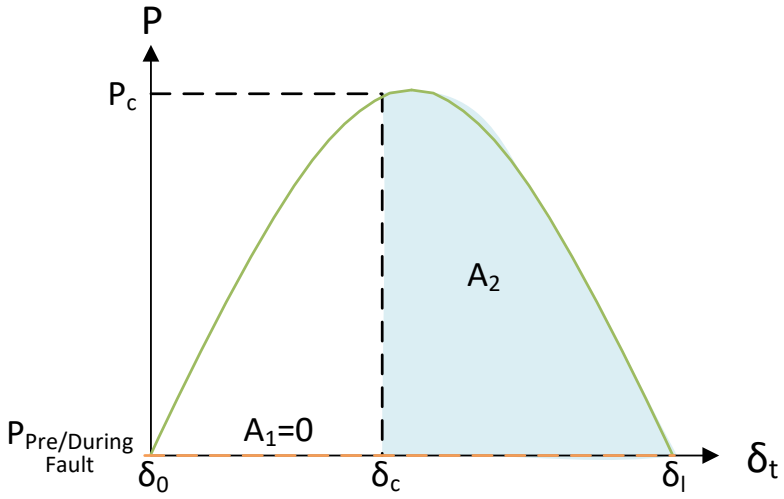

Figure 4.2: Synchronous condenser terminal voltage angle relationship with respect to δ_b (for the system shown in Figure 4.1).

Loss of synchronism of a synchronous condenser with nearby IBRs

To determine the critical clearing angle of a fault close to a synchronous condenser with nearby IBRs, a similar two-machine test system illustrated in Figure 4.3 is employed. In this test system, synchronous condenser is connected at the POI of an IBR to provide short circuit strength. Rest of the test system is similar to the one discussed in Section 4.2.1.

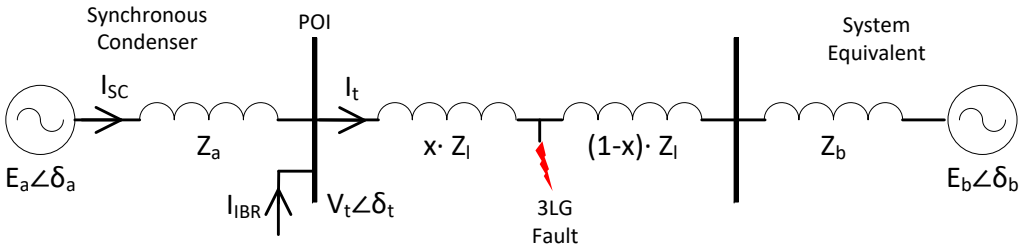

Figure 4.3: The test system consisting of two machines and an IBR with a temporary 3LG bolted fault at mid line

Under steady-state conditions, the terminal voltage angle of the SC relative to

the equivalent generator is δ_t (given that $\delta_b = 0$), resulting from the active power flow through the transmission line driven by the IBR generation. However, the power angle (angular displacement between the internal stator voltage and the terminal voltage) of the SC is nearly zero due to the negligible active power flow through its stator reactance. As illustrated in Figure 4.5, δ_{ta} (=δ_t- δ_a) ≈ 0 under steady-state operation.

A temporary three-phase-to-ground bolted fault is introduced at the mid point of the transmission line between synchronous condenser and the equivalent generator (this is a simplified representation of scenario where a fault is applied and the faulted line is disconnected in a double circuit line). During the fault, the terminal voltage of the synchronous condenser drops. However, due to the injection of reactive current from both the IBR and the synchronous condenser, as well as the remote location of the fault (at the mid point of the transmission line), the voltage drop at the synchronous condenser terminal is not significant. Consequently, the IBR is able to maintain active power injection during the fault period. In other words, synchronous condenser forms an island during the fault with an active power producer.

The active power generated by the IBR during the fault, having no immediate path for delivery, leads to continuous acceleration of the SC until the fault is cleared. This results in an increasing voltage angle of the SC subsystem with respect to the rest of the system. Upon fault clearance, active power transfer to the network resumes, causing the SC to decelerate. However, since its rotational speed remains above nominal, the voltage angle continues to increase. This dynamic response is analogous to the classical loss of synchronism phenomenon observed in synchronous generators,

where system stability is determined by the critical clearing time/angle. Accordingly, a synchronous condenser with nearby IBRs possesses a critical clearing time, which is influenced by the system parameters and the IBR's active power dispatch levels.

Figure 4.4 illustrates the terminal voltage angle of the SC subsystem relative to the rest of the system. If area A_2 is smaller than area A_1, the two subsystems will experience loss of synchronism condition.

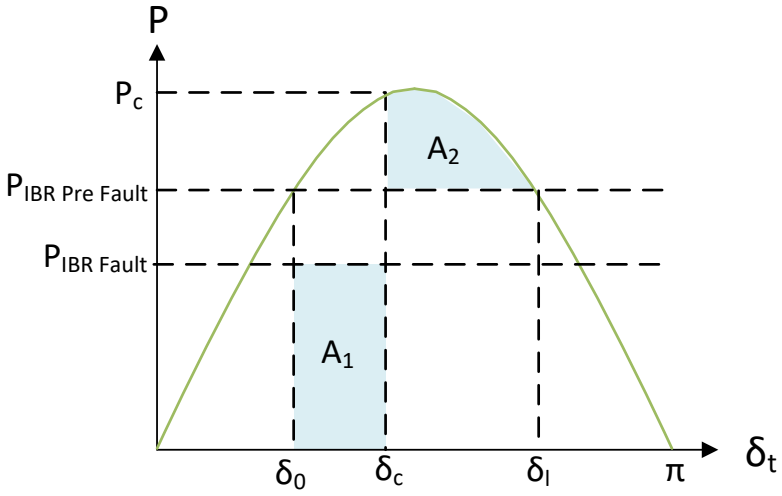

Figure 4.4: Synchronous condenser terminal voltage angle relationship with respect to δ_b (for the system shown in Figure 4.3).

Figure 4.5 presents the variation in the power angle of the SC, defined as the angular displacement between the internal stator voltage and the terminal voltage. The trajectory of the power angle during the disturbance is indicated by the red arrows. The maximum power angle reached by the SC is predominantly governed by the magnitude of active power injected by the IBR during the fault period. This implies that the fault duration has a negligible effect on the maximum angle attained; rather, it is the level of active power that serves as the determining factor. As a result, under typical system operating conditions, the occurrence of pole slipping in the SC

either during or following fault clearance is highly improbable.

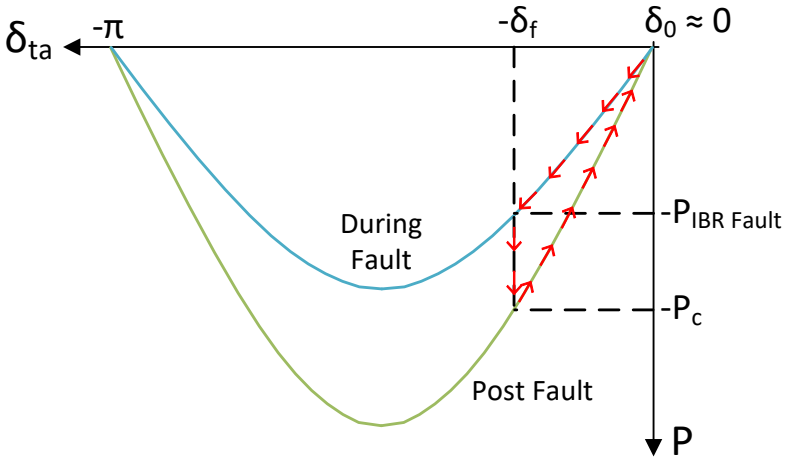

Figure 4.5: Synchronous condenser power angle relationship with respect to its terminals (for the system shown in Figure 4.3).

4.2.2 Impedance Relationship of a Synchronous Condenser

One of the well established traditional methods to analyze a loss of synchronism condition is to examine the trajectory of impedance seen from the synchronous condenser terminals. During a loss of synchronism condition, the impedance seen by the synchronous condenser varies depending on the voltage magnitude and angular difference between internal and terminal quantities (i.e. power angle). Most protective devices calculate this variation of impedance to determine a loss of synchronism condition [17–20].

The best way to illustrate this variation of the apparent impedance at the terminal of the synchronous condenser is by using a simple test system as shown in Figure 4.3. δ_b is lagging with respect to δ_t since the IBR injects active power and the equivalent generator absorbs it. δ_a is also lagging slightly behind δ_t, since the synchronous

condenser is absorbing a small amount of real power. Additionally, it is assumed that the synchronous condenser is operating with a leading Power Factor (PF).

The impedance seen by the relay at the synchronous condenser terminals can be calculated as follows:

$$V_t = E_a - I_{sc} \cdot Z_a = I_t \cdot (Z_l + Z_b) + E_b \tag{4.1}$$

$$Z_t = \frac{V_t}{I_{sc}} = \frac{I_t \cdot (Z_l + Z_b)}{I_{sc}} + \frac{E_b}{I_{sc}} \tag{4.2}$$

The phasor relationship described by (4.1) and (4.2) are shown in Figure 4.6.

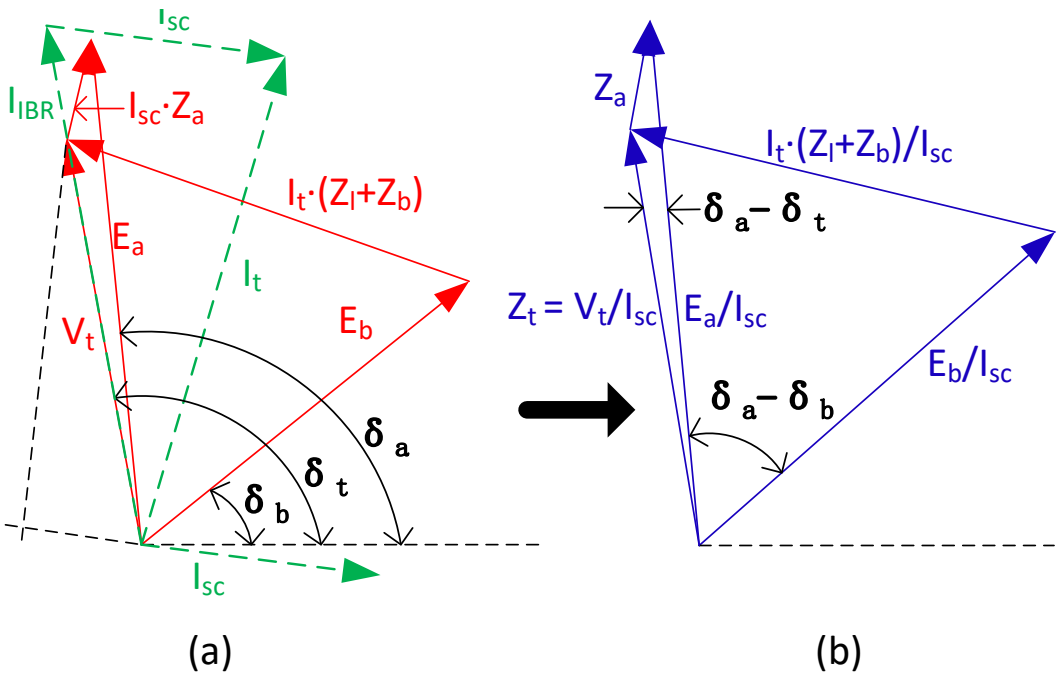

Figure 4.6: (a) Voltage (in red) and Current (in green), (b) Impedance (in blue) phasors of the test system shown in Figure 4.3. The voltage phasors in (a) were converted into impedance phasors in (b) by dividing all voltage drops by current I_{sc}.

The impedance phasors from Figure 4.6 (b), placed on the real and imaginary axis plane, are depicted in Figure 4.7. Similar diagrams were obtained by replacing the

synchronous condenser with a generator and a motor as shown in Figure 4.8 and 4.9, respectively. The synchronous generator is assumed to be operating with a lagging PF, while the synchronous motor is with a leading PF. IBR is not considered in the Synchronous generator and motor applications. Supervisory mho circle of a double blinder protection scheme is also shown in all impedance diagrams to highlight the potential for loss of synchronism relay pick up.

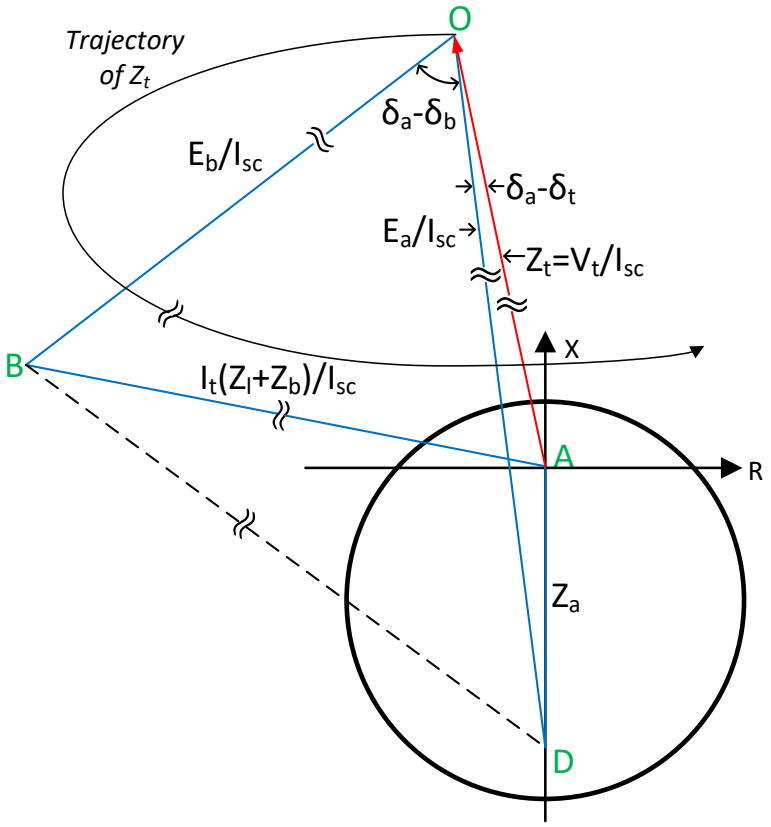

Figure 4.7: Impedance seen by the synchronous condensers (in red) during a power swing. The black circle represents a typical mho scheme.

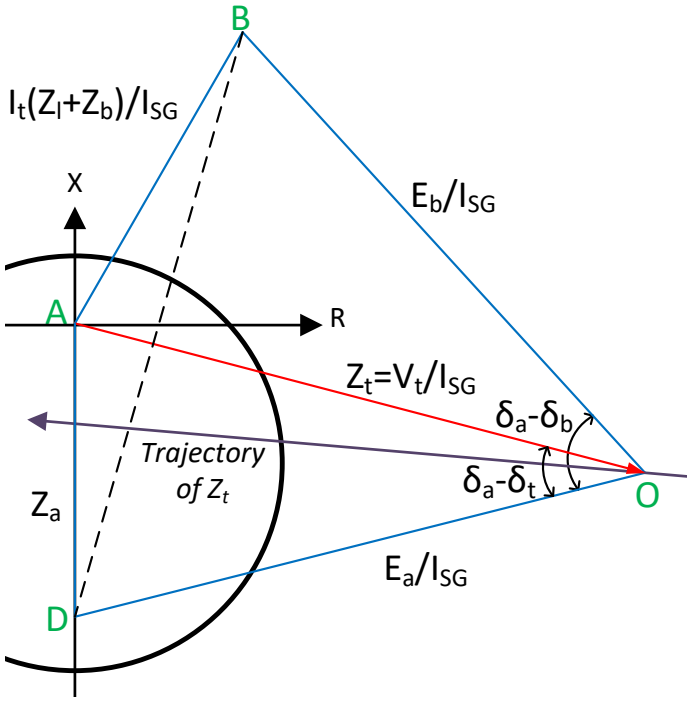

Figure 4.8: Impedance seen by the synchronous generator (in red) during a power swing. The black circle represents a typical mho scheme.

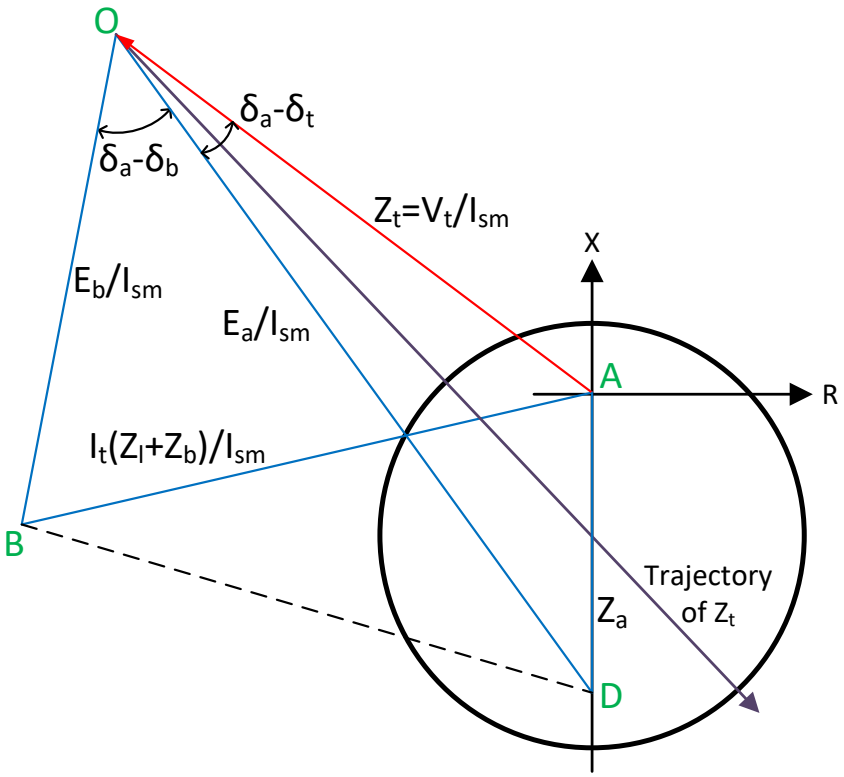

Figure 4.9: Impedance seen by the synchronous motor (in red) during a power swing. The black circle represents a typical mho scheme.

To enhance clarity, the example of a synchronous generator will be examined first. An oscillation may cause E_a and δ_a to deviate from their pre-disturbance values. Hence, the terminal voltage (V_t), synchronous generator terminal current (I_{SG}) and the vector V_t/I_{SG} may also vary. If the disturbance is sufficiently large, the impedance seen by the relay (red phasor in Figure 4.8) can move into the relay operating zones. The power angle δ ($= \delta_a - \delta_t$) increases and the impedance magnitude seen by the relay decreases and it may fall inside the relay operating characteristic.

A similar behaviour is observed in the synchronous motor scenario as well. The terminal voltage (V_t), synchronous motor terminal current (I_{SM}) and the vector V_t/I_{SM} may vary during the disturbance and the impedance seen by the relay (red phasor in Figure 4.9) can move into the relay operating zones.

In the case of synchronous condenser, where pre-disturbance impedance is almost on the reactance axis (see Figure 4.7), the chance of impedance seen by the synchronous condenser relay move into operating zone is much lower. Therefore, the probability of impedance trajectory crossing the line AD is very low. The point where the impedance locus intersects the total impedance line between B and D is called the electrical centre of the system. At this point, the two generators are 180^{o} out of phase with each other. In the proper scale, the ratio of lengths AB:AD in Figure 4.7 is significantly larger than the same of synchronous generator. As an example, $(AB : AD_{SC})/(AB : AD_{SG}) > 5$. In other words, the swing centre is located more towards outside of line AD.

4.2.3 Trajectory of Synchronous Condenser Impedance During Transients

The trajectory of impedance seen by the relay at the synchronous condenser terminals for different E_a/E_b ratios (i.e. the ratio of voltage magnitudes of the two machines in Figure 4.3) can be calculated as follows:

From (4.1), the measured impedance at the synchronous condenser terminal can be written as:

$$Z_t = \frac{V_t}{I_{sc}} = \frac{E_a}{I_{sc}} - Z_a \tag{4.3}$$

The total terminal current (I_t) can be written in terms of the network quantities beyond the POI and also using current summation as:

$$I_t = \frac{V_t - E_b}{Z_l + Z_b} = I_{sc} + I_{IBR} \tag{4.4}$$

Substituting (4.1) in (4.4) and subjecting I_{SC} gives:

$$I_{sc} = \left[\frac{(E_a - I_{sc} \cdot Z_a) - E_b}{Z_l + Z_b}\right] - I_{IBR} \tag{4.5}$$

Subjecting I_{SC} in (4.5) gives:

$$I_{sc} = \frac{E_a - E_b - I_{IBR}(Z_l + Z_b)}{Z_a + Z_l + Z_b} \tag{4.6}$$

Substituting (4.6) in (4.3) and rearranging the term E_a/E_b gives:

$$Z_t = \frac{Z_a + Z_l + Z_b}{1 - \frac{E_b}{E_a} - \frac{I_{IBR}}{E_a}(Z_l + Z_b)} - Z_a \tag{4.7}$$

Lets assume, $E_b = 1\angle 0$ and $E_a = k\angle\delta$. Then $E_a/E_b = k\angle\delta$. Therefore, (4.7) can be re-written as a function of k and δ as:

$$Z_t(k, \delta) = \frac{Z_{total}}{1 - \frac{1}{k\angle\delta} - \frac{I_{IBR}(Z_l+Z_b)}{k\angle\delta}} - Z_a \tag{4.8}$$

The trajectories of impedance seen by the terminal relay for different E_a/E_b ratios are depicted in Figure 4.10. The current injection from the IBR is assumed constant during the power swings due to its fast current controllers.

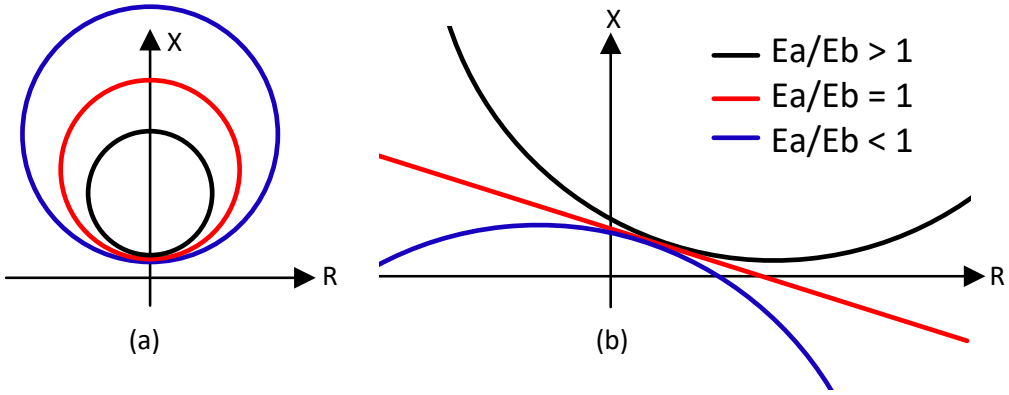

Figure 4.10: Impedance trajectories of (a) synchronous condenser and (b) synchronous generator (without IBR) for different E_a/E_b ratios.

For a synchronous generator (without IBR), the impedance locus seen by the relay during a power swing forms a straight line if $|E_a| = |E_b|$, as illustrated in Figure 4.10-(b). However, in this synchronous condenser example, the impedance locus is not necessarily a straight line, because it is also influenced by the current injection

from the IBR. For example, when the synchronous condenser is sized at less than half of the IBR facility rating, the impedance loci appear as a family of circles on the positive reactance plane, as shown in Figure 4.10-(a). If $|E_a|$ is not equal to $|E_b|$, the impedance locus for a synchronous generator forms a family of circles centered on the BD axis (See BD axis of a SG in Fig. 4.8). In contrast, for an synchronous condenser under the same conditions, the impedance locus is not necessarily a family of circles.

In all three scenarios above, if the angle $A\hat{O}D$ in Figure 4.7 to 4.9 reaches 120° and goes beyond, the system is not likely to recover, which is a typical assumption in setting loss of synchronism protection relays for synchronous generators. In the synchronous condenser scenario, the probability of angle $A\hat{O}D$ reaching 120° is significantly less compared to synchronous generator and synchronous motor scenarios. As the locus keeps moving away from the reactance axis, the angular separation increases beyond 180°, thereafter the two machines move into phase again. Once the two machines in Figure 4.3 are back into phase again with each other, the machines have completed one slip cycle. If the impedance trajectory crosses the reactance axis outside of AD, the angle $A\hat{O}D$ will not reach 180°. This means that the swing center is not within the machine impedance. The system may still experience a loss of synchronism condition but synchronous condenser may not experience poles slipping.

4.3 Loss of Synchronism and Pole Slipping

In the context of Synchronous Condensers, it is important to note a distinction from Synchronous Generators regarding 'loss of synchronism" and "pole slipping"

phenomenon. Loss of synchronism is a condition where synchronous condenser loses its synchronism with the rest of the system. The condition of pole slipping occurs when the angle difference between synchronous condenser's stator magnetic field and the rotor field exceeding 180°. Unlike synchronous generators, where these events typically coincide (i.e. loss of synchronism condition and pole slipping usually occur together or within few milliseconds), in the case of synchronous condensers, they may not always occur simultaneously. This means that a synchronous condenser can operate asynchronously with respect to another generator or the system without slipping poles. This may also define as line out-of-step condition in some context due to swing center is not being located within the synchronous condenser impedance even though the loss of synchronism condition is triggered due to oscillation of synchronous condenser against the system. This highlights an unique operational characteristic of synchronous condensers, where traditional generator loss of synchronism protection schemes fail since they rely on the pole-slipping condition.

Since synchronous condenser does not produce or absorb significant amount of steady state active power, the initial power angle is relatively small (power angle only accounts for the real power consumption of the synchronous condenser to compensate its losses). Therefore, the probability of pole slipping in synchronous condensers are relatively low compared to synchronous generators or synchronous motors. However, synchronous condensers may experience loss of synchronism condition with respect to another generator or the system without slipping poles. In other words, since the angle between terminal and internal voltages are relatively small they may not oscillate against each other but can oscillate against the system.

4.4 Application of Proposed Scheme on Synchronous Condensers

A novel loss of synchronism protection scheme based on the relative speed of rotation has been developed for synchronous generators, as detailed in Chapter 3 [55]. The algorithm identifies a power swing as unstable if the relative speed measured at fault clearance and at the first maximum has the same polarity. Conversely, it classifies the swing as stable if the polarities are opposite. The algorithm can also be configured to analyze the polarity of multiple maximums, accommodating scenarios where the machines allow one or more power swings (not necessarily pole slips). Further details on the proposed scheme, including its implementation and validation, are presented in Chapter 3.

The proposed scheme leverages relative speed as a direct indicator of loss of synchronism conditions, as speed variations arise from energy imbalances caused by disturbances within the machine. This property is not exclusive to synchronous generators but is applicable to any synchronous machine. Speed variations are directly correlated with the active power response during and after a fault, making this approach equally relevant for both synchronous generators and condensers. As a result, the proposed method can be directly applied to detect loss of synchronism conditions in synchronous condensers without requiring modifications to the loss of synchronism detection algorithm.

In fact, the method is particularly well-suited for synchronous condensers, as they

lack the slow-moving governor dynamics which are present in synchronous generators but not considered in the proposed algorithm. Thus, the algorithm provides a robust means of detecting loss of synchronism conditions in synchronous condensers without relying on pole-slipping, a common requirement in many traditional loss of synchronism protection schemes for synchronous machines.

4.5 Implementation in an EMT Program

The proposed method was implemented in PSCAD/EMTDC to evaluate its performance and examine its sensitivity to various factors. The implementation details are already discussed in Chapter 3 Section 3.3.1. To benchmark the proposed method, several well-established techniques from the literature were also implemented in PSCAD/EMTDC. These included the single blinder scheme [1], notching relay [43], field AC overcurrent element [44, 45], and the loss of excitation scheme [10]. Implementation details of these other methods are discussed in Section 4.5.1.

An eight bus network based on Kundur's two-area test system [48], incorporating a variety of passive and dynamic components such as synchronous condensers, IBRs, transmission lines, transformers, and loads, was employed as the test setup for performance evaluation. In this modified system, Generator No. 3 (G_3) from the original Kundur's test system is replaced with a synchronous condenser, and Generator No. 4 (G_4) is replaced with a wind plant model. Additionally, the machines in Area 1 are aggregated into a system equivalent represented by a voltage source behind an impedance. The single-line diagram of the test network is shown in Figure

4.11. The network and machine parameters of the modified test system can be found in Appendix A.2.

The modelling of the synchronous condenser was based on field data provided by Manitoba Hydro, which included both machine parameters and exciter dynamic data. To represent the IBR, generic Type 4 (full converter) and Type 3 (DFIG) wind farm models were utilized. A plant controller model, representing both active and reactive power control algorithms, was used to generate power dispatch commands for the wind turbine generators (WTGs). The modelling of IBRs for protection validation studies are discussed in detailed in Appendix C. The modelling of passive devices followed a similar methodology to that described in Chapter 3 Section 3.4.

The test network was initially modelled in PSS/E and subsequently converted into PSCAD using the E-TRAN tool [53] to ensure accurate initial conditions, including generator bus voltage magnitudes, angles, and transformer tap positions.

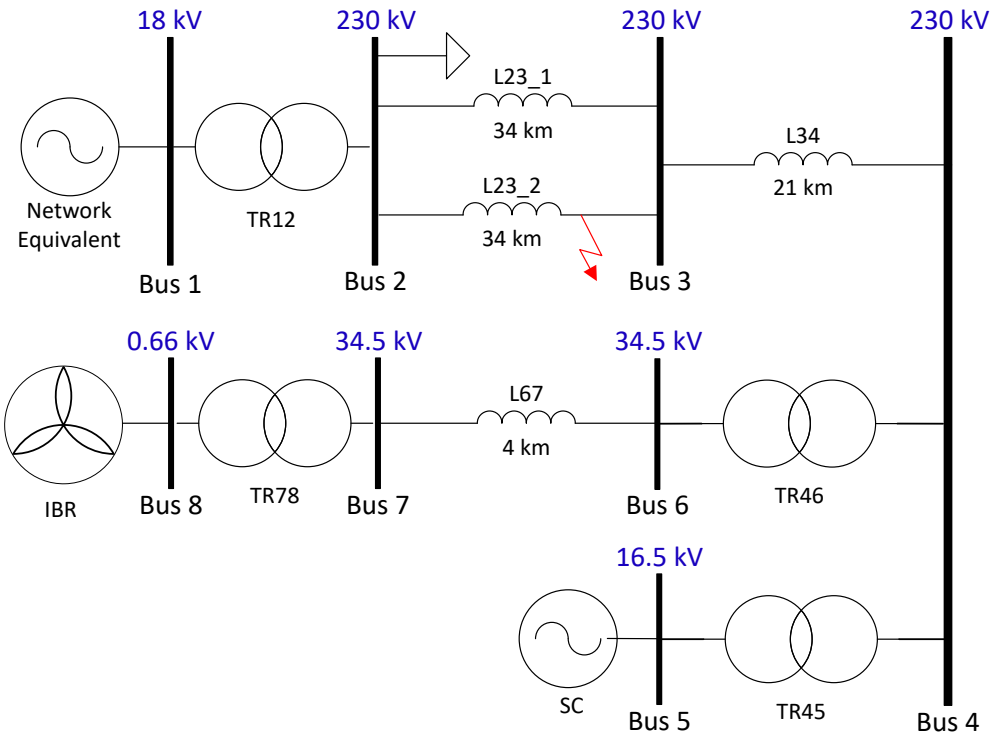

Figure 4.11: The modified Kundur's two-area test network developed for synchronous condenser loss of synchronism protection validation studies

4.5.1 Implementation of Traditional Synchronous Condenser Loss of Synchronism Protection Schemes

To benchmark proposed method against established synchronous condenser loss of synchronism methods, several widely recognized methods from the literature were implemented in PSCAD/EMTDC. These included the single blinder scheme [1], notching relay [43], field AC over-current element [44, 45], and loss of excitation scheme [10].

Single Blinder Schemes

The single blinder scheme is implemented as a custom component, aligning with the operational principles outlined in the instruction manual of the SEL-700G [51]. Similar to double blinder scheme, the implementation incorporates a direct fourier transformation (DFT) algorithm coupled with an anti-aliasing filter to derive positive sequence phasors. A sampling rate of 16 samples per cycle is employed. Impedance is then calculated at each processing time step and evaluated in accordance with the principles outlined in [51]. The relay settings are configured adopting the methodology used by Manitoba Hydro and impedance characteristics of the test system, as detailed in Appendix B.1.

Notching Relay

Pole slips cause an oscillatory behaviour in phase currents and voltages, which can temporarily result in a reversal of current flow. The notching relay scheme is designed to detect these reversals, typically by counting them within a specified time frame, and initiate operation if a maximum count is reached [44]. This scheme is implemented as a custom component, following the operational principles outlined in the "supplementary instructions of the Westinghouse loss of synchronism notching relay (Type KSN) [56]". The implementation comprises two main units: the loss of synchronism unit and the notching unit. The loss of synchronism unit incorporates a directional element and an over current element. If the terminal current exceeds a certain threshold and changes direction, operating impulses are transmitted to the

notching unit. After 7 impulses (i.e 3.5 pole slips), the relay issues a trip signal. The relay is configured as per the loss of synchronism setting calculation practice used by Manitoba Hydro, a utility in the province of Manitoba in Canada.

Field AC Over-Current Element

The Field AC over-current element, as described in [44, 45], employs a technique similar to the notching relay. Instead of counting pole slips, this method utilizes a high or band pass filter to eliminate the DC component from the field current. It then triggers an over-current element based on the AC content of the current. This scheme is implemented in PSCAD/EMTDC as a custom component. The field current measurement undergoes filtering using a band pass filter with cut-off frequencies of 1 and 50 Hz. Subsequently, the RMS value of the AC component is compared against a threshold of 0.2 pu for a duration of 0.5 s prior to executing the trip signal.

Loss of Excitation Scheme

Loss of excitation (LOE) protection schemes monitor changes in the impedance at the terminals of the synchronous machine to detect the loss of excitation condition. When the machine loses its excitation, the measured impedance changes significantly due to the absence of the magnetic field. This change in impedance is used as an indication of the loss of excitation condition. Positive sequence voltage and current phasors were calculated similar to single blinder scheme. Impedance is then calculated at each processing time step and evaluated in accordance with the principles outlined in [10]. The relay settings are configured based on the protection relay setting practice

of Manitoba Hydro, as detailed in Appendix B.3.

4.6 Case Studies

Three unique cases were analysed using the network in Figure 4.11. Several tests were performed on each case to verify the loss of synchronism phenomenons described in sections 4.2 and 4.3. This includes multiple fault types, locations, clearing times and power flow conditions which result in both stable and unstable power swings. These tests also validate the accuracy and security of the proposed method. The test setup, results and discussion of each case is presented in Sections 4.6.1 through 4.6.3.

4.6.1 Case 1: Loss of Synchronism Due to Rotor Acceleration

In this case, a three phase bolted fault is applied on bus 3 end of the transmission line $L23\_2$ (location A in Figure 4.11) and the line was tripped to clear the fault. Duration of the fault was adjusted to 6 cycles and 7 cycles to create stable and unstable power swings (i.e. critical clearing time is around 6 cycles).

As shown in Figure 4.12, the bolted fault at bus 3 caused windfarm terminal bus voltage to drop about 0.5 pu. Therefore, the active power output of the windfarm is reduced to about 200 MW (from 300 MW) during the fault. Since, the only transmission corridor in this test system lies on the faulted path, the power generated from WTGs cannot be delivered into the system (and loads). Therefore, this excess power is absorbed by the synchronous condenser (which is adjacent to WF) during

the fault. This results in synchronous condenser to accelerate during the fault (see Figure 4.13). If the fault is cleared after the critical clearing time, the synchronous condenser experiences a loss of synchronism condition as shown in Figure 4.16.

As shown in Figure 4.14, the internal voltage angle with respect to its terminal does not exceed 180° during the window of interest (1.5s). But the internal voltage angle with respect to infinite bus exceed 400° even before 1s showing that the synchronous condenser is experiencing a loss of synchronism against the system. This demonstrates the occurrence of a loss of synchronism condition in the system without the synchronous condenser subjecting to slipping poles. Instantaneous voltages and currents of the stable and unstable scenarios are depicted in Figure 4.15 and 4.16, respectively.

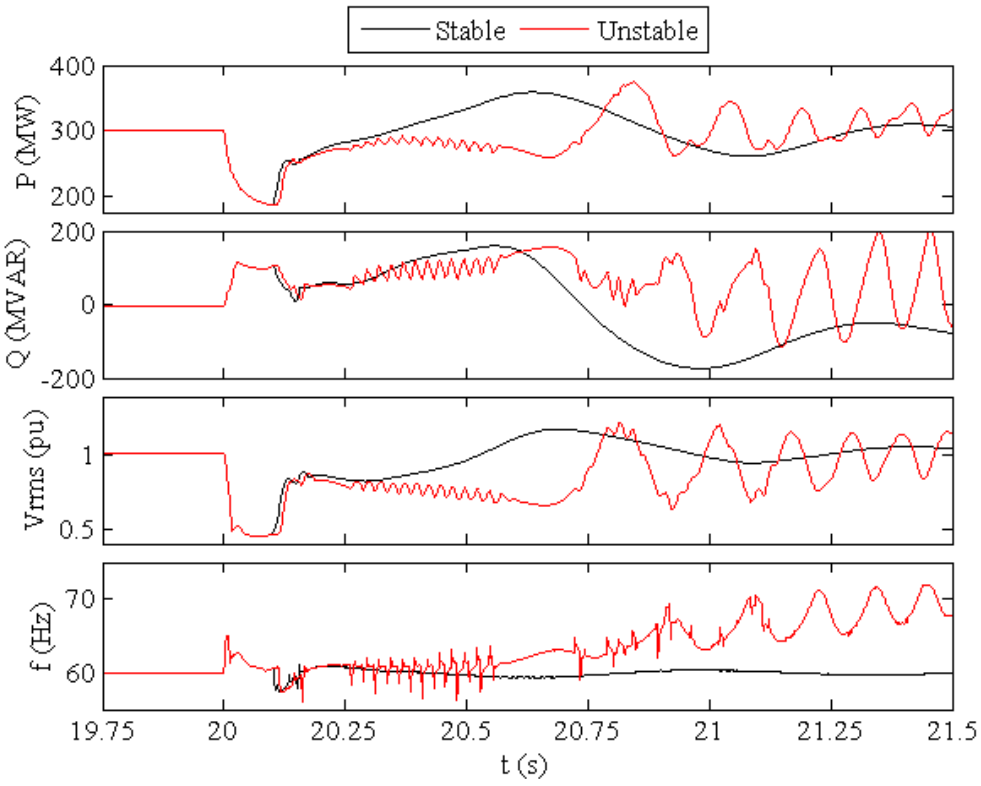

Figure 4.12: Wind farm P, Q, Vrms and f at the terminal for stable and unstable scenarios: Case 1

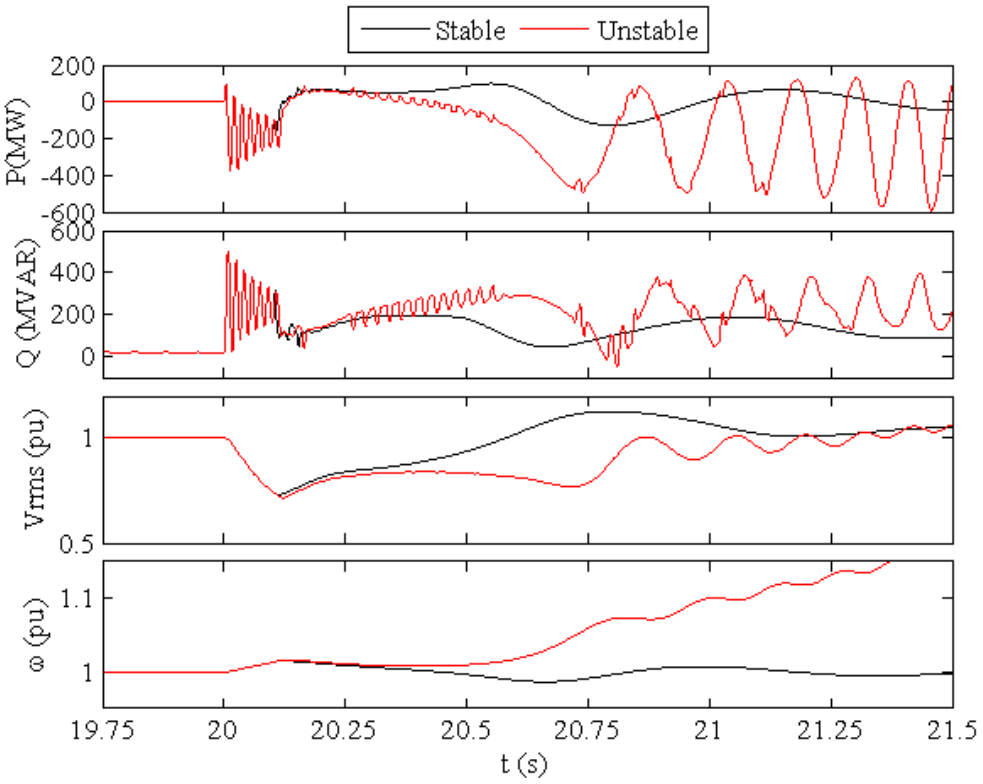

Figure 4.13: Synchronous condenser P, Q, Vrms and ω at the terminal for stable and unstable scenarios: Case 1

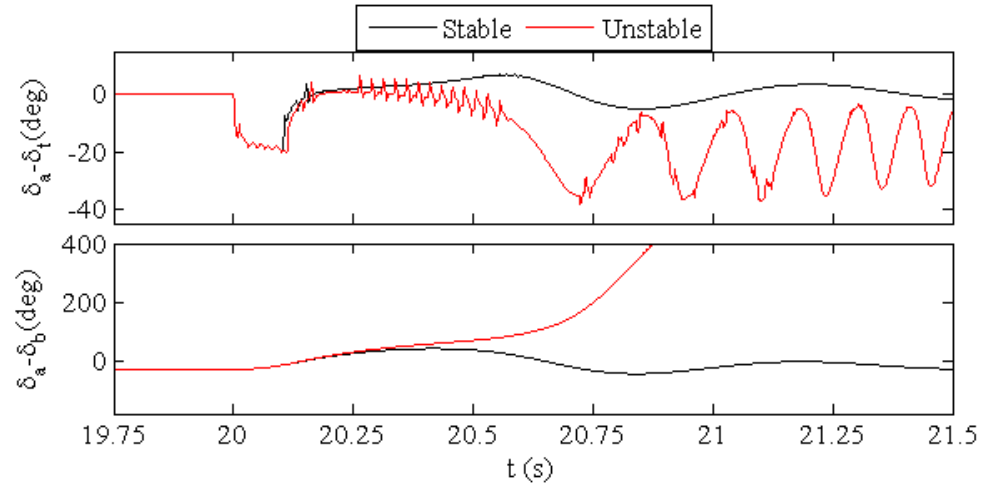

Figure 4.14: Synchronous condenser power angle and internal voltage angle with respect to infinite bus for stable and unstable scenarios: Case 1

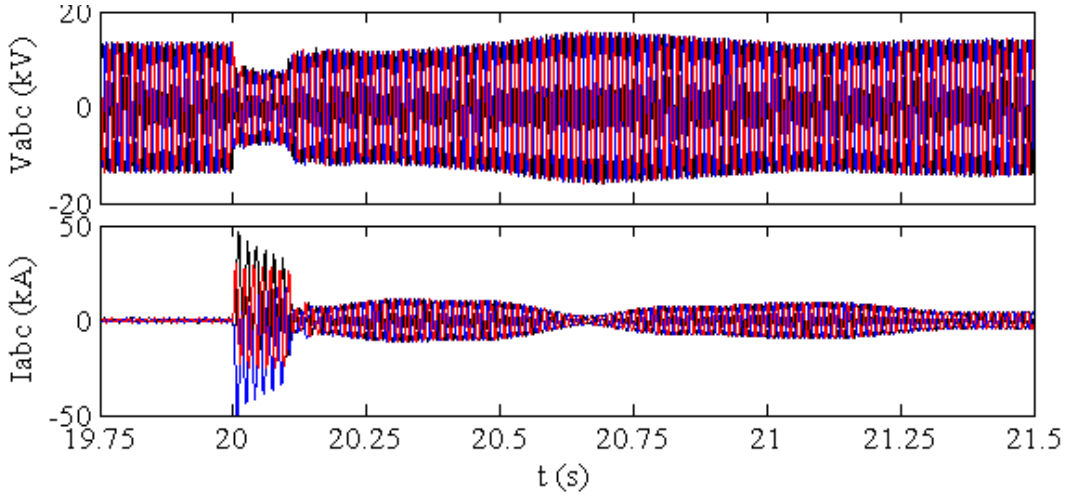

Figure 4.15: Phase voltages and currents at the synchronous condenser terminal for the stable scenario: Case 1

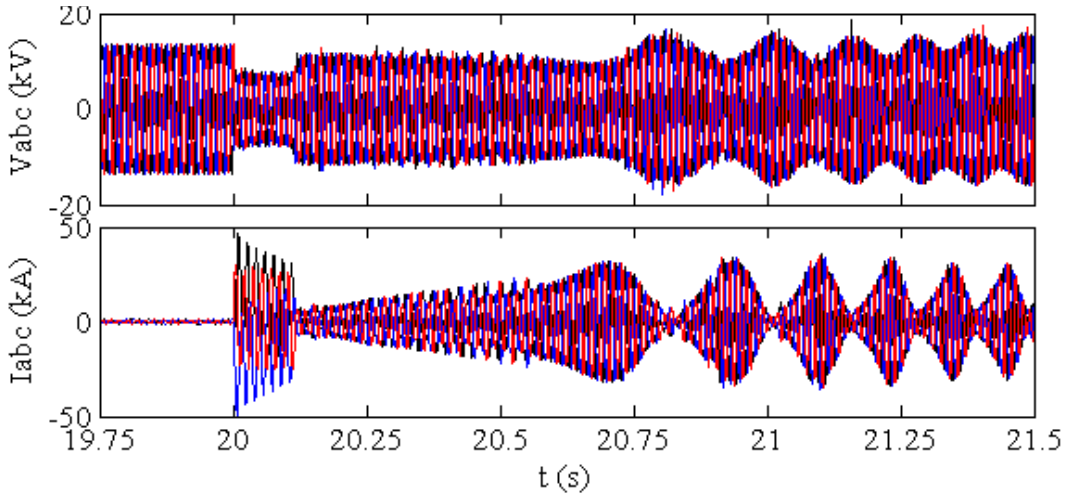

Figure 4.16: Phase voltages and currents at the synchronous condenser terminal for the unstable scenario: Case 1

4.6.2 Case 2: Loss of Synchronism Due to Rotor Deceleration

Lack of active power due to tripping of a large generator or connecting a large load may cause loss of synchronism conditions due to rotor deceleration. In this case,

the load connected at bus 2 is moved to bus 4 to make the impact on the synchronous condenser strong prior to the fault. Then a three phase bolted fault is applied on the bus 6 end of the transformer $TR46$ (location B in Figure 4.11) and the transformer is disconnected after 6 cycles to clear the fault. This disconnect the wind farm from the network creating a loss of 300 MW of generation. The rating of the load (now connected at bus 4) is adjusted to 300 MW and 400 MW to create stable and unstable power swings.

As shown in Figure 4.17, the power deficit due to generation loss is compensated by the synchronous condenser and the system equivalent generator connected at bus 1. synchronous condenser decelerated due to this transient active power output and ultimately lost its synchronism with the system.

As shown in Figure 4.18, similar to Case 1, the power angle does not exceed 180° even though the internal voltage angle with respect to infinite bus exceed −600°. This further demonstrates the possibility of loss of synchronism condition in the system without the synchronous condenser going through pole slipping due to deceleration. Instantaneous voltages and currents of the stable and unstable scenarios are depicted in Figure 4.19 and 4.20, respectively.

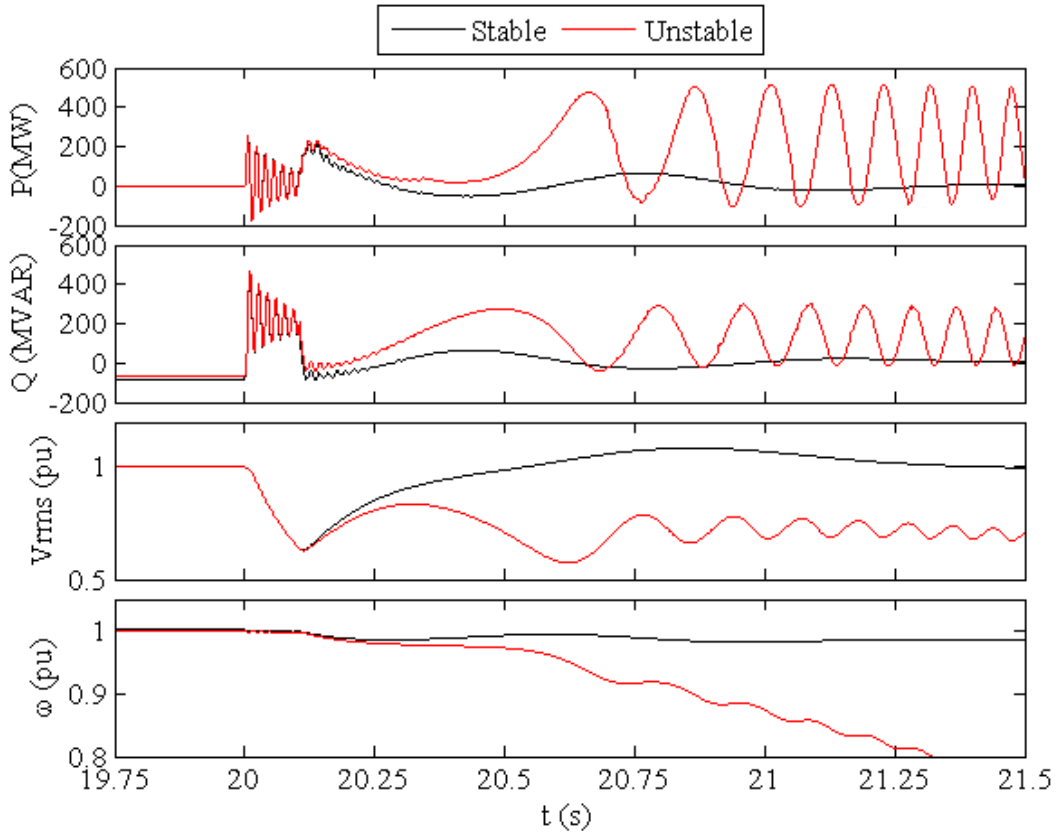

Figure 4.17: Synchronous condenser P, Q, Vrms and ω at the terminal for stable and unstable scenarios: Case 2

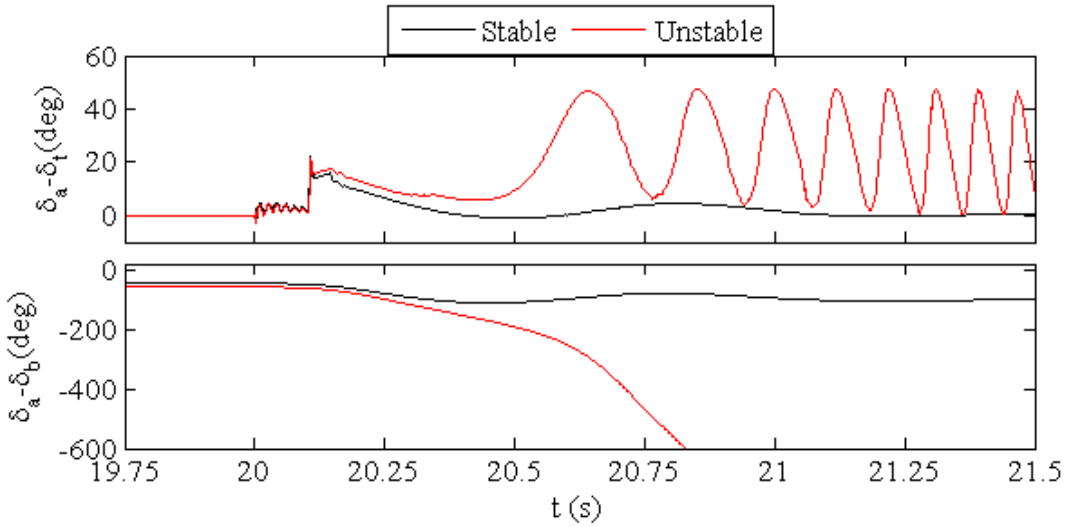

Figure 4.18: Synchronous condenser power angle and internal voltage angle with respect to infinite bus for stable and unstable scenarios: Case 2

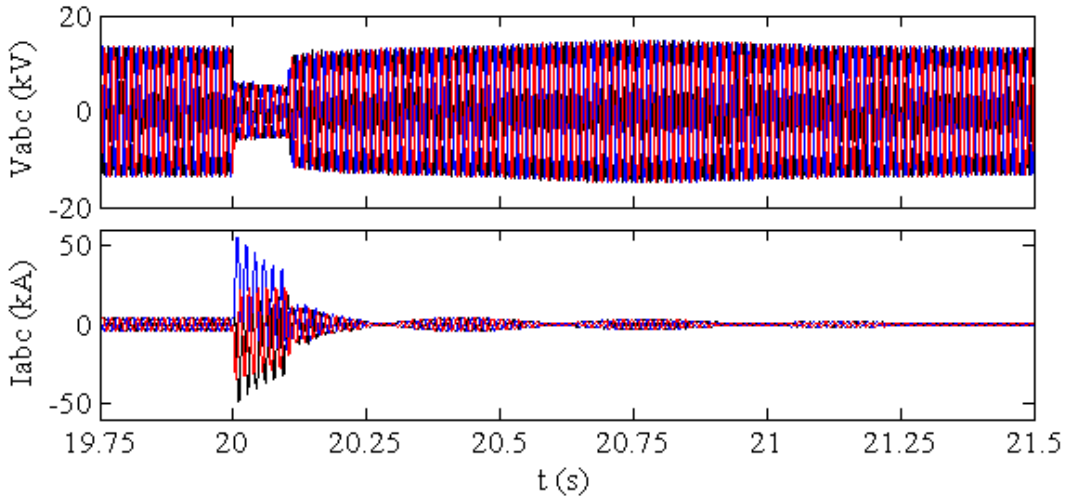

Figure 4.19: Phase voltages and currents at the synchronous condenser terminal for the unstable scenario: Case 2

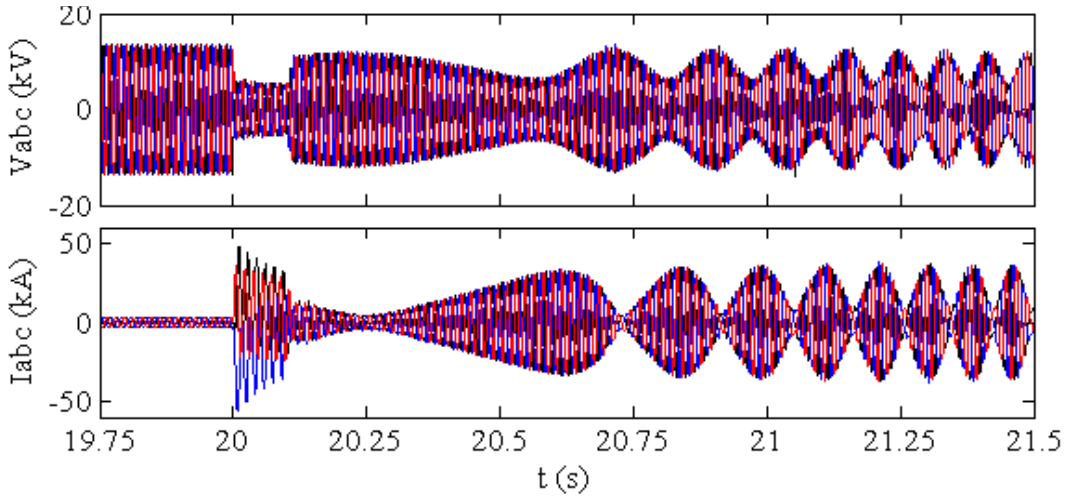

Figure 4.20: Phase voltages and currents at the synchronous condenser terminal for the unstable scenario: Case 2

4.6.3 Case 3: Loss of Excitation Condition

In this case, the field winding of the synchronous condenser was short circuited to test the security of the proposed method against loss of field condition. As shown in Figure 4.21, when the field voltage drops to zero, the field current gradually reduces and ultimately reach zero. As shown in the same figure, the speed of the machine

is not significantly affected due to loss of filed condition. It was observed that, the speed fluctuations did not even reach the threshold speed limit where the proposed method activates at.

As shown in Figure 4.22, the loss of field condition results in a current reversals before the field current reach zero. In other words, the impedance trajectory cross the resistance axis one time. This is clearly visible in Figure 4.22 where vertical markers are aligned with the maximum of phase A voltage in two different time instances across the reversal point (or resistance axis in the impedance plain). The current maximum of same phase is leading the voltage at the left marker and lagging the voltage at the right marker.

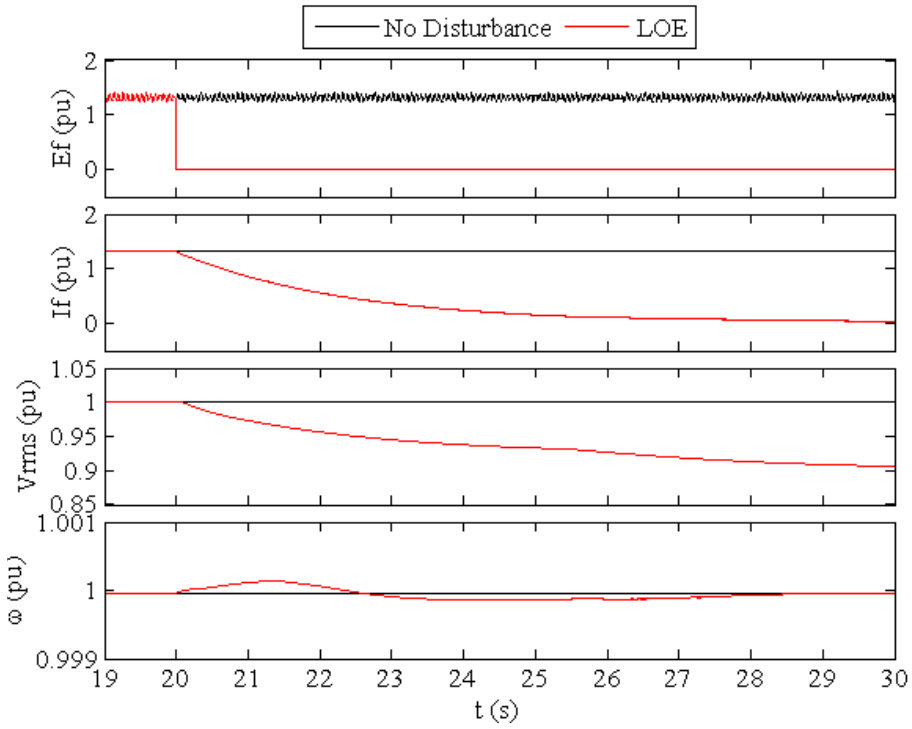

Figure 4.21: Synchronous condenser excitation voltage (Ef), excitation current (If), terminal voltage (Vrms) and speed (ω) at the terminal for LOE and flat run(no disturbance) scenarios : Case 3

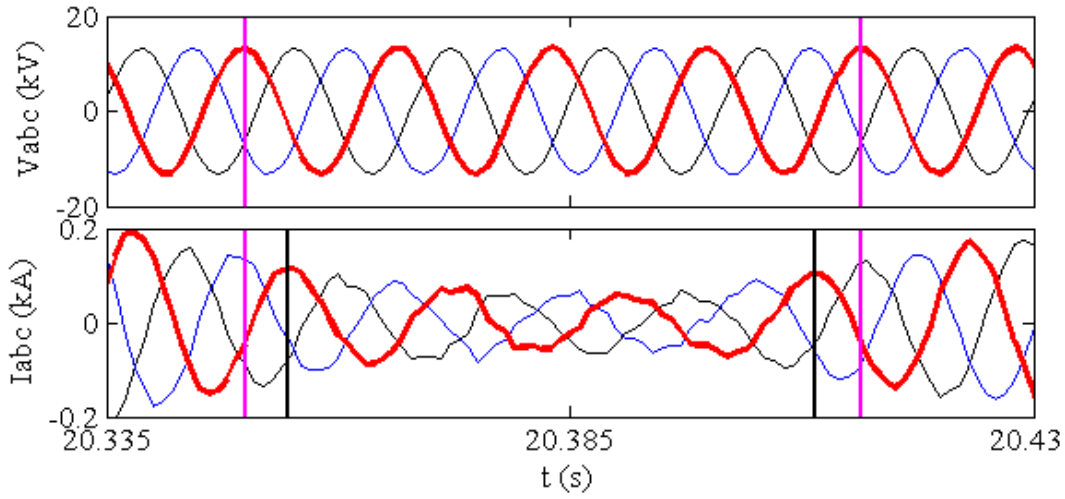

Figure 4.22: Phase voltages and currents at the synchronous condenser terminal following the loss of field. Reversal of current can be seen from the angle of current with respect to voltage: Case 3

4.6.4 Comparison of Loss of Synchronism Detection Methods

Accuracy, security and the loss of synchronism detection speed of the proposed method was compared against single blinder, notch filter, field AC current and loss of excitation schemes. All methods were implemented in PSCAD/EMTDC as described in section 4.5.1. The scenarios presented in Sections 4.6.1, 4.6.2, and 4.6.3 were also used for comparison tests. Results are illustrated in Figures 4.23 through 4.34.

As outlined in section 4.6.1 and 4.6.2, synchronous condenser loss of synchronism condition typically occurs without pole slipping. This is because the stator magnetic field of the synchronous condenser tightly coupled with the terminal voltage due to absence of a prime mover or a load. This is evident in the single blinder scheme depicted in Figure 4.23 and 4.24, where the impedance trajectory did not intersect

either the both blinders or the Mho circle and aligned with the theoretical analysis derived from phasor diagrams in section 4.2. This observation is further substantiated by the fact that the power angle did not exceed 180° during the unstable power swing as illustrated in Figure 4.14 and 4.18. In summary, the single blinder scheme did not operate for unstable power swings, which is the expected response from this method as the swing center is outside the synchronous condenser.

Compared to the notch filter scheme, the proposed method has operated faster. This is because it has issued the trip signal at the first or second swing cycle while the notch filter have issued the trip signals after 3.5 swing cycles. Notch filter is configured to trigger after 7 current direction changes (i.e. 3.5 swing cycles) to discriminate against stable power swings. This is essential in the notch filter scheme since few triggers (current direction changes) can be risen for faults and stable power swings (see Figure 4.25 and 4.26).

Figures 4.27 and 4.28 show the filed current and its AC RMS component used to detect loss of synchronism conditions in the field AC overcurrent scheme. Since any disturbance induces AC components on the field current, it is essential to configure the relay with an adequate current setting and a time delay for proper discrimination against faults and stable power swings. Therefore, this relay is relatively slow in issuing trip signals compared to other traditional methods.

The loss of excitation scheme presented in Figure 4.31 operated as expected for the LOE event (case 3 in section 4.6.3). It also did not issue any trip signals for loss of synchronism conditions during other scenarios. Therefore, LOE scheme may not be used as back up protection for loss of synchronism conditions in synchronous

condensers similar to synchronous generators.

Figures 4.29 and 4.30 show the estimated relative speed trajectories used by the proposed method to detect a loss of synchronism condition. The algorithm detected the loss of synchronism condition at the second maximum/minimum of the unstable ω vs t trajectory at around 20.9s. The rate of change of speed ($\dot{\omega}$ = ROCOF) which were used to identify the maximums in the proposed method along with the trip signal are also depicted in the same figure.

As shown in Figure 4.32 and 4.33, proposed method delivered the fastest tripping for unstable power swings. It also showed the security against faults and LOE conditions (see Figure 4.34).

Single Blinder Scheme Results

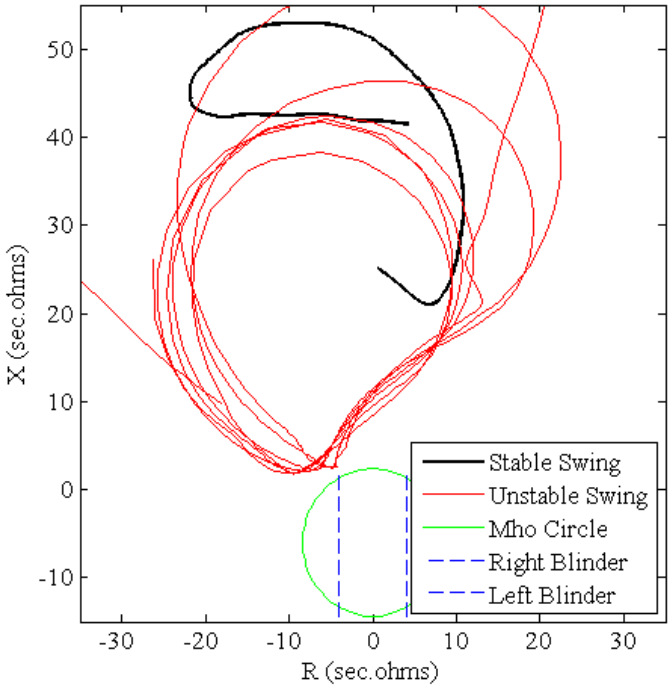

Figure 4.23: Impedance trajectories and settings of the single blinder scheme for stable and unstable scenarios: Case 1

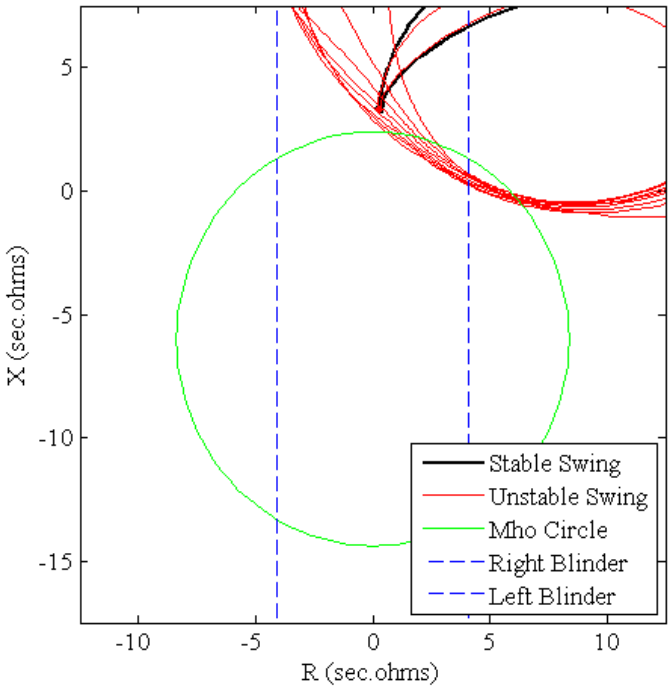

Figure 4.24: Impedance trajectories and settings of the single blinder scheme for stable and unstable scenarios: Case 2

Notching Relay Scheme Results

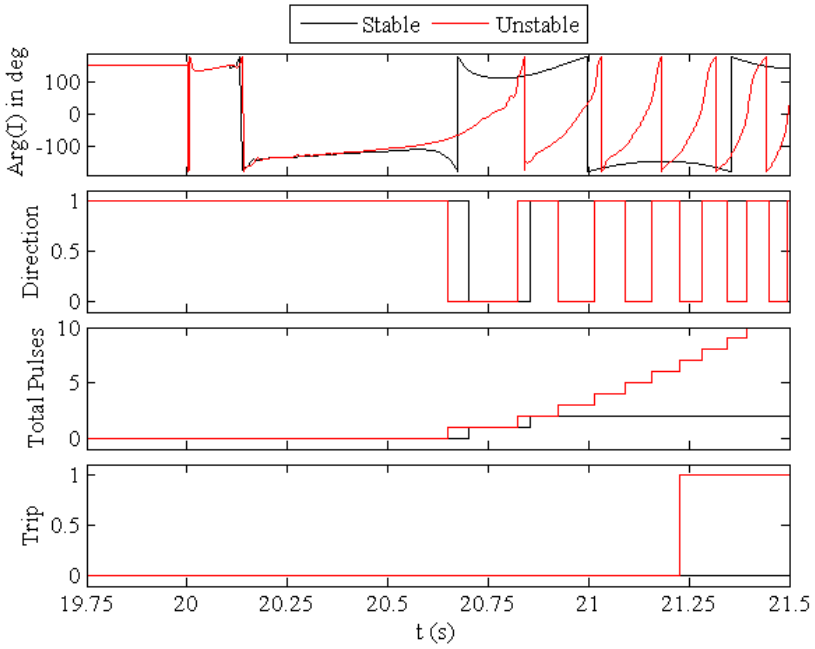

Figure 4.25: Angle of the terminal current, directional element output, cumulative current reversals and trip signal of the notching relay scheme for stable and unstable scenarios: Case 1

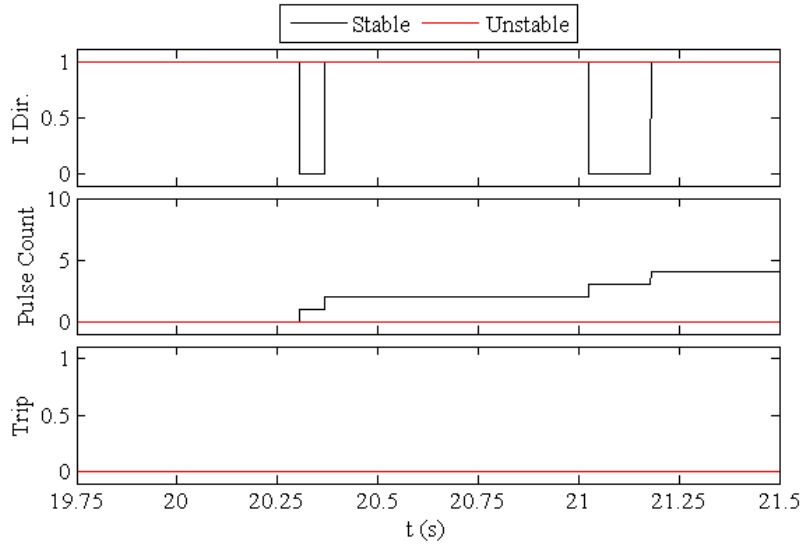

Figure 4.26: Angle of the terminal current, directional element output, cumulative current reversals and trip signal of the notching relay scheme for stable and unstable scenarios: Case 2

Field AC Scheme Results

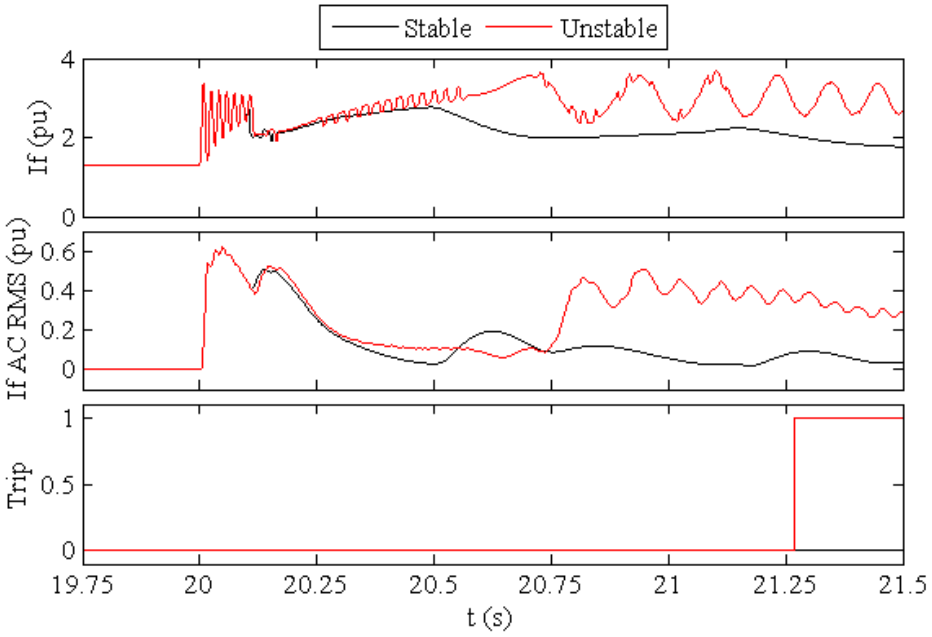

Figure 4.27: Field current, AC RMS component of the field current and trip signal of the Field AC scheme for stable and unstable scenarios: Case 1

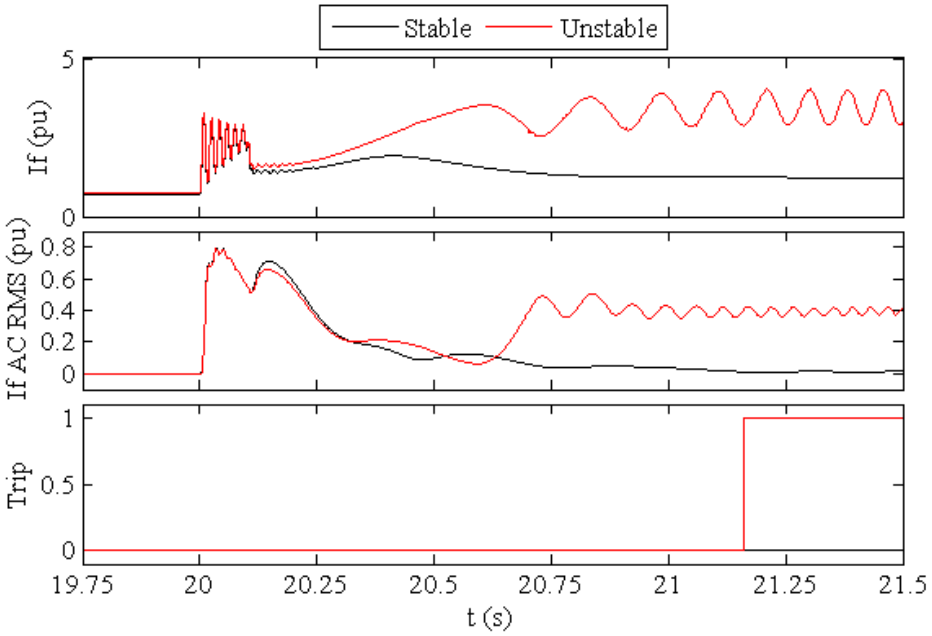

Figure 4.28: Field current, AC RMS component of the field current and trip signal of the Field AC scheme for stable and unstable scenarios: Case 2

Proposed Scheme Results

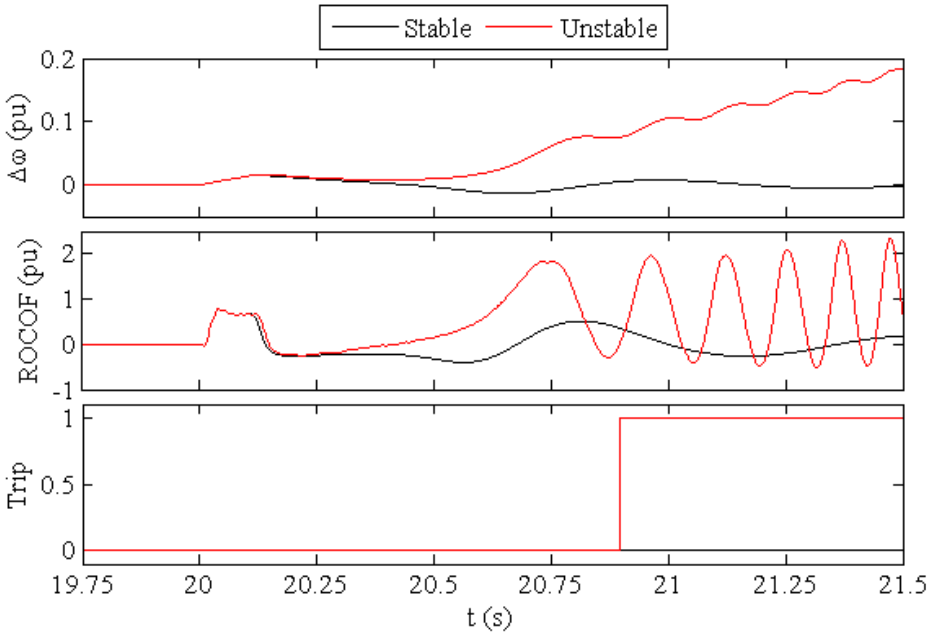

Figure 4.29: ω vs t trajectories used by the proposed method for stable and unstable scenarios: Case 1

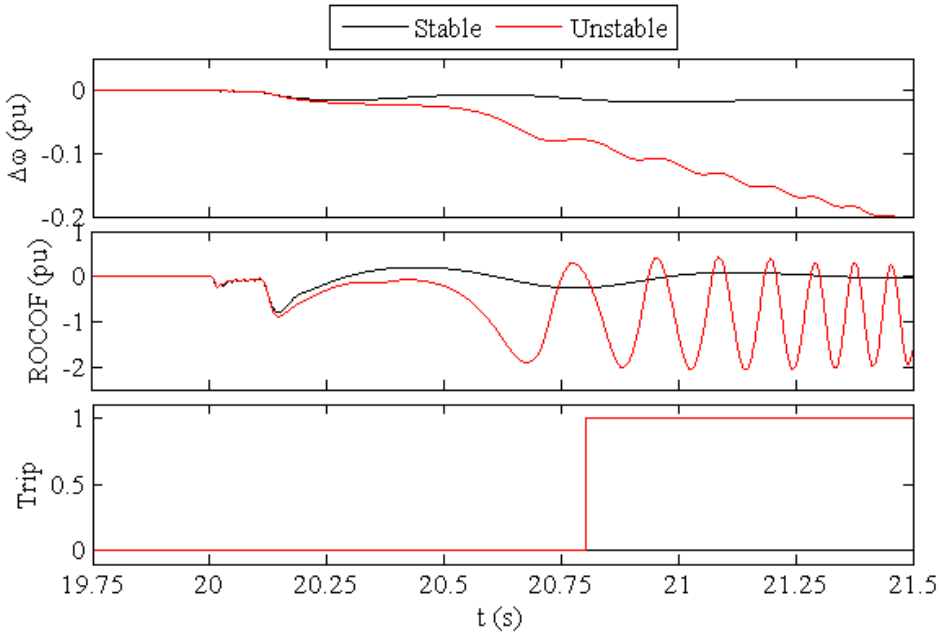

Figure 4.30: ω vs t trajectories used by the proposed method for stable and unstable scenarios: Case 2

LOE Scheme Results

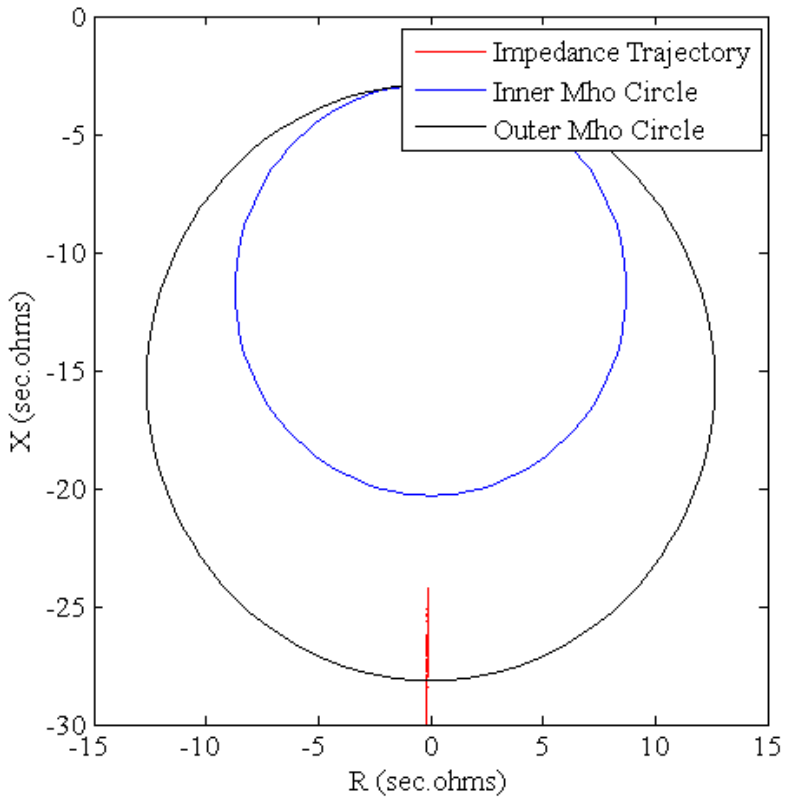

Figure 4.31: Impedance trajectories of the loss of excitation scheme for LOE scenario: Case 3

Trip Signal Results

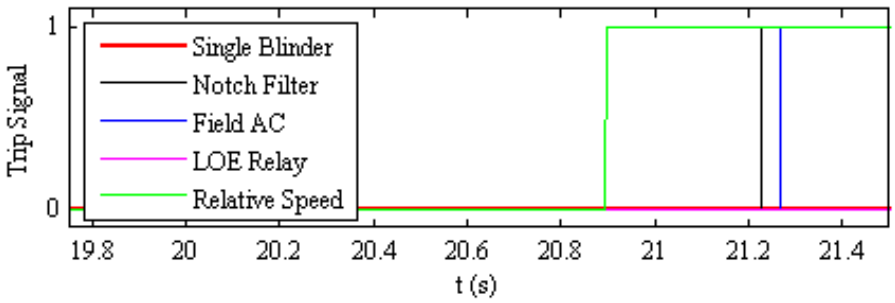

Figure 4.32: Trip signals of single blinder, notch filter, Field AC, LOE relay and proposed loss of synchronism schemes for the unstable power swing: Case 1

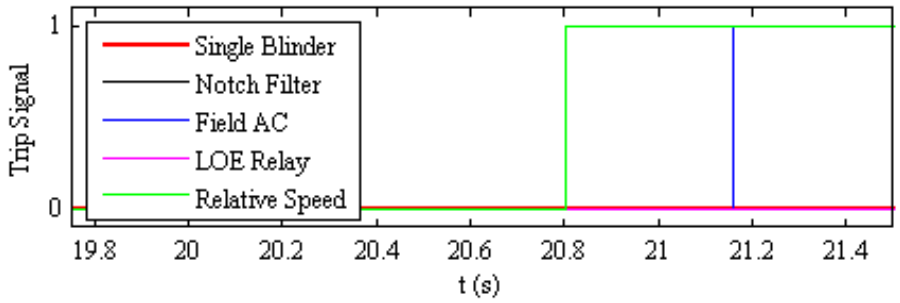

Figure 4.33: Trip signals of single blinder, notch filter, Field AC, LOE relay and proposed loss of synchronism schemes for the unstable power swing: Case 2

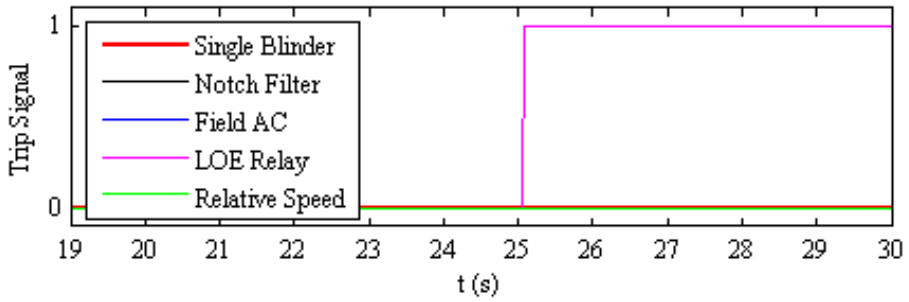

Figure 4.34: Trip signals of single blinder, notch filter, Field AC, LOE relay and proposed loss of synchronism schemes for the unstable power swing: Case 3

4.7 Concluding Remarks

Synchronous generators have been extensively analyzed for their loss of synchronism behavior, resulting in a well-documented framework for predicting and mitigating such events. However, synchronous condensers, despite their increased usage in modern power systems, have not received the same level of scrutiny. The literature indicates a considerable gap in understanding the loss of synchronism phenomenon in synchronous condensers, particularly under conditions where IBRs dominate the power grid.

Therefore, in depth analysis of the loss of synchronism phenomenon in synchronous condensers in the systems with IBRs, providing a theoretical explanation through the use of phasor diagrams is conducted. The study found that the loss of synchronism condition in synchronous condensers generally occurs without pole slipping. This is attributed to the strong coupling between the stator magnetic field and terminal voltage, as there is no prime mover or load involved. The impedance trajectories observed in the time-domain simulations were consistent with the theoretical analysis derived from phasor diagrams. Thus, conventional impedance-based loss of synchronism schemes that rely on the occurrence of pole slipping may be ineffective for protecting synchronous condensers during loss of synchronism conditions.

In addition, the behaviour of the synchronous condenser during system transients was validated using the calculated dynamic impedance. Further, the proposed relative speed based loss of synchronism detection method, originally developed for synchronous generators, is applied to synchronous condensers. Unlike traditional methods, this method does not rely on network-specific settings. Time-domain simulations were conducted to compare this method with several well-established traditional schemes. The results showed improved detection times and demonstrated the method's reliability and security.

Chapter 5

Loss of Synchronism Protection in Weak Grids with High Penetration of Inverter Based Resources

5.1 Introduction

Loss of synchronism protection in weak grids with high penetration of inverter based resources (IBRs) poses distinct challenges, primarily due to reduced short-circuit strength, distorted voltage/current waveforms, and the complex dynamic interactions between IBRs and conventional generation sources. In such weak grid conditions, the ability of synchronous generators to maintain rotor angle stability following disturbances is also affected. Traditional loss of synchronism protection methods, which typically depend on predictable impedance trajectories or rotor angle divergence, may fail to operate reliably in these complex systems.

To evaluate the performance of the proposed relative speed based method under weak grid conditions, comprehensive simulation studies were carried out on several weak systems with varying levels of IBR penetration and system disturbances. The studies utilized a modified version of the IEEE 39 bus system and focused on the impacts arising from the integration of Type-3 and Type-4 wind turbine generators (WTGs). The study encompasses the loss of synchronism behaviour for both synchronous generators and synchronous condensers.

The remainder of this chapter is organized as follows. Section 5.2 discusses the influence of IBR integration on the impedance characteristics of power swings. Section 5.3 outlines the development of the modified IEEE 39 bus system to mimic different levels of IBR penetration. The selection of study scenarios to analyse loss of synchronism of synchronous generators and synchronous condensers in weak grids is discussed in Section 5.4. Section 5.5 presents the case study findings, evaluating the influence of IBRs on loss of synchronism and the performance of the proposed loss of synchronism protection method. Finally, Section 5.6 summarizes the key conclusions drawn from the study.

5.2 Impact of IBR Integration on the Impedance Characteristics of Power Swings

The post fault response of IBRs demonstrates different transient and dynamic behaviors compared to conventional synchronous generators, posing significant challenges to traditional protection schemes. Distance relays, for instance, may erro-

neously interpret power swing conditions as faults, resulting in undesired tripping of transmission lines [57, 58]. In the context of loss of synchronism protection for generators, the altered voltage and current phasors during swing conditions can cause the apparent impedance trajectory to enter the relay's operating zone, potentially triggering unintended disconnection of stable machines [59]. Such misoperations threaten overall system stability and can propagate cascading failures and widespread blackouts [60].

The dynamic behavior of IBRs particularly their fault and immediate post fault response is dictated primarily by the converter control strategies and differs substantially from that of synchronous generators [61–63]. Consequently, the integration of IBRs has been shown to affect several conventional protection functions, including power swing blocking (PSB), out-of-step tripping (OOST), directional elements, and negative-sequence-based protection [64–69]. As noted in [70, 71], the performance of legacy PSB and OOST schemes may degrade under high IBR penetration due to the reduction in system inertia. Loss of synchronism protection schemes, typically rely on monitoring the rate of change of apparent impedance to differentiate between faults and unstable swing conditions [72–74]. The rate of change of impedance is inherently tied to the system's rotor angle dynamics, which are directly influenced by the aggregate system inertia. This decline in inertia accelerates system frequency dynamics and impedance trajectory variations, making it increasingly difficult to distinguish between fault-induced transients and genuine power swings. Since conventional PSB schemes are designed based on the maximum rate of impedance change under full synchronous generator penetration, their reliability deteriorates under faster swing

conditions induced by IBRs. This impairs the relay's ability to distinguish faults from stable swings. Under such conditions, traditional PSB settings tuned for synchronous generator dominated systems may no longer provide secure and dependable performance.

Moreover, with high levels of IBR integration, the trajectory of the apparent impedance during power swings can shift significantly, compromising the detection accuracy of OOST schemes [75]. OOST functions rely on identifying critical points along the impedance trajectory beyond which system recovery is no longer feasible. These thresholds are typically defined based on synchronous generator dominated impedance trajectories. With significant IBR penetration, the altered trajectory may no longer intersect the preset detection zones, leading to either missed tripping or false operation. Therefore, with increasing IBR integration, a reassessment and re-parametrization of PSB and OOST settings are imperative to ensure continued protection reliability.

The work presented in [76, 77] and derived a dynamic model of power swings for systems incorporating IBRs, which was subsequently employed in to examine the practical implications for power swing protection. Although this work provides a comprehensive investigation with detailed modelling, it relies on complex system representations and therefore cannot be readily adopted in practice.

5.3 Test System Development

The case study utilizes a modified version of the IEEE 39 bus test system as the network model. A single-line diagram of the system is presented in Figure 5.1. Detailed network data, generator parameters, and the corresponding load-flow solution are provided in Appendix A.3. The system was initially developed in PSS/E and subsequently translated into PSCAD/EMTDC using the E-Tran conversion tool, enabling initialization of both synchronous generators and IBRs based on the load-flow solution. In PSCAD/EMTDC, all transmission lines were modeled using travelling wave-based Bergeron models, while loads (both active and reactive) were represented as constant impedance elements.

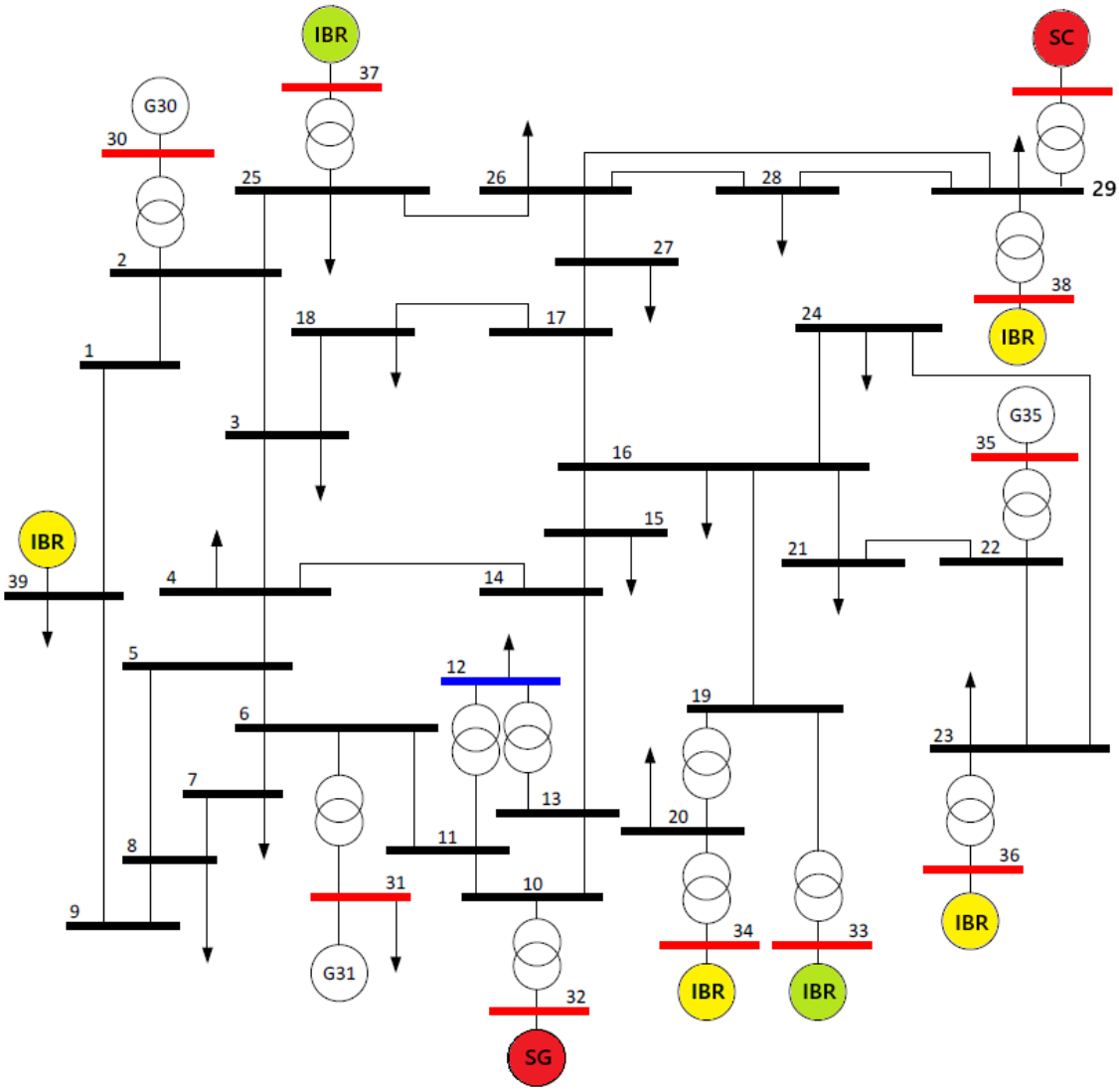

Figure 5.1: Modified IEEE 39 bus test system [2]. Coloured in yellow: synchronous machines that are replaced with IBRs under stage 1. Coloured in green: additional synchronous machines that are replaced with IBRs under stage 2. Coloured in red: SG and SC under study

To replicate weak and extremely weak grid environments, the test network was configured with two IBR penetration levels, referred to as Stage 1 and Stage 2.

5.3.1 Stage 1 IBR Integration

To mimic a relatively weak system, four generators out of nine generators in the original IEEE 39 bus test system is replaced with Type 3 (generators at bus 34 and 39) and Type 4 (generators at bus 36 and 38) WTG models. In addition, the impedance of the voltage source representing the network equivalent at bus 31 is modified to have a reactance of 0.1 pu and a resistance of 0.01 pu on the machine MVA base (i.e. SCR = 10 and X/R = 10) to achieve the adequate network strength. The resultant Short Circuit Ratios (SCRs) at the Point of Interconnection (POI) of wind plants following above modification are tabulated in Table 5.1.

Table 5.1: SCRs at each WF POI of the modified IEEE 39 bus test system with stage 1 IBR integration

POI (Gen.) Bus No.	**SCMVA**	**Rated MW**	**SCR**	**X/R**
20 (34)	2746	1000	2.75	3.33
23 (36)	3821	1000	3.82	4.34
29 (38)	1626	1000	1.63	2.45
39 (39)	2216	1000	2.22	1.68

As demonstrated above, the SCR values at the POIs for all four wind plants are below 4, accompanied by relatively low X/R ratios. These findings collectively verify the weak system characteristics of the modified IEEE 39 bus test system, making it a suitable candidate for evaluating the performance of the proposed method under weak grid conditions.

5.3.2 Stage 2 IBR Integration

To emulate extremely weak grid conditions, two additional synchronous generators in the modified system described in Section 5.3.1 were replaced with IBRs. As a result, six out of the nine generators in the original IEEE 39 bus test system were substituted with WTG models—Type 3 WTGs (at buses 33, 34, and 39) and Type 4 WTGs (at buses 36, 37, and 38). The corresponding SCRs at the POIs for the wind plants after this modification are presented in Table 5.2.

Table 5.2: SCRs at each WF POI of the modified IEEE 39 bus test system with stage 2 IBR integration

POI (Gen.) Bus No.	**SCMVA**	**Rated MW**	**SCR**	**X/R**
20 (34)	1718	1000	1.72	2.09
23 (36)	3139	1000	3.14	3.22
29 (38)	1365	1000	1.37	2.08
39 (39)	1970	1000	1.97	1.56
25 (37)	3715	1000	3.72	2.72
19 (33)	2271	1000	2.27	2.15

As demonstrated above, the SCR and X/R values at the POIs further reduced compared to stage 1 due to replacement of two additional synchronous machines with IBRs. These findings collectively verify the extremely weak system characteristics of the modified IEEE 39 bus test system, making it a suitable candidate for evaluating the performance of the proposed method under extreme weak grid conditions.

5.4 Study Scenarios

The investigation focused on two sets of scenarios aimed at analyzing loss of synchronism behaviour of synchronous generators and condensers in weak grids. Multiple fault scenarios were simulated with different load flow conditions and IBR penetration levels using modified IEEE 39 bus test system. This includes;

- System faults (large disturbances) - 24 scenarios
- Tripping without faults (small disturbances)- 1 scenario
- Loadflow conditions - 2 scenarios
- IBR penetration levels - 2 scenarios
- Device under study (SG or SC) - 2 scenarios

Therefore, in total two hundred (200 = (24+1) x 2 x 2 x 2) scenarios were simulated. Further details of study scenarios are provided in Sections 5.4.1 and 5.4.2.

5.4.1 Synchronous Generator Study Scenarios

A total of one hundred (100) unique scenarios—including 96 fault cases and 4 non-fault disturbances were simulated to assess the sensitivity and security of the proposed loss of synchronism protection method for synchronous generators under weak grid conditions. The simulations encompassed three fault types (LG, 2LG, and 3LG), four fault locations (each end of the transmission lines connecting bus 10–11 and bus 6–11), and two fault durations (50 ms and 150 ms). The synchronous generator located at bus 32 was selected for detailed analysis. The performance of the

proposed protection scheme was evaluated based on its loss of synchronism detection accuracy and detection speed. A summary of the results, along with traces from few selected scenarios, is presented in Section 5.5.

5.4.2 Synchronous Condenser Study Scenarios

An additional set of one hundred (100) unique scenarios—comprising 96 faults and 4 non-fault disturbances was simulated to evaluate the proposed method's effectiveness in detecting loss of synchronism conditions in synchronous condensers under weak grid conditions. A synchronous condenser was introduced at bus 29 and designated as the device under study. The considered faults include LG, 2LG, and 3LG types at four locations: the bus 26 end of all lines connected to bus 26 (i.e., lines 25–26, 27–26, 28–26, and 29–26), with fault durations of 50 ms and 150 ms. Additionally, loads at buses 28 and 29 were moved to bus 26 to facilitate realistic loss of synchronism scenarios under practical fault clearing times. The proposed method's performance was assessed based on detection accuracy and speed. A summary of outcomes and representative traces provided in Section 5.5.

5.5 Results Discussion

An overall summary of the study results and a breakdown by protection scheme and IBR level are presented in Table 5.3 and 5.4, respectively. As shown, the majority of scenarios simulated yielded stable power swings, specifically 172 out of 200 cases. As expected, the proposed relay did not trigger during any of these stable events.

The remaining 28 scenarios experienced unstable power swings, of which 22 were successfully detected, while the remaining 6 were not.

The six failed scenarios are from stage 2 IBR integration level representing extreme weak system. This is due to the fact that the loss of synchronism condition occur faster compared to traditional systems such that the maximums and minimums of the relative rotor speed does not detectable. i.e. only first maximum occur but subsequency minimum or maximums does not occur. Therefore, it missed the zero crossing of the rate of change of relative speed and hence algorithm did not detected the loss of synchronism condition.

This indicates that the proposed method may be influenced by the complexities arising from nearby IBRs in extremely weak systems. However, an overall success rate of 97% highlights its reliability and accuracy in identifying loss of synchronism conditions in grids with high IBR penetration.

Detailed results for each IBR penetration level, as well as those involving synchronous generators and synchronous condensers, are presented in Sections 5.5.1 to 5.5.4.

Table 5.3: Overall results summary

Description	**Number of Scenarios**		
	Unstable Power Swings	**Stable Power Swings**	**Total**
Total Simulated	28	172	200
Detected Correctly	22	172	194
Mis/Delayed Operation	6	0	0
Success Rate	**78.6 %**	**100 %**	**97 %**

Table 5.4: Results breakdown by protection scheme and IBR level

Protection Scheme	**IBR Level**	**Success Rate (%)**
Synchronous Generator LOS	Stage 1	100
	Stage 2	88
Synchronous Condenser LOS	Stage 1	100
	Stage 2	100
Average		**97**

5.5.1 Results Discussion: Synchronous Generator Scenarios with Stage 1 IBR Integration

A summary of the study results is presented in Table 5.5. As shown, the majority of scenarios simulated with stage 1 IBR integration yielded stable power swings, specifically 42 out of 50 cases. As anticipated, the proposed relay did not operate in any of these stable conditions. The remaining eight (8) scenarios exhibited unstable power swings, all of which were associated with 3LG fault events cleared in 150 ms.

Table 5.5: Synchronous generator results summary - IBR penetration stage 1

Description	**Number of Scenarios**		
	Unstable Power Swings	**Stable Power Swings**	**Total**
Total Simulated	8	42	50
Detected Correctly	8	42	50
Mis/Delayed Operation	0	0	0

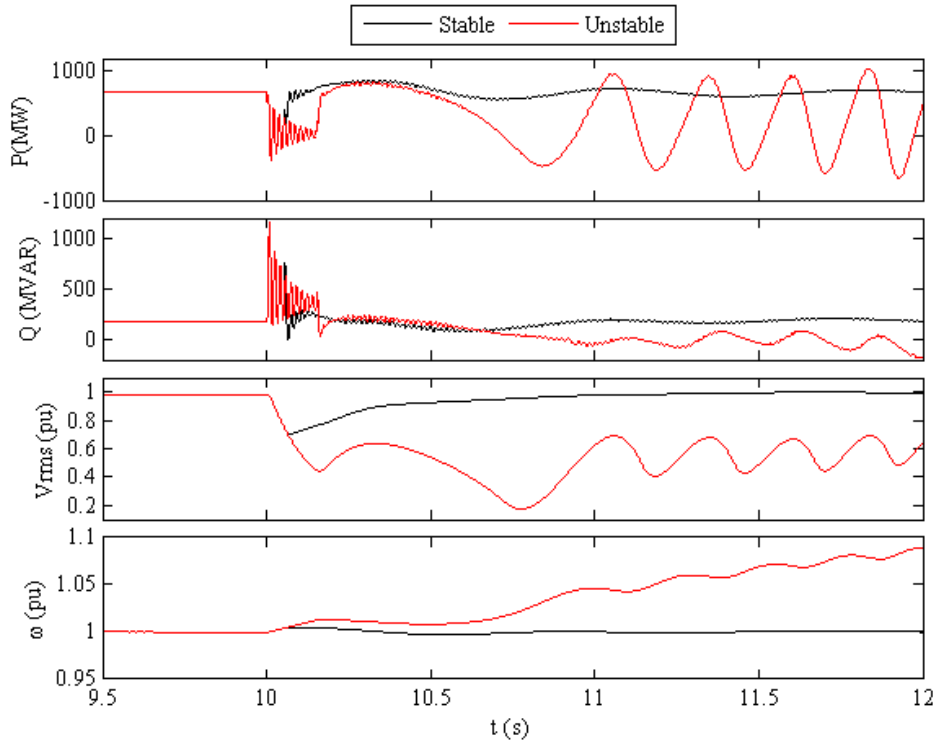

Figure 5.2: P, Q, Vrms and ω at the terminal of the synchronous generator at bus 32 for stable and unstable power swings (S1 and S2)

As illustrated in Figure 5.2, at stage 1 IBR penetration level, the influence of nearby IBRs on the relative speed of the rotor is minimal and does not significantly alter its trajectory from the expected pattern. The proposed algorithm issued the trip signal at the second maximum of the relative speed trajectory in all unstable scenarios. Overall, the proposed algorithm has shown success rate of 100% for system faults under weak grid conditions. Plots of a selected stable scenario (S1) and an unstable scenario (S2) are depicted in Figure 5.2 through 5.6. Those are related to bolted 3LG faults at bus 10 end of the transmission line between bus 10-11 (in Figure A.3) with 50ms and 150ms clearing times.

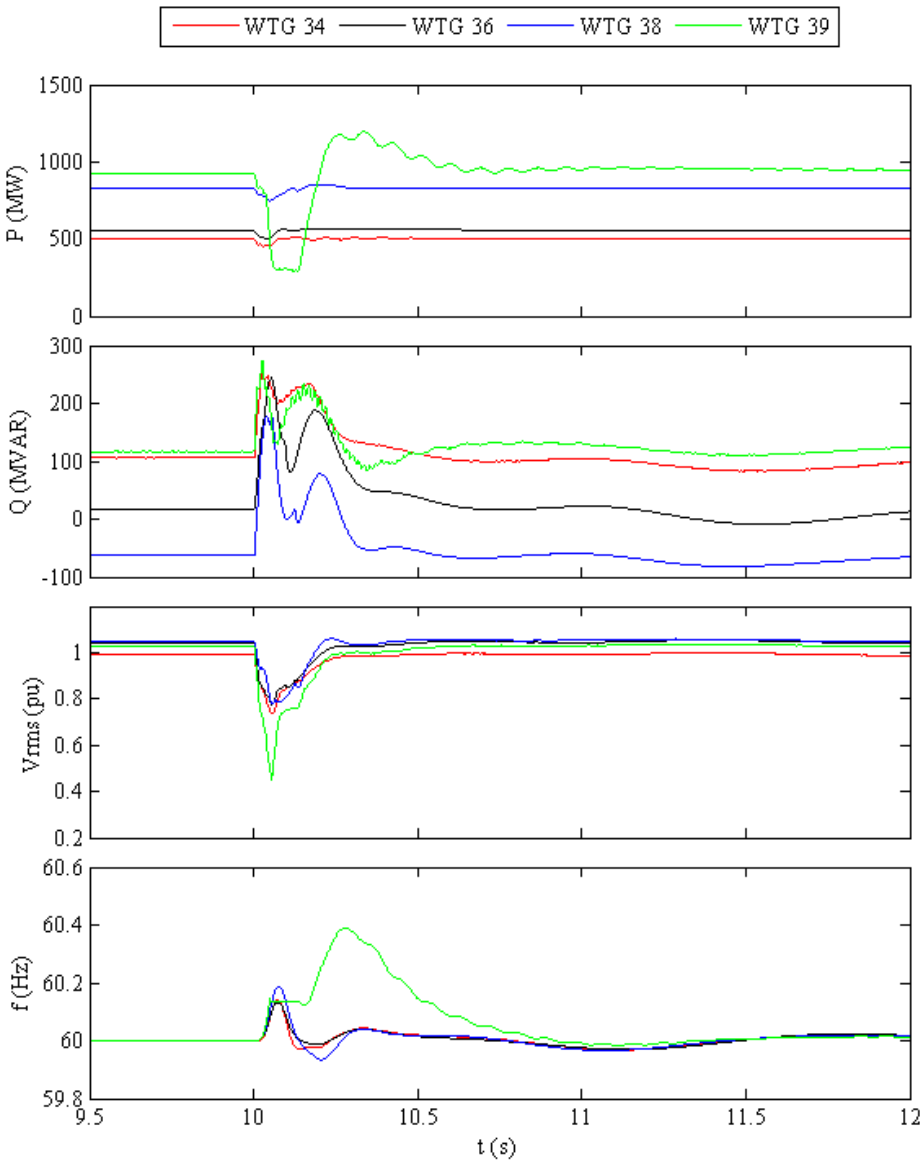

Figure 5.3: P, Q, Vrms at the POI and PLL frequency of the wind plants during a stable power swing (S1)

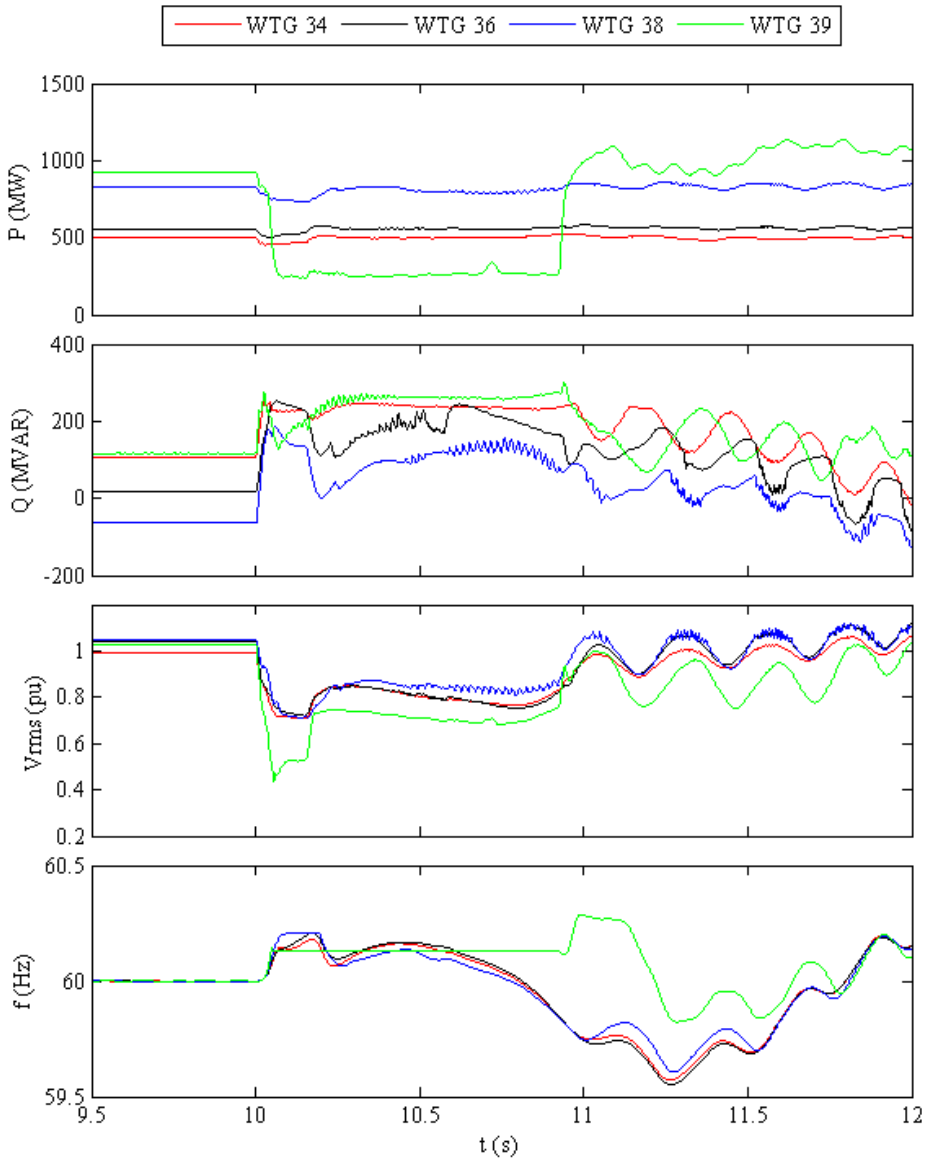

Figure 5.4: P, Q, Vrms at the POI and PLL frequency of the wind plants during an unstable power swing (S2)

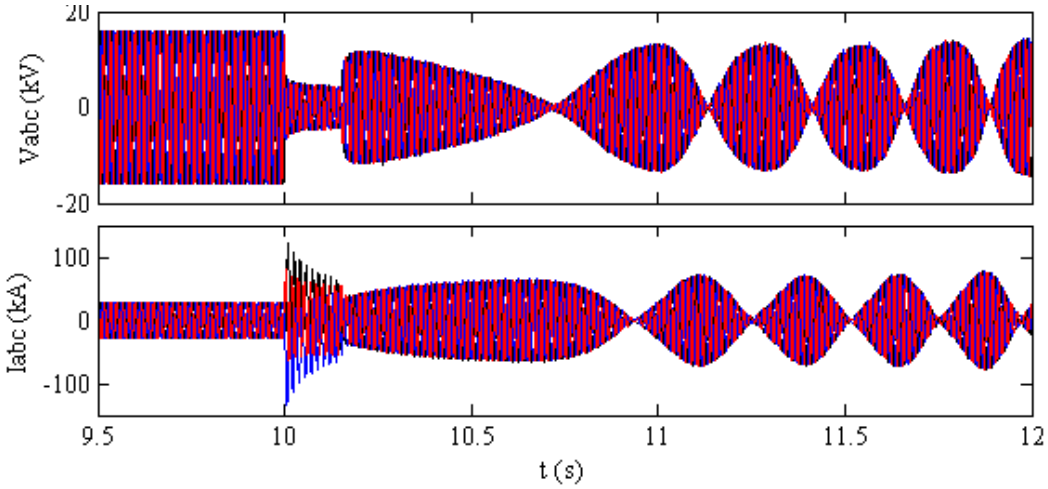

Figure 5.5: Phase voltages and currents of the synchronous generator at bus 32 for the unstable power swing (S2)

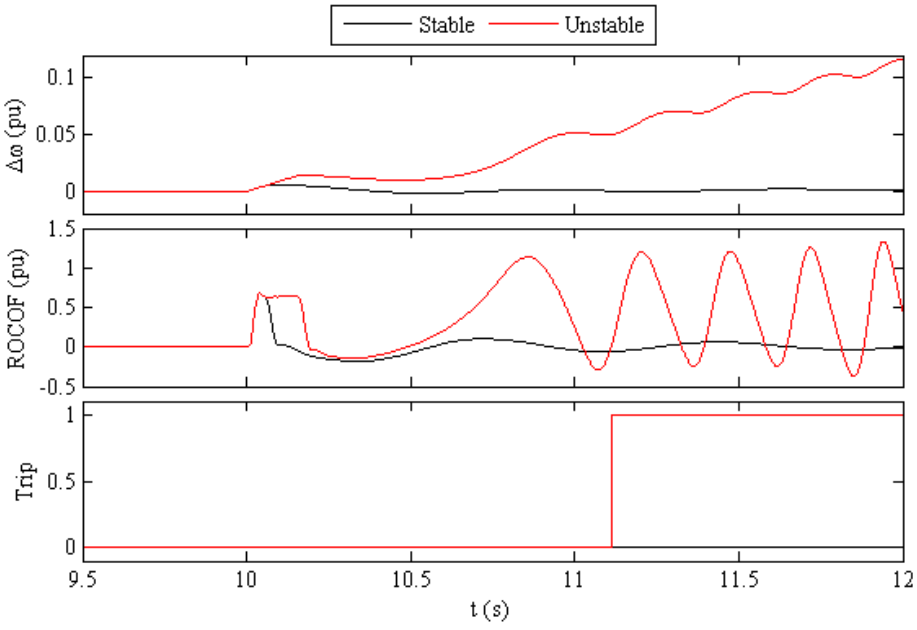

Figure 5.6: ω vs t trajectories used by the proposed method for stable and unstable power swings (S1 and S2)

5.5.2 Results Discussion: Synchronous Generator Scenarios with Stage 2 IBR Integration

A summary of the study results is presented in Table 5.6. As illustrated, the majority of scenarios simulated under stage 2 IBR integration resulted in stable power swings - i.e. 34 out of 50 cases. Consistent with expectations, the proposed relay did not operate for any of these stable events. Conversely, unstable power swings were observed in 16 out of the 50 scenarios. Notably, all 3LG and 2LG fault cases with a 150 ms clearing time led to instability. As stated in Section 5.1, the ability of synchronous generators to preserve rotor angle stability is significantly reduced in weak grids. This observation is further supported by the fact that all 2LG faults with 150 ms clearing time, which caused instability in stage 2, were previously stable under stage 1 IBR penetration levels.

Table 5.6: Synchronous generator results summary - IBR penetration stage 2

Description	**Number of Scenarios**		
	Unstable Power Swings	**Stable Power Swings**	**Total**
Total Simulated	16	34	50
Detected Correctly	10	34	44
Mis/Delayed Operation	6	0	6

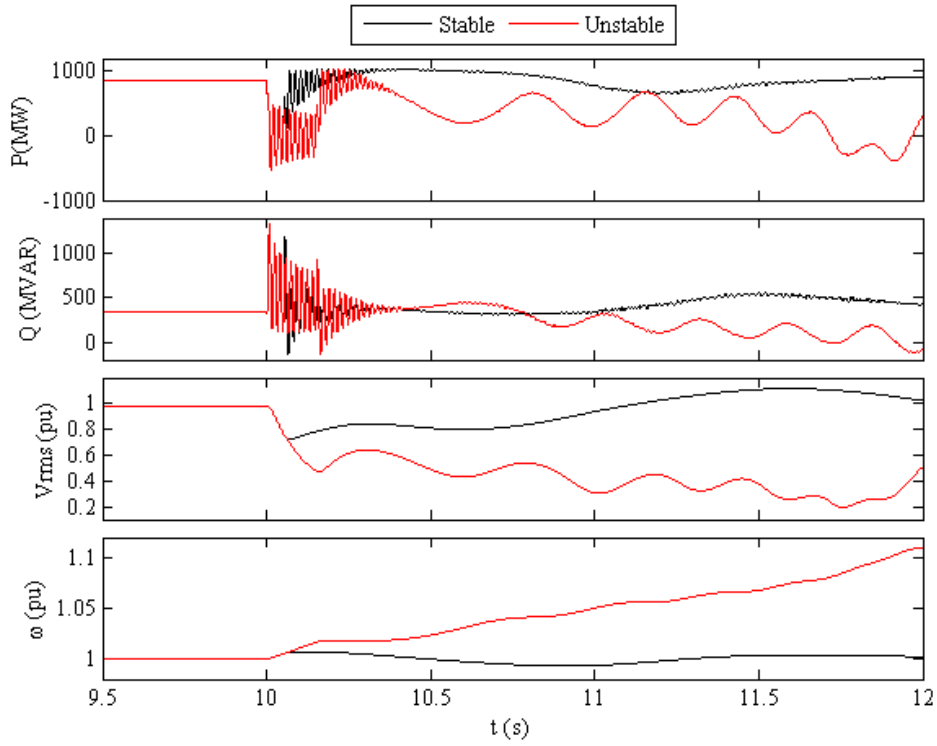

Figure 5.7: P, Q, Vrms and ω at the terminal of the synchronous generator at bus 32 for stable and unstable power swings (S3 and S4)

The proposed algorithm issued the trip signal at the first maximum of the relative speed in majority of unstable scenarios. Out of 16 unstable scenarios, proposed algorithm failed in 6 scenarios. As illustrated in Figure 5.7, at stage 2 IBR penetration level, the influence of nearby inverter-based resources on the relative speed of the rotor is considerable and altered its trajectory from the expected pattern. This is due to the fact that the system being extremely weak and the loss of synchronism condition occur faster compared to traditional systems such that the maximums and minimums of the relative rotor speed does not detectable. i.e. only first maximum occur but subsequency minimum or maximums does not occur. Therefore, it missed the zero

crossing of the rate of change of relative speed and hence algorithm did not detected the loss of synchronism condition.

Overall, the proposed algorithm has shown success rate of 88% for system faults under weak grid conditions. Plots of a selected stable scenario (S3) and an unstable scenario (S4) are depicted in Figure 5.7 through 5.11. Those are related to bolted 3LG faults at bus 26 end of the transmission line between bus 25-26 (in Figure A.3) with 50ms and 150ms clearing times.

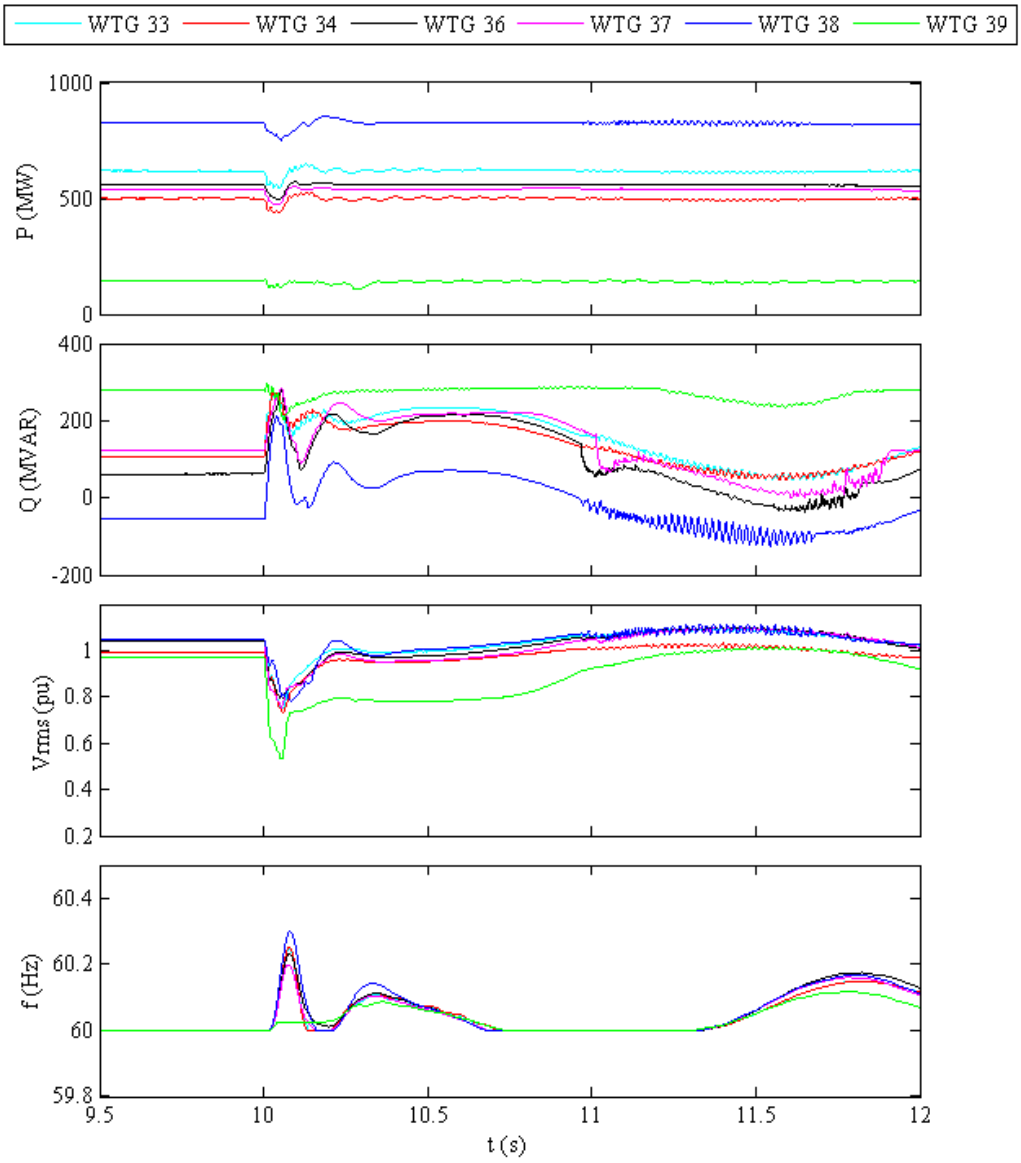

Figure 5.8: P, Q, Vrms at the POI and PLL frequency of the wind plants during a stable power swing (S3)

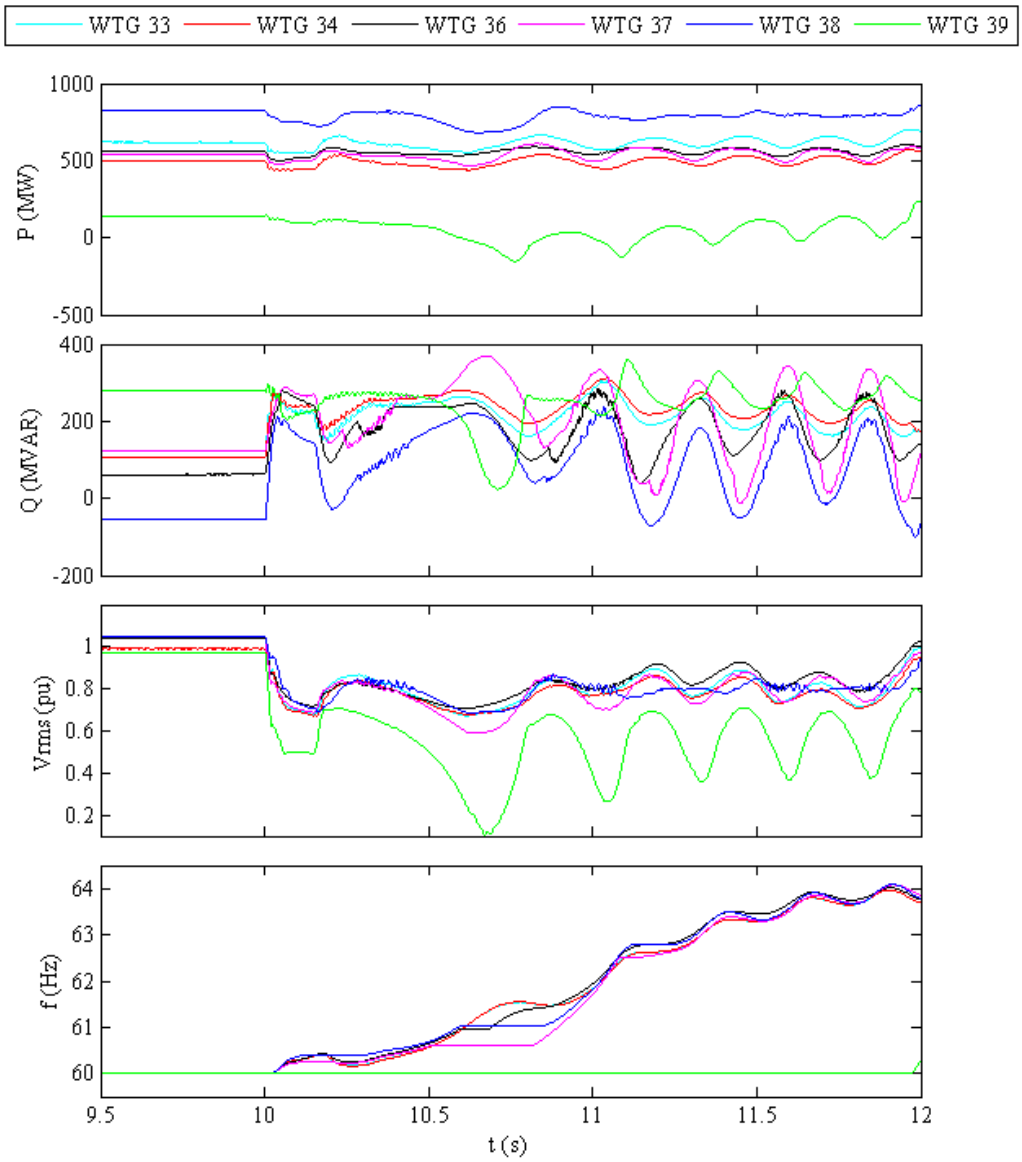

Figure 5.9: P, Q, Vrms at the POI and PLL frequency of the wind plants during an unstable power swing (S4)

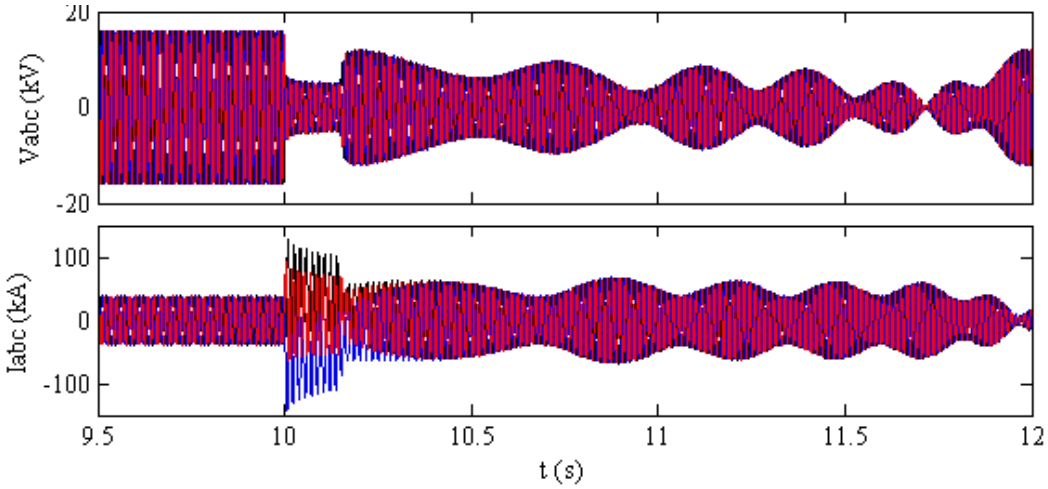

Figure 5.10: Phase voltages and currents of the synchronous generator at bus 32 for the unstable power swing (S4)

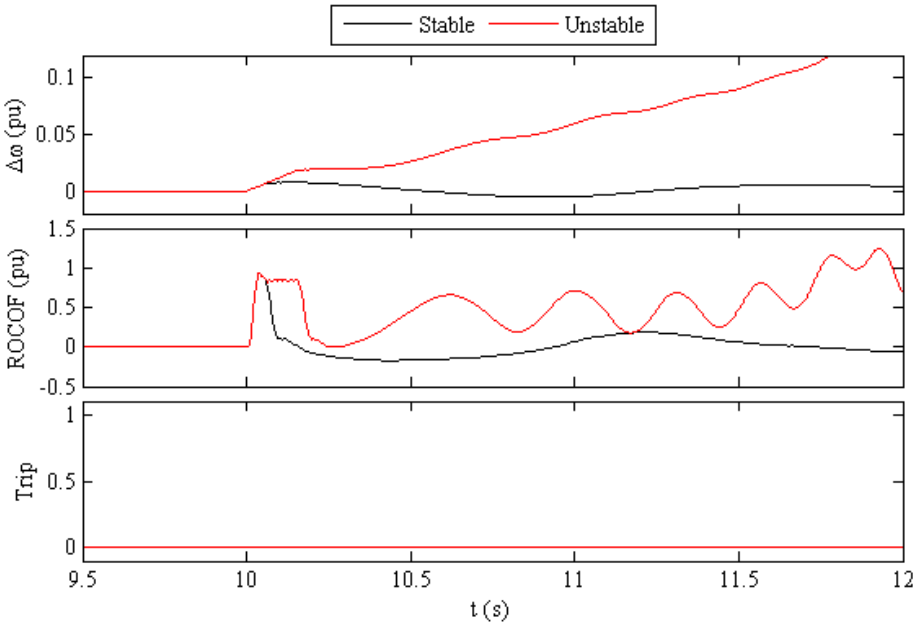

Figure 5.11: ω vs t trajectories used by the proposed method for stable and unstable power swings (S3 and S4)

5.5.3 Results Discussion: Synchronous Condenser Scenarios with Stage 1 IBR Integration

A summary of the study results is presented in Table 5.7. As shown, the majority of scenarios simulated with stage 1 IBR integration yielded stable power swings, specifically 48 out of 50 cases. As anticipated, the proposed relay did not operate in any of these stable conditions. The remaining two (2) scenarios exhibited unstable power swings, both are associated with 3LG fault events cleared in 150 ms.

Table 5.7: Synchronous condenser results summary - IBR penetration stage 1

Description	**Number of Scenarios**		
	Unstable Power Swings	**Stable Power Swings**	**Total**
Total Simulated	2	48	50
Detected Correctly	2	48	50
Mis/Delayed Operation	0	0	0

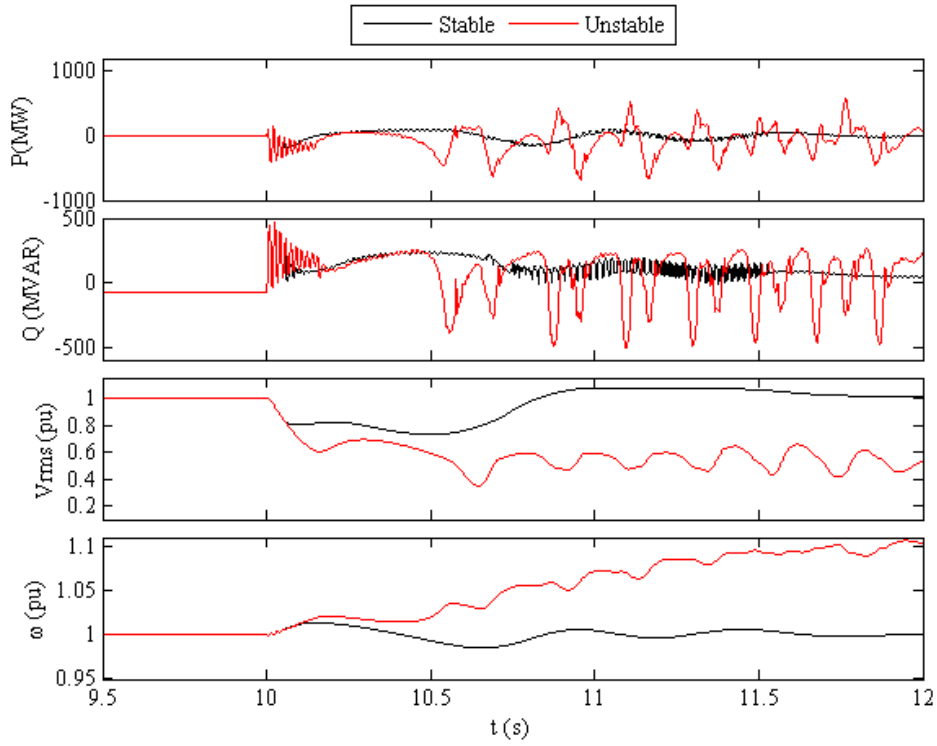

Figure 5.12: P, Q, Vrms and ω at the terminal of the synchronous condenser at bus 29 for stable and unstable power swings (S5 and S6)

As illustrated in Figure 5.12, at stage 1 IBR penetration level, the influence of nearby IBRs on the relative speed of the rotor is minimal and does not significantly alter its trajectory from the expected pattern. The proposed algorithm issued the trip signal at the second maximum of the relative speed trajectory in all unstable scenarios. Overall, the proposed algorithm has shown success rate of 100% for system faults under weak grid conditions. Plots of a selected stable scenario (S5) and an unstable scenario (S6) are depicted in Figure 5.12 through 5.16. Those are related to bolted 3LG faults at bus 26 end of the transmission line between bus 26-28 (in Figure A.3) with 50ms and 150ms clearing times.

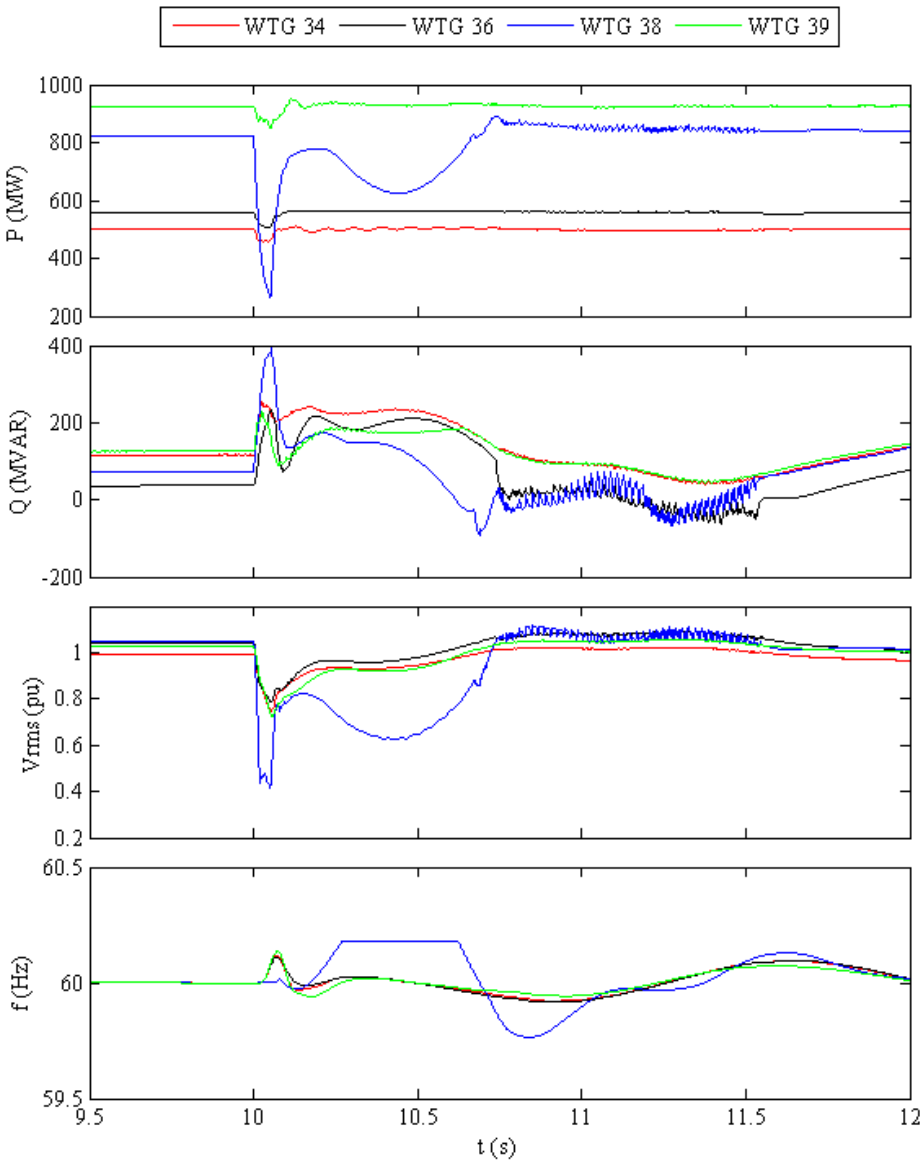

Figure 5.13: P, Q, Vrms at the POI and PLL frequency of the wind plants during a stable power swing (S1)

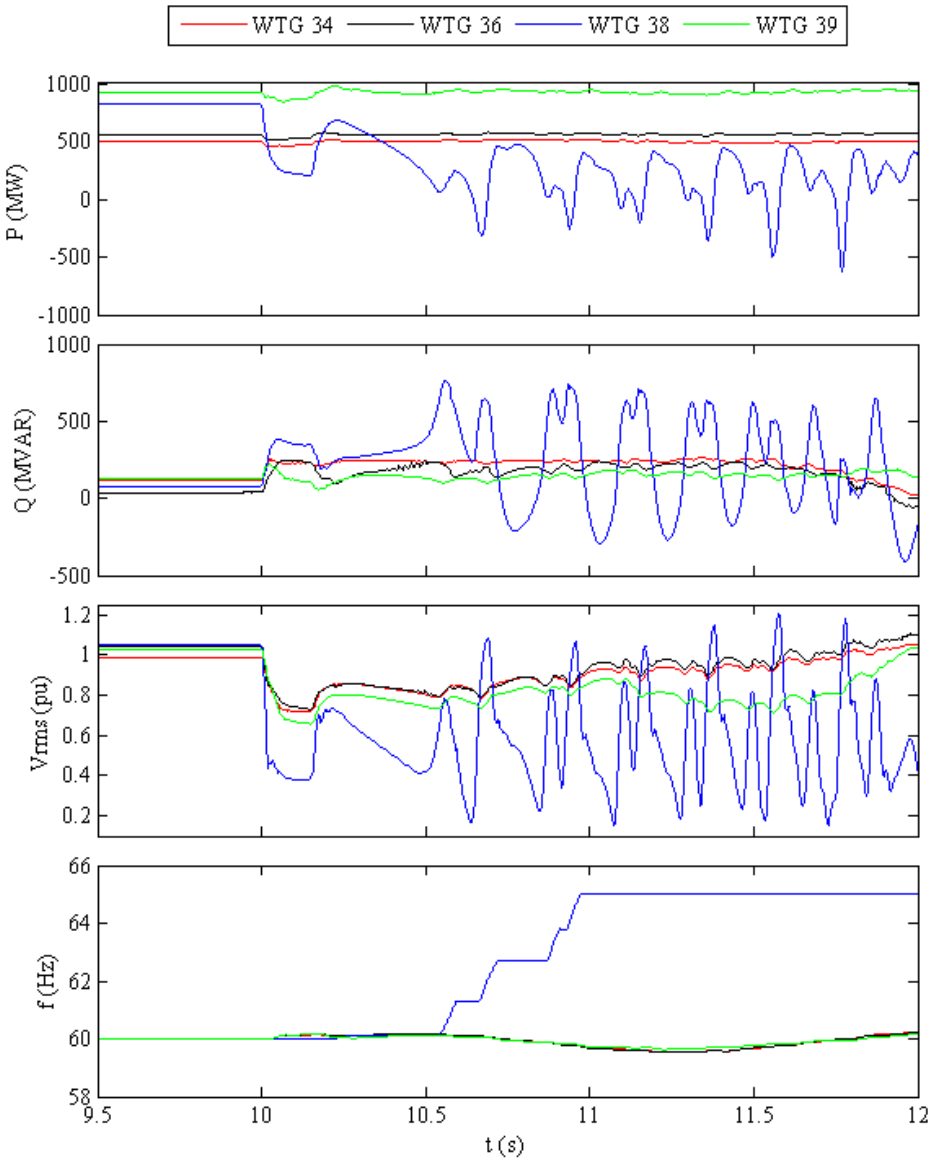

Figure 5.14: P, Q, Vrms at the POI and PLL frequency of the wind plants during an unstable power swing (S2)

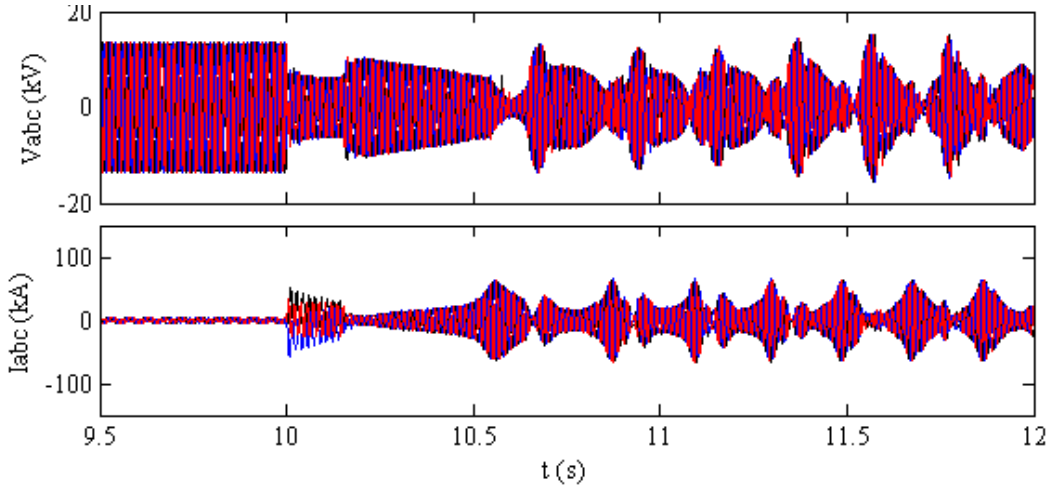

Figure 5.15: Phase voltages and currents of the synchronous generator at bus 32 for the unstable power swing (S2)

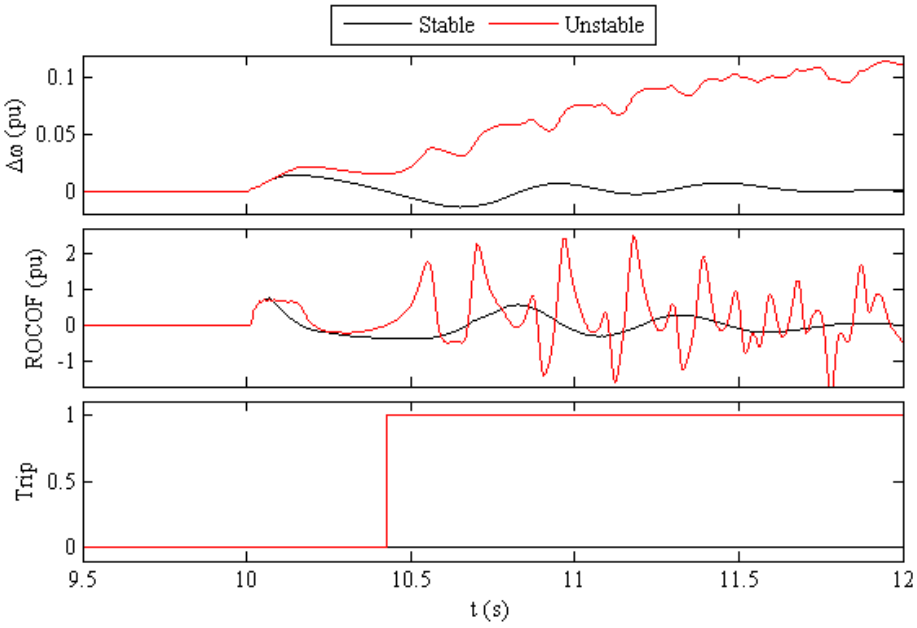

Figure 5.16: ω vs t trajectories used by the proposed method for stable and unstable power swings (S1 and S2)

5.5.4 Results Discussion: Synchronous Condenser Scenarios with Stage 2 IBR Integration

A summary of the study results is presented in Table 5.8. As shown, the majority of scenarios simulated with stage 2 IBR integration yielded stable power swings, specifically 48 out of 50 cases (similar observations as stage 1 results). As anticipated, the proposed relay did not operate in any of these stable conditions. The remaining two (2) scenarios exhibited unstable power swings, both are associated with 3LG fault events cleared in 150 ms.

Table 5.8: Synchronous condenser results summary - IBR penetration stage 2

Description	**Number of Scenarios**		
	Unstable Power Swings	**Stable Power Swings**	**Total**
Total Simulated	2	48	50
Detected Correctly	2	48	50
Mis/Delayed Operation	0	0	0

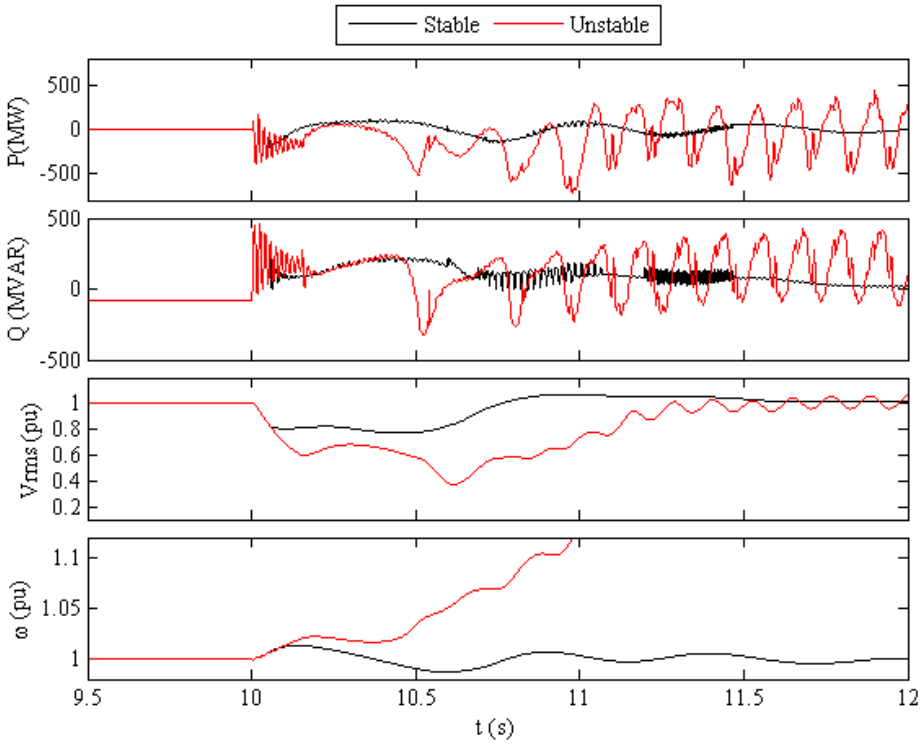

Figure 5.17: P, Q, Vrms and ω at the terminal of the synchronous condenser at bus 29 for stable and unstable power swings (S7 and S8)

As illustrated in Figure 5.17, at stage 2 IBR penetration level, the influence of nearby IBRs on the relative speed of the rotor is minimal and does not significantly alter its trajectory from the expected pattern. The proposed algorithm issued the trip signal at the second maximum of the relative speed trajectory in all unstable scenarios. Overall, the proposed algorithm has shown success rate of 100% for system faults under weak grid conditions. Plots of a selected stable scenario (S7) and an unstable scenario (S8) are depicted in Figure 5.17 through 5.21. Those are related to bolted 3LG faults at bus 26 end of the transmission line between bus 26-28 (in Figure A.3) with 50ms and 150ms clearing times.

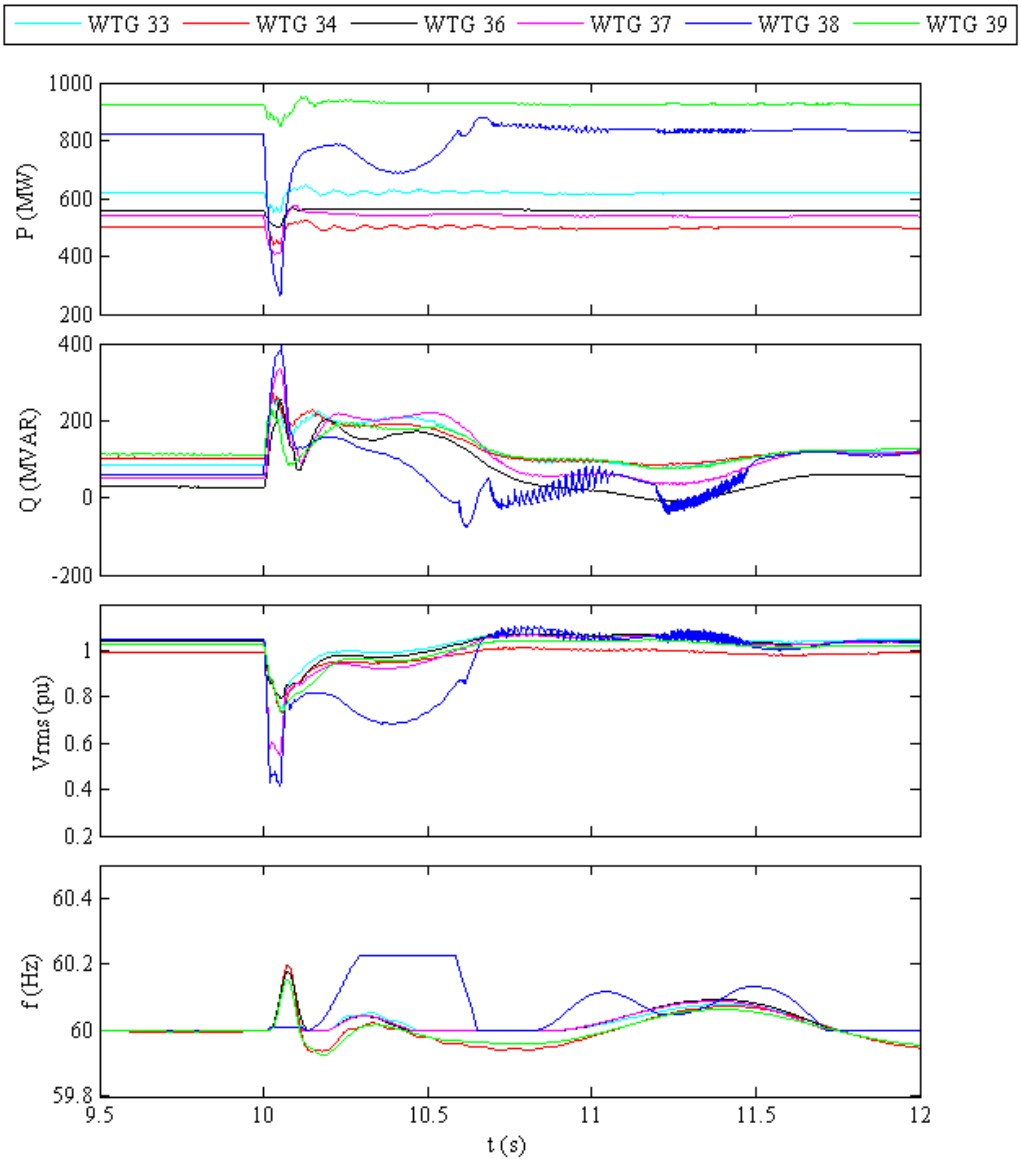

Figure 5.18: P, Q, Vrms at the POI and PLL frequency of the wind plants during a stable power swing (S1)

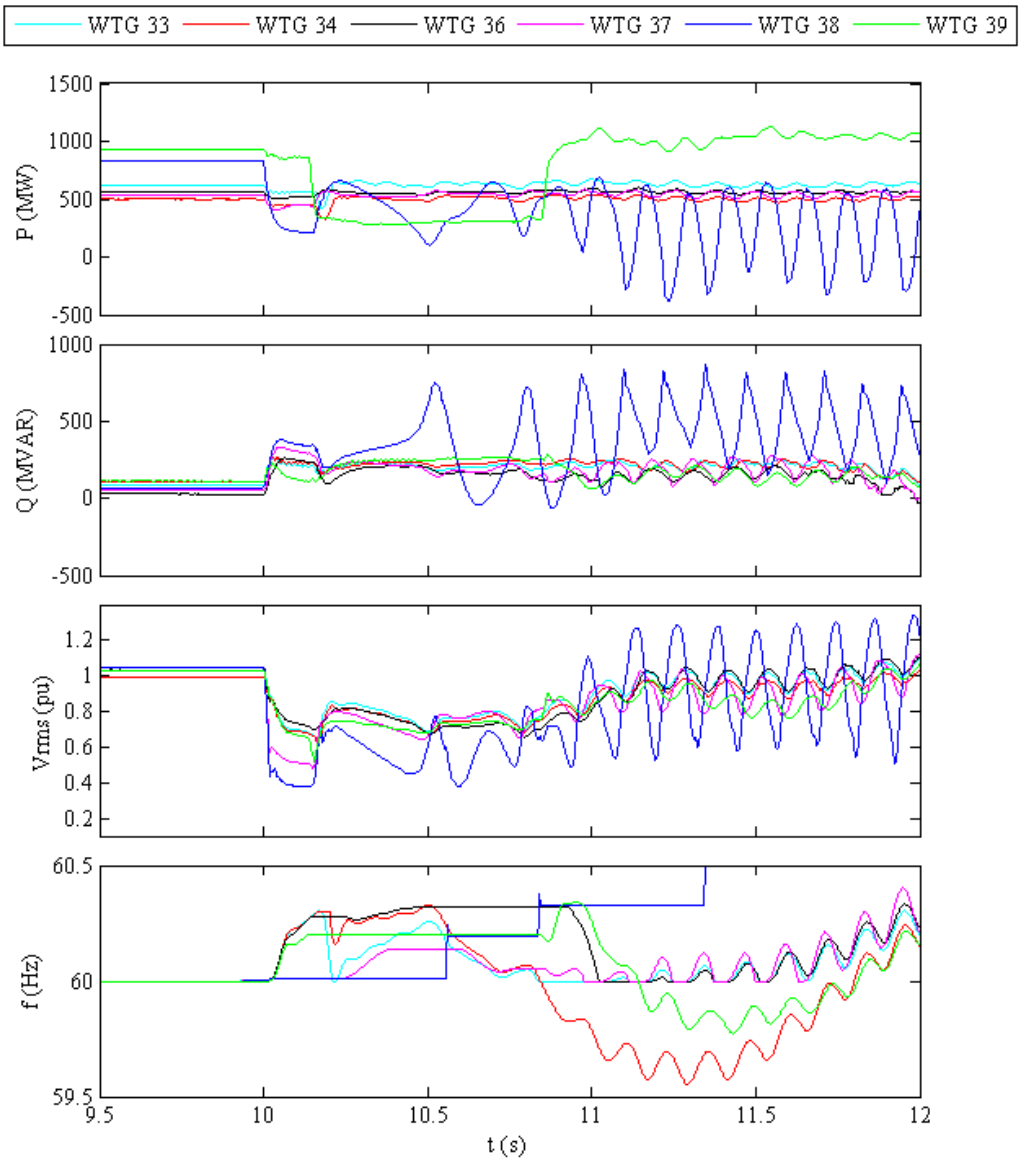

Figure 5.19: P, Q, Vrms at the POI and PLL frequency of the wind plants during an unstable power swing (S2)

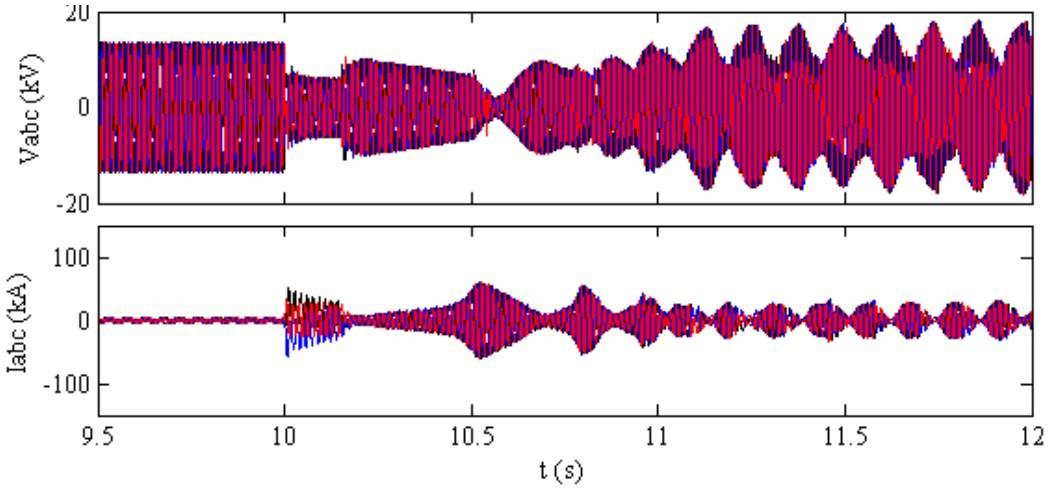

Figure 5.20: Phase voltages and currents of the synchronous generator at bus 32 for the unstable power swing (S2)

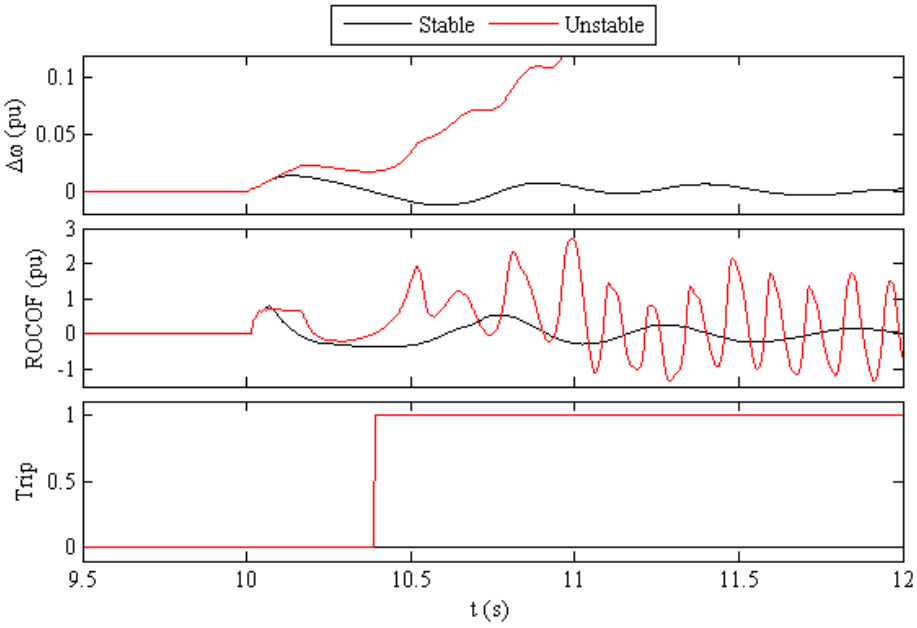

Figure 5.21: ω vs t trajectories used by the proposed method for stable and unstable power swings (S1 and S2)

5.6 Concluding Remarks

Loss of synchronism protection in weak grids with high penetration of inverter based resources poses distinct challenges, primarily due to reduced short-circuit currents, distorted voltage/current waveforms, and the complex dynamic interactions between IBRs and conventional generation sources. Traditional loss of synchronism protection methods, which typically depend on predictable impedance trajectories or rotor angle divergence, may fail to operate reliably in these complex systems. This study investigates the impact of IBR integration on the proposed relative speed based loss of synchronism protection scheme.

A modified IEEE 39 bus test system was developed in PSCAD/EMTDC to assess these impacts under two IBR penetration stages. Stage 1 represents a weak grid with partial IBR replacement, while Stage 2 simulates an extremely weak grid with higher IBR integration. The study involved 200 simulation scenarios, including faults and non-fault disturbances, with both synchronous generators and condensers under varying conditions.

Results showed that the proposed loss of synchronism detection method successfully identified 194 out of 200 scenarios, achieving an overall 97% accuracy. All 6 missed detections occurred under extreme weak grid conditions, where fast swing dynamics prevented the detection algorithm from capturing necessary rotor speed transitions. Despite these challenges, the method demonstrated high reliability across most scenarios and highlighted the importance of adapting protection settings for high IBR environments.

Chapter 6

Conclusions and Contributions

This chapter presents a summary of the thesis, draws conclusions from the research, highlights the key contributions, and proposes potential avenues for future work in the area of loss of synchronism protection.

6.1 Summary

Loss of synchronism protection is essential to avoid widespread outages and equipment damage that may result from voltage or angular instability. While a range of protection methods spanning traditional impedance-based schemes to more advanced dynamic approaches have been developed for synchronous machines, these methods often face challenges in complexity, adaptability, and computational demands. Also a notable gap exists in the literature on loss of synchronism in synchronous condensers, largely due to its historically low occurrence. However, with the increasing reliance on power electronics-based generation and the challenges of weaker grids, synchronous

condensers now play a more critical role, making such conditions more relevant and highlighting the need for advanced, precise protection strategies.

A novel approach for detecting loss of synchronism conditions in synchronous generators utilizing estimated relative rotor speed is proposed in this thesis. The method comprises two key components: a "speed estimation algorithm" and an "loss of synchronism detection algorithm". The speed estimation algorithm calculates the relative speed and its rate of change using terminal voltage and current measurements, along with generator parameters. An EMT study was conducted to assess the sensitivity of the estimated relative speed to variations in generator data, measurement errors, and stator transients. The results validated the effectiveness of the proposed speed estimation method. The calculated relative speed values are then used as inputs for the loss of synchronism detection algorithm. The loss of synchronism detection algorithm evaluates rotor speed variations following a disturbance, identifying a loss of synchronism condition if the relative speed consistently increases or decreases within a swing cycle. It classifies a power swing as unstable if the relative speed at fault clearance and the first maximum (or minimum) share the same polarity. This proposed method was implemented as a custom component in PSCAD/EMTDC. Extensive time-domain simulation tests demonstrated its effectiveness, with results comparable to or better than those of traditional impedance based methods. The method offers enhanced reliability and security, with less critical threshold settings that reduce the need for frequent adjustments based on network conditions.

Synchronous generators have been extensively analyzed for their loss of synchronism behavior, resulting in a well-documented framework for predicting and mitigat-

ing such events. However, synchronous condensers, despite their increased usage in modern power systems, have not received the same level of scrutiny. Therefore, in depth analysis of the loss of synchronism phenomenon in synchronous condensers in the systems with IBRs, providing a theoretical explanation through the use of phasor diagrams is conducted. The study found that the loss of synchronism condition in synchronous condensers generally occurs without pole slipping. This is attributed to the strong coupling between the stator magnetic field and terminal voltage, as there is no prime mover or load involved. The impedance trajectories observed in the time-domain simulations were consistent with the theoretical analysis derived from phasor diagrams. Thus, conventional impedance-based loss of synchronism schemes that rely on the occurrence of pole slipping may be ineffective for protecting synchronous condensers during loss of synchronism conditions.

Furthermore, the relative speed-based loss of synchronism detection method, initially designed for synchronous generators, was adapted for use with synchronous condensers. Unlike conventional methods, this approach does not depend on network-specific settings. Time-domain simulations were performed to compare this method with several established traditional schemes. The results highlighted improved detection times and confirmed the method's reliability and security. Notably, the proposed relative speed-based method does not rely on the pole-slipping condition, unlike traditional impedance-based loss of synchronism protection schemes, which fail under such circumstances due to their dependence on pole-slipping.

Loss of synchronism protection in weak grids with high inverter-based resource penetration presents significant challenges due to reduced short-circuit strength and

complex dynamic interactions. Traditional impedance-based methods may become unreliable under such conditions. A case study is conducted to evaluate the performance of the proposed relative speed based loss of synchronism protection scheme in weak grids with high penetration of inverter based resources using a modified IEEE 39 bus system. Two IBR integration levels representing weak and extremely weak system conditions are considered. Study involved faults and non-fault disturbances, with both synchronous generators and condensers under varying system conditions. Across the simulated disturbance scenarios, the proposed method successfully detected the loss of synchronism in nearly all cases, achieving about a 97% success rate. Missed detections occurred only under extreme weak grid conditions, emphasizing the need to adapt protection settings in high IBR integrated environments.

6.2 Conclusions

A novel approach for detecting loss of synchronism conditions in synchronous generators based on estimated relative rotor speed was proposed. The proposed approach circumvents the challenges faced in setting traditional loss of synchronism protection schemes such as need for accurate system details, requirement for many dynamic simulations, and dependency on pole slipping condition for detection. The results of numerous EMT simulations confirmed the accuracy and effectiveness of the proposed relative rotor speed-based loss of synchronism protection schemes. Furthermore, comparisons showed that the new method is comparable to or better than the traditional impedance-based loss of synchronism protection schemes.

In depth analysis of the loss of synchronism phenomenon in synchronous condensers, providing a theoretical explanation through the use of phasor diagrams was conducted. The study found that the loss of synchronism condition in synchronous condensers generally occurs without slipping poles. Thus, conventional impedance-based loss of synchronism schemes that rely on the occurrence of pole slipping may be ineffective. With the growing use of synchronous condensers to overcome issues related to power electronics-based generation interconnected to weak systems, the presented theoretical analysis and clarification are highly relevant to the industry.

The proposed relative speed-based loss of synchronism protection scheme, initially designed for synchronous generators, was applied for synchronous condensers. Comparison of the performance of this method with those of well-established traditional schemes using time-domain simulations confirmed the improved detection times and the dependability and security of the protection scheme. Notably, the proposed method does not rely on the pole-slipping condition, unlike traditional impedance-based schemes. A case study was conducted to evaluate the performance of the proposed method in weak grids with high penetration of inverter-based resources using a modified version of the IEEE 39 bus system. Across the simulated disturbance scenarios, the proposed method successfully detected the loss of synchronism in nearly all cases, achieving about a 97% success rate. The few missed detections occurred only under extremely weak grid conditions, highlighting the need for further improvements in very high IBR integrated environments.

6.3 Contributions

The main contributions of the research work presented in this thesis are:

1. Development of a loss of synchronism protection scheme for synchronous generators based on rotor relative speed which can be configured with minimal effort.

2. Validation of the proposed methods' performance under various system disturbances.

3. Comparison of the proposed method's performance with established and novel loss of synchronism protection schemes.

4. Analysis of Synchronous condenser loss of synchronism phenomenon and the distinguish the difference between loss of synchronism and pole slipping.

5. Identification that synchronous condensers experience loss of synchronism conditions without pole slips.

6. Recognition that traditional impedance-based loss of synchronism protection relays may be ineffective for detecting loss of synchronism conditions in synchronous condensers.

7. Demonstration of the effectiveness of the proposed loss of synchronism method for synchronous condensers since it does not rely on the pole slipping condition.

8. Validation of the proposed method's performance in synchronous condenser applications under various system disturbances.

9. Comparison of the proposed method's performance with established synchronous condenser loss of synchronism protection schemes.

10. Investigation of the proposed method's performance and accuracy in weak grids with high penetration of inverter-based generation.

11. Development of various EMT models for protection scheme validation studies.

These contributions have led to the following publications in journals:

1. **K. Samarawickrama**, A. D. Rajapakse, and N. Perera, "Generator out-of-step protection using the trajectory of estimated relative speed", Electric Power Systems Research, vol. 223, p. 109640, 2023.

2. **K. Samarawickrama**, A. D. Rajapakse, N. Perera, K. Manchur, and D. Lin, "Loss of Synchronism Protection of Synchronous Condensers in Modern Power Systems", IEEE Access journal, August 2025 (under review).

6.4 Future Work

This thesis introduces the development of a novel loss of synchronism protection scheme, focusing on the theoretical formulation, simulation-based validation, and performance evaluation under a wide range of operating conditions. However, prototype implementation of the proposed algorithm in a relay hardware is not explored. To advance towards real-world applicability, it will be essential to build a prototype of the relay and rigorously assess its stability, reliability, and computational efficiency under realistic system conditions.

In addition, the applicability of the proposed method to synchronous motors has not been studied. Therefore, it would be valuable to analyze the loss of synchronism phenomenon in synchronous motors and investigate whether the proposed method is suitable for such applications.

Further research could focus on examining speed variations in synchronous machines and their impact on the speed estimation and loss of synchronism detection algorithms when operating alongside emerging IBR technologies, such as grid-forming battery energy storage systems, large data centre loads. The rapid initial active power response during disturbances (e.g., phase jumps) may induce unique speed variations in synchronous machines, making this an intriguing area for future study.

Another promising direction for future research would be to analyze the applicability of the proposed method for clusters of generators. Investigating the calculation of an average speed for a group of generators and applying the proposed method to this average speed could provide insights into its potential extension to broader areas or systems.

References

[1] I. P. S. R. Committee *et al.*, "Ieee tutorial on the protection of synchronous generators," *IEEE PSRC WG J*, 2011.

[2] A. Pai, *Energy function analysis for power system stability*. Springer Science & Business Media, 1989.

[3] D. R. Gurusinghe and A. D. Rajapakse, "Post-disturbance transient stability status prediction using synchrophasor measurements," *IEEE Transactions on Power Systems*, vol. 31, no. 5, pp. 3656–3664, 2016.

[4] R. Jain, H. L. Hess, and B. K. Johnson, "Dfig based wind turbine system modeling in the real time digital simulator," in *2014 North American Power Symposium (NAPS)*. IEEE, 2014, pp. 1–6.

[5] S. Shah and V. Gevorgian, "Control, operation, and stability characteristics of grid-forming type iii wind turbines," National Renewable Energy Lab.(NREL), Golden, CO (United States), Tech. Rep., 2020.

[6] F. Cupertino, E. Lavopa, P. Zanchetta, M. Sumner, and L. Salvatore, "Running dft-based pll algorithm for frequency, phase, and amplitude tracking in aircraft electrical systems," *IEEE Transactions on Industrial Electronics*, vol. 58, no. 3, pp. 1027–1035, 2011.

[7] PTI, *PSS/E Model Library*, 34th ed., Siemens Power Technologies International, 400 State Street, Schenectady, NY 12301-1058 USA, Aug. 2023.

[8] M. McDonald, D. Tziouvaras, A. Apostolov *et al.*, "Power swing and out-of-step considerations on transmission lines," *IEEE PSRC WG D*, vol. 6, p. 2005, 2005.

[9] T. J. Hammons, "Electrical damping and its effect on accumulate fatigue life expenditure of turbine-generator shafts following worst-case supply system disturbances," *IEEE Transactions on Power Apparatus and Systems*, vol. PAS-102, no. 6, pp. 1552–1565, June 1983.

[10] J. Berdy, W. A. Elmore, L. E. Goff, W. C. New, G. C. Parr, A. H. Summers, and C. L. Wagner, "Loss of excitation protection for modern synchronous generators," *IEEE Transactions on Power Apparatus and Systems*, vol. 94, no. 5, pp. 1457–1463, Sep. 1975.

[11] D. A. Tziouvaras and D. Hou, "Out-of-step protection fundamentals and advancements," in *57th Annual Conference for Protective Relay Engineers, 2004.* IEEE, 2004, pp. 282–307.

[12] C. J. Mozina, "Impact of power system instability on generator protection," in *PES T D 2012*, May 2012, pp. 1–8.

[13] M. Aghazadeh and A. Kazemi, "A novel fast algorithm for detecting out-of-step using equal area criterion," in *2016 24th Iranian Conference on Electrical Engineering (ICEE)*, May 2016, pp. 931–936.

[14] E. Farantatos, R. Huang, G. J. Cokkinides, and A. P. Meliopoulos, "A predictive generator out-of-step protection and transient stability monitoring scheme enabled by a distributed dynamic state estimator," *IEEE Transactions on Power Delivery*, vol. 31, no. 4, pp. 1826–1835, Aug 2016.

[15] J. Blumschein, Y. Yelgin, and M. Kereit, "Proper detection and treatment of power swing to reduce the risk of blackouts," in *2008 Third International Conference on Electric Utility Deregulation and Restructuring and Power Technologies*, April 2008, pp. 2440–2446.

[16] K. Malmedal, P. K. Sen, and J. P. Nelson, "Application of out-of-step relaying for small generators in distributed generation," *IEEE Transactions on Industry Applications*, vol. 41, no. 6, pp. 1506–1514, Nov 2005.

[17] B. Alinejad and H. Kazemi Karegar, "A novel out-of-step relay using wide area measurements," in *2014 5th Conference on Thermal Power Plants (CTPP)*, June 2014, pp. 7–11.

[18] B. Alinezhad and H. K. Karegar, "Out-of-step protection based on equal area criterion," *IEEE Transactions on Power Systems*, vol. 32, no. 2, pp. 968–977, March 2017.

[19] A. Sauhats, A. Utans, D. Antonovs, and A. Svalovs, "Multi-terminal out-of-step protection system," in *2016 IEEE 16th International Conference on Environment and Electrical Engineering (EEEIC)*, June 2016, pp. 1–6.

[20] S. Paudyal and R. Gokaraju, "Out-of-step protection for multi-machine power systems using local measurements," in *2015 IEEE Eindhoven PowerTech*, June 2015, pp. 1–6.

[21] B. Shrestha, R. Gokaraju, and M. Sachdev, "Out-of-step protection using state-plane trajectories analysis," *IEEE Transactions on Power Delivery*, vol. 28, no. 2, pp. 1083–1093, April 2013.

[22] D. Hou and D. A. Tziouvaras, "Out-of-step protection enhancements," in *2004 Eighth IEE International Conference on Developments in Power System Protection*, vol. 1, April 2004, pp. 5–10 Vol.1.

[23] A. Y. Abdelaziz, M. R. Irving, M. M. Mansour, A. M. El-Arabaty, and A. I. Nosseir, "Adaptive protection strategies for detecting power system out-of-step conditions using neural networks," *IEE Proceedings - Generation, Transmission and Distribution*, vol. 145, no. 4, pp. 387–394, July 1998.

[24] M. Rasoulpour, T. Amraee, and A. K. Sedigh, "A relay logic for total and partial loss of excitation protection in synchronous generators," *IEEE Transactions on Power Delivery*, vol. 35, no. 3, pp. 1432–1442, 2020.

[25] Q. Verzosa, "Realistic testing of power swing blocking and out-of-step tripping functions," in *2013 66th Annual Conference for Protective Relay Engineers*, 2013, pp. 420–449.

[26] D. Celeita, M. Gutierrez, M. Toro, and G. Ramos, "Out-of-step protection modeling for virtual playback testing applied to industrial generators," *IEEE Transactions on Industry Applications*, vol. 55, no. 3, pp. 2472–2480, 2019.

[27] J. R. Camarillo-Penaranda, D. Celeita, M. Gutierrez, M. Toro, and G. Ramos, "An approach for out-of-step protection based on swing center voltage estimation and analytic geometry parameters," *IEEE Transactions on Industry Applications*, vol. 56, no. 3, pp. 2402–2408, 2020.

[28] C. W. Taylor, J. M. Haner, L. A. Hill, W. A. Mittelstadt, and R. L. Cresap, "A new out-of-step relay with rate of change of apparent resistance augmentation," *IEEE Power Engineering Review*, vol. PER-3, no. 3, pp. 32–32, 1983.

[29] J. M. Haner, T. D. Laughlin, and C. W. Taylor, "Experience with the r-rdot out-of-step relay," *IEEE Transactions on Power Delivery*, vol. 1, no. 2, pp. 35–39, 1986.

[30] A. Sauhats, A. Utans, and E. Biela-Dalidovicha, "Equal area criterion and angle control-based out-of-step protection," in *2017 IEEE 58th International Scientific Conference on Power and Electrical Engineering of Riga Technical University (RTUCON)*, 2017, pp. 1–6.

[31] M. N. Pala, A. Thakar, and A. Patel, "Power swing and out of step protection using equal area criteria," in *2019 IEEE 5th International Conference for Convergence in Technology (I2CT)*, 2019, pp. 1–7.

[32] V. Centeno, A. G. Phadke, A. Edris, J. Benton, M. Gaudi, and G. Michel, "An adaptive out-of-step relay [for power system protection]," *IEEE Transactions on Power Delivery*, vol. 12, no. 1, pp. 61–71, 1997.

[33] M. A. Redfern and M. J. Checkfield, "A new pole slipping protection algorithm for dispersed storage and generation using the equal area criterion," *IEEE Transactions on Power Delivery*, vol. 10, no. 1, pp. 194–202, 1995.

[34] M. A. Redfern and M. J. Checksfield, "A study into a new solution for the problems experienced with pole slipping protection [of synchronous generators]," *IEEE Transactions on Power Delivery*, vol. 13, no. 2, pp. 394–404, 1998.

[35] S. Paudyal, G. Ramakrishna, and M. S. Sachdev, "Application of equal area criterion conditions in the time domain for out-of-step protection," *IEEE Transactions on Power Delivery*, vol. 25, no. 2, pp. 600–609, 2010.

[36] Shengli Cheng and M. S. Sachdev, "Out-of-step protection using the equal area criterion," in *Canadian Conference on Electrical and Computer Engineering, 2005.*, 2005, pp. 1488–1491.

[37] M. Abedini, M. Davarpanah, M. Sanaye-Pasand, S. M. Hashemi, and R. Iravani, "Generator out-of-step prediction based on faster-than-real-time analysis: Concepts and applications," *IEEE Transactions on Power Systems*, vol. 33, no. 4, pp. 4563–4573, 2018.

[38] K. h. So, J. y. Heo, C. h. Kim, R. K. Aggarwal, and K. b. Song, "Out-of-step detection algorithm using frequency deviation of voltage," *IET Generation, Transmission Distribution*, vol. 1, no. 1, pp. 119–126, 2007.

[39] B. Shrestha, P. Sharma, and R. Gokaraju, "Out-of-step protection using the analysis of electrical power vs speed deviation in state plane," in *IEEE PES ISGT Europe 2013*, 2013, pp. 1–5.

[40] H. Yaghobi, "Out-of-step protection of generator using analysis of angular velocity and acceleration data measured from magnetic flux," *Electric Power Systems Research*, vol. 132, pp. 9 – 21, 2016.

[41] S. M. Brahma, "Distance relay with out-of-step blocking function using wavelet transform," *IEEE Transactions on Power Delivery*, vol. 22, no. 3, pp. 1360–1366, 2007.

[42] R. Sandoval, A. Guzman, and H. J. Altuve, "Dynamic simulations help improve generator protection," in *2007 Power Systems Conference: Advanced Metering, Protection, Control, Communication, and Distributed Resources*, 2007, pp. 16–38.

[43] M. Donolo, P. Donolo, S. Patel, and V. Yedidi, "Performance of synchronous motors loss-of-synchronism protection," in *2017 Petroleum and Chemical Industry Technical Conference (PCIC)*, 2017, pp. 71–78.

[44] I. P. PSRC, "Ieee guide for ac motor protection - redline," *IEEE Std C37.96-2012 (Revision of IEEE Std C37.96-2000) - Redline*, pp. 1–278, 2013.

[45] A. H. Hoffmann, C. Raczkowski, and R. B. Squires, "Relaying for synchronous motor pullout protection," *Transactions of the American Institute of Electrical Engineers. Part III: Power Apparatus and Systems*, vol. 78, no. 3, pp. 618–623, 1959.

[46] F. Jebali and K. Garg, "High-inertia synchronous motor protection and lessons learned," in *proceedings of the 41st Annual Western Protective Relay Conference, Spokane, WA*, 2014.

[47] M. A. Donolo, "Speed and angle monitor for rotating machinery," United States of America Patent 14/962,155, Jun. 8, 2017, uS Patent App. 14/962,155.

[48] P. Kundur, N. J. Balu, and M. G. Lauby, *Power system stability and control*. McGraw-hill New York, 1994, vol. 7.

[49] S. Filizadeh, *Electric machines and drives: principles, control, modeling, and simulation*. CRC Press, 2013.

[50] R. H. Park, "Two-reaction theory of synchronous machines generalized method of analysis-part i," *Transactions of the American Institute of Electrical Engineers*, vol. 48, no. 3, pp. 716–727, 1929.

[51] SEL, *SEL-700G Generator and Intertie Protection Relays: Instruction Manual*, Schweitzer Engineering Laboratories, Aug. 2022.

[52] PTI, *Program Operation Manual*, 34th ed., Siemens Power Technologies International, 400 State Street, Schenectady, NY 12301-1058 USA, Aug. 2023.

[53] Electranix Corporation, *E-TRAN Translator for Power System Simulation*, 6th ed., Electranix Corporation, 12-75 Scurfield Blvd. Winnipeg, MB R3Y 1G4 Canada, July 2020.

[54] Manitoba HVDC Research Centre, *User's guide on the use of PSCAD*, 5th ed., Manitoba HVDC Research Centre, a division of Manitoba Hydro International Ltd, 211 Commerce Drive, Winnipeg, Manitoba, Canada R3P 1A3, February 2010.

[55] K. Samarawickrama, A. D. Rajapakse, and N. Perera, "Generator out-of-step protection using the trajectory of estimated relative speed," *Electric Power Systems Research*, vol. 223, p. 109640, 2023.

[56] WestinghouseElectric, *Westinghouse Type KSN Out-of-Step Notching Relay: Supplementary Instructions (IL 639949A)*, Westinghouse Electric Corporation, Newark, NJ, Jul. 1963.

[57] S. M. Hashemi and M. Sanaye-Pasand, "Current-based out-of-step detection method to enhance line differential protection," *IEEE Transactions on Power Delivery*, vol. 34, no. 2, pp. 448–456, 2019.

[58] S. Zhang and Y. Zhang, "Characteristic analysis and calculation of frequencies of voltages in out-of-step oscillation power system and a frequency-based out-of-step protection," *IEEE Transactions on Power Systems*, vol. 34, no. 1, pp. 205–214, 2019.

[59] S. M. Hashemi and M. Sanaye-Pasand, "Distance protection during asymmetrical power swings: Challenges and solutions," *IEEE Transactions on Power Delivery*, vol. 33, no. 6, pp. 2736–2745, 2018.

[60] H. Zare, H. Yaghobi, and Y. Alinejad-Beromi, "Adaptive concept of controlled islanding in power systems for wide-area out-of-step prediction of synchronous generators based on adaptive tripping index," *IET Generation, Transmission & Distribution*, vol. 12, no. 16, pp. 3829–3836, 2018.

[61] A. Banaiemoqadam, A. Hooshyar, and M. A. Azzouz, "A comprehensive dual current control scheme for inverter-based resources to enable correct operation of protective relays," *IEEE Transactions on Power Delivery*, vol. 36, no. 5, pp. 2715–2729, 2021.

[62] M. R. Behnke, G. Custer, E. Farantatos, N. Fischer, R. Guttromson, A. Isaacs, R. Majumder, S. Pant, M. Patel, V. Reddy-Konala *et al.*, "Impact of inverter based resource negative sequence current injection on transmission system protection," Sandia National Laboratories (SNL-NM), Albuquerque, NM, United States, Tech. Rep., 2020.

[63] A. Haddadi, I. Kocar, and E. Farantatos, "Impact of inverter-based resources on protection schemes based on negative sequence components," *EPRI: Palo Alto, CA, USA*, vol. 36, no. 1, pp. 289–98, 2019.

[64] A. Haddadi, I. Kocar, U. Karaagac, H. Gras, and E. Farantatos, "Impact of wind generation on power swing protection," *IEEE Transactions on Power Delivery*, vol. 34, no. 3, pp. 1118–1128, 2019.

[65] A. Haddadi, E. Farantatos, I. Kocar, and U. Karaagac, "Impact of inverter based resources on system protection," *Energies*, vol. 14, no. 4, 2021.

[66] A. Haddadi, M. Zhao, I. Kocar, U. Karaagac, K. W. Chan, and E. Farantatos, "Impact of inverter-based resources on negative sequence quantities-based protection elements," *IEEE Transactions on Power Delivery*, vol. 36, no. 1, pp. 289–298, 2021.

[67] A. Jalilian and K. M. Muttaqi, "Current-based directional relaying scheme to protect series compensated transmission lines used to transmit bulk power produced by power electronics interfaced renewable energy power plants," *IET Generation, Transmission & Distribution*, vol. 14, no. 15, pp. 2976–2987, 2020.

[68] Y. Xiong, H. Wu, and X. Wang, "Efficacy analysis of power swing blocking and out-of-step tripping protection for grid-following-vsc systems," in *2023 8th IEEE Workshop on the Electronic Grid (eGRID)*, 2023, pp. 1–5.

[69] M. Jayamohan, S. Das, and S. Brahma, "Impedance trajectories during stable and unstable power swings in presence of pq control based pv generations," in *2023 IEEE Power and Energy Society General Meeting (PESGM)*, 2023, pp. 1–5.

[70] M. Nagpal, M. Jensen, M. Higginson *et al.*, "Protection challenges and practices for interconnecting inverter based resources to utility transmission systems," *IEEE Power Energy Soc*, pp. 1–65, 2020.

[71] G. Kou, L. Chen, P. VanSant, F. Velez-Cedeno, and Y. Liu, "Fault characteristics of distributed solar generation," *IEEE Transactions on Power Delivery*, vol. 35, no. 2, pp. 1062–1064, 2020.

[72] S. M. Hashemi and M. Sanaye-Pasand, "A new predictive approach to wide-area out-of-step protection," *IEEE Transactions on Industrial Informatics*, vol. 15, no. 4, pp. 1890–1898, 2019.

[73] M. Sharifzadeh, H. Lesani, and M. Sanaye-Pasand, "A new algorithm to stabilize distance relay operation during voltage-degraded conditions," *IEEE Transactions on Power Delivery*, vol. 29, no. 4, pp. 1639–1647, 2014.

[74] P. K. Nayak, A. K. Pradhan, and P. Bajpai, "Secured zone 3 protection during stressed condition," *IEEE Transactions on Power Delivery*, vol. 30, no. 1, pp. 89–96, 2015.

[75] M. Paolone, T. Gaunt, X. Guillaud, M. Liserre, S. Meliopoulos, A. Monti, T. Van Cutsem, V. Vittal, and C. Vournas, "Fundamentals of power systems modelling in the presence of converter-interfaced generation," *Electric Power Systems Research*, vol. 189, p. 106811, 2020.

[76] M. A. Nasr and A. Hooshyar, "Power swing in systems with inverter based resources Part I: Dynamic model development," *IEEE Transactions on Power Delivery*, vol. 39, no. 3, pp. 1889–1902, 2024.

[77] M. A. Nasr and A. Hooshyar, "Power swing in systems with inverter based resources Part II: Impact on protection systems," *IEEE Transactions on Power Delivery*, vol. 39, no. 3, pp. 1903–1917, 2024.

[78] J. J. Grainger and W. D. Stevenson, *Power system analysis*. McGraw-Hill New York, 1994, vol. 67.

[79] V. Gevorgian and E. Muljadi, "Wind power plant short circuit current contribution for different fault and wind turbine topologies," National Renewable Energy Lab.(NREL), Golden, CO (United States), Tech. Rep., 2010.

[80] E. Lavopa, P. Zanchetta, M. Sumner, and F. Cupertino, "Real-time estimation of fundamental frequency and harmonics for active shunt power filters in aircraft electrical systems," *IEEE Transactions on Industrial Electronics*, vol. 56, no. 8, pp. 2875–2884, 2009.

Appendix A

Test System Data

This appendix presents the system data used for modelling various test systems in this thesis.

A.1 Five Bus Test System from IEEE PSRC Generator Protection Tutorial

A single line diagram of the test network is depicted in Figure A.1. The network and generator parameters are shown in Section A.1.1 through A.1.3 [78]. Section A.1.4 provides the load-flow solution of the test network prior to any outages.

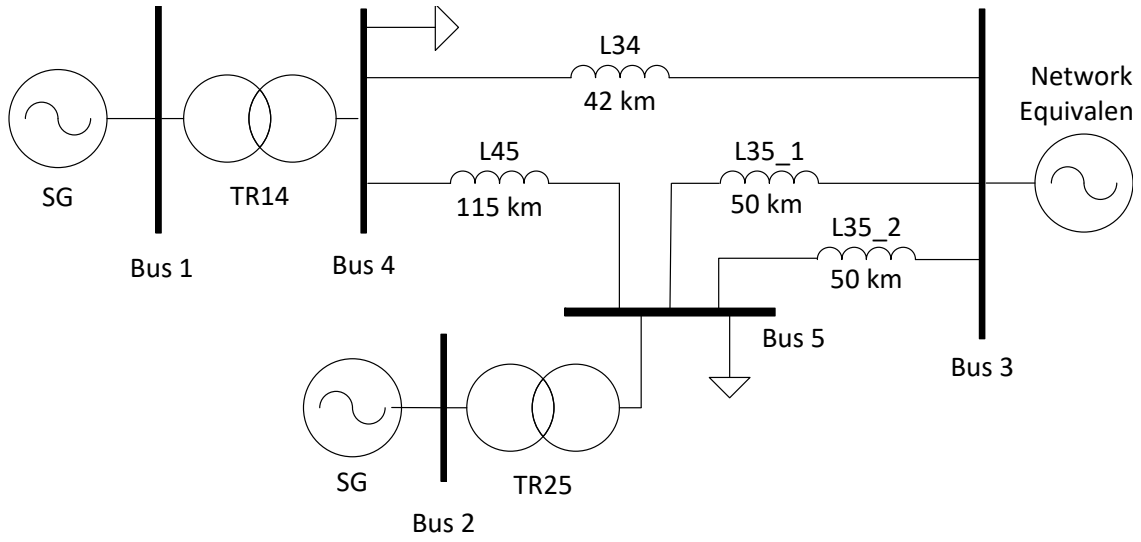

Figure A.1: Five bus test system from IEEE PSRC generator protection tutorial [1]

A.1.1 Machine Parameters

Synchronous generator parameters are in pu on 18 kV and machine base of 400 MVA for bus 1 unit and on 20 kV and machine base of 250 MVA for bus 2 unit.

Table A.1: Synchronous machine parameters of the five bus test system in Figure A.1

Bus No.	$\mathbf{R_a}$ **(pu)**	$\mathbf{X_l}$ **(pu)**	$\mathbf{X_d}$ **(pu)**	$\mathbf{X_q}$ **(pu)**	$\mathbf{X'_d}$ **(pu)**	$\mathbf{X'_q}$ **(pu)**	$\mathbf{X''_d}$ **(pu)**	$\mathbf{X''_q}$ **(pu)**	**H (s)**	$\mathbf{T'_{do}}$ **(s)**	$\mathbf{T'_{qo}}$ **(s)**	$\mathbf{T''_{do}}$ **(s)**	$\mathbf{T''_{qo}}$ **(s)**
1	0.00129	0.130	0.920	0.510	0.268	0.228	0.135	0.200	2.8	4.3	0.85	0.032	0.05
2	0.00129	0.130	0.920	0.510	0.250	0.228	0.135	0.200	3.2	4.3	0.85	0.032	0.05

A.1.2 Transmission Line Parameters

The transmission line parameters are in pu on 230 kV and the system base of 100 MVA.

Table A.2: Transmission line parameters of the five bus test system in Figure A.1

From Bus	To Bus	R1 (pu)	X1 (pu)	B1 (pu)	R0 (pu)	X0 (pu)	B0 (pu)
3	4	0.007	0.040	0.082	0.0711	0.1042	0.0582
4	5	0.018	0.110	0.226	0.1827	0.2865	0.1605
3	5(1)	0.008	0.047	0.098	0.0812	0.1224	0.0696
3	5(2)	0.008	0.047	0.098	0.0812	0.1224	0.0696

A.1.3 Transformer Parameters

The transformer parameters are in pu on 230 kV and the system base of 100 MVA.

Table A.3: Transformer parameters of the five bus test system in Figure A.1

From Bus	To Bus	R (pu)	X (pu)
1	4	0.001	0.022
2	5	0.001	0.040

A.1.4 Pre-Disturbance Load-flow Solution

The values are in pu on the system base of 100 MVA.

Table A.4: Pre-disturbance load-flow solution of the five bus test system in Figure A.1

Bus No.	**Voltage**		**Generation**		**Load**	
	Mag. (pu)	**Angle (deg)**	**P (pu)**	**Q (pu)**	**P (pu)**	**Q (pu)**
1	1.030	8.88°	3.500	0.712	-	-
2	1.020	6.38°	1.850	0.298	-	-
3	1.000	0°	-	-	-	-
4	1.018	4.68°	-	-	1.00	0.44
5	1.011	2.27°	-	-	0.50	0.16

A.2 Modified Kundur's Two-area Test System

A single line diagram of the test network is depicted in Figure A.2. The network and synchronous condenser parameters are shown in Section A.2.1 through A.2.4. Section A.2.5 provides the load-flow solution of the test network prior to any outages.

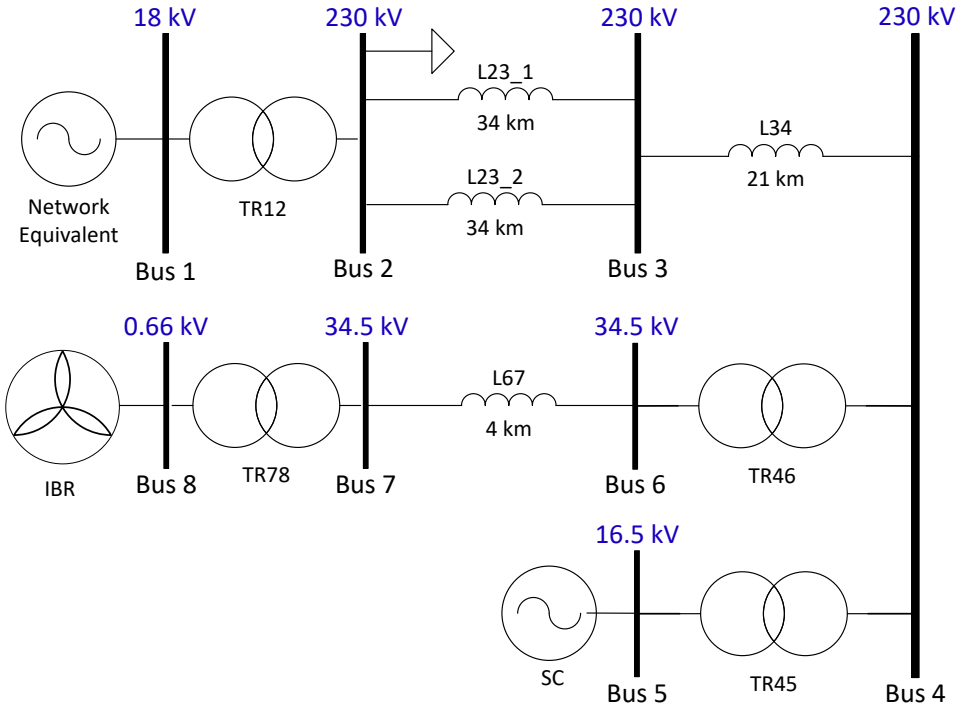

Figure A.2: The modified Kundur's two-area test system

A.2.1 Machine Parameters

The synchronous condenser parameters are in pu on 16.5 kV and machine base of 250 MVA

Table A.5: Synchronous condenser parameters of the modified Kundur's two-area test system

Bus No.	R_a (pu)	X_l (pu)	X_d (pu)	X_q (pu)	X'_d (pu)	X'_q (pu)	X''_d (pu)	X''_q (pu)	H (s)	T'_{do} (s)	T'_{qo} (s)	T''_{do} (s)	T''_{qo} (s)
5	0.00	0.11	1.45	1.14	0.33	1.139	0.217	0.2	2.403	9.14	999	0.19	0.65

A.2.2 Exciter Parameters

The exciter representation consists of three models: the Exciter, the Minimum Excitation Limiter, and the Voltage Regulator Current Compensating Model. The parameters for each model are provided in Tables A.6 through A.8

Table A.6: Exciter parameters of the modified Kundur's two-area test system

Bus No.	T_R	V_{IMAX}	V_{IMIN}	T_C	T_B	T_{C1}	T_{B1}	K_A	T_A
5	0.009	0.0270	-0.0230	1.2	2.12	0.65	0.65	600.0	0.01
	VA_{MAX}	VA_{MIN}	VR_{MAX}	VR_{MIN}	K_C	K_F	T_F	K_{LR}	I_{LR}
	10.0	-8.23	10.0	-8.23	0.08	0.0	1.0	50.0	2.84

Table A.7: Minimum excitation limiter parameters of the modified Kundur's two-area test system

Bus No.	K_{F2}	T_{F2}	K_M	T_M	MELMAX	Q_0	Radius
5	0.05	0.5	3.0	0.009	999	0.6	1.1

Table A.8: Voltage regulator current compensating model parameters of the modified Kundur's two-area test system

Bus No.	**R_C (pu)**	**X_C (pu)**
5	0.001	0.058

Voltage regulator current compensating model allows the voltage regulator of the machine to sense the voltage at a point separated from the machine terminals by an impedance of $R_C + jX_C$. Impedance values are in pu on the machine base of 250 MVA.

A.2.3 Transmission Line Parameters

The transmission line parameters are in pu on the system base of 100 MVA.

Table A.9: Transmission line parameters of the modified Kundur's two-area test system

From Bus	**To Bus**	**R1 (pu)**	**X1 (pu)**	**B1 (pu)**	**R0 (pu)**	**X0 (pu)**	**B0 (pu)**
6	7	0.0008	0.001	0.001	0.0081	0.0026	0.0007
3	4	0.0040	0.080	0.010	0.0406	0.2084	0.0071
2	3(1)	0.0080	0.110	0.020	0.0812	0.2865	0.0142
2	3(2)	0.0080	0.110	0.020	0.0812	0.2865	0.0142

A.2.4 Transformer Parameters

The transformer parameters are in pu on the transformer MVA base.

Table A.10: Transformer parameters of the modified Kundur's two-area test system

From Bus	**To Bus**	**R (pu)**	**X (pu)**	**MVA**
4	6	0.0010	0.1100	430
1	2	0.0050	0.1200	500
4	5	0.0053	0.0781	250
7	8	0.0010	0.0700	430

A.2.5 Pre-Disturbance Load-flow Solution

The values are in pu on the system base of 100 MVA.

Table A.11: Pre-disturbance load-flow solution of the modified Kundur's two-area test system

Bus No.	**Voltage**		**Generation**		**Load**	
	Mag. (pu)	**Angle (deg)**	**P (pu)**	**Q (pu)**	**P (pu)**	**Q (pu)**
1	1.0500	0.0°	-	-	-	-
2	1.0498	−1.337°	-	-	4.00	-1.0
3	1.0221	7.513°	-	-	-	-
4	1.0200	20.782°	-	-	-	-
5	1.0015	−9.243°	0.000	0.204	-	-
6	0.9979	25.216°	-	-	-	-
7	1.0005	25.379°	-	-	-	-
8	1.0057	28.167°	3.012	0.351	-	-

A.3 IEEE 39 Bus Test System

A single line diagram of the test network is depicted in Figure A.3. The network and machine parameters are shown in Section A.3.1 through A.3.4. Section A.3.5 provides the load-flow solution of the test network prior to any outages.

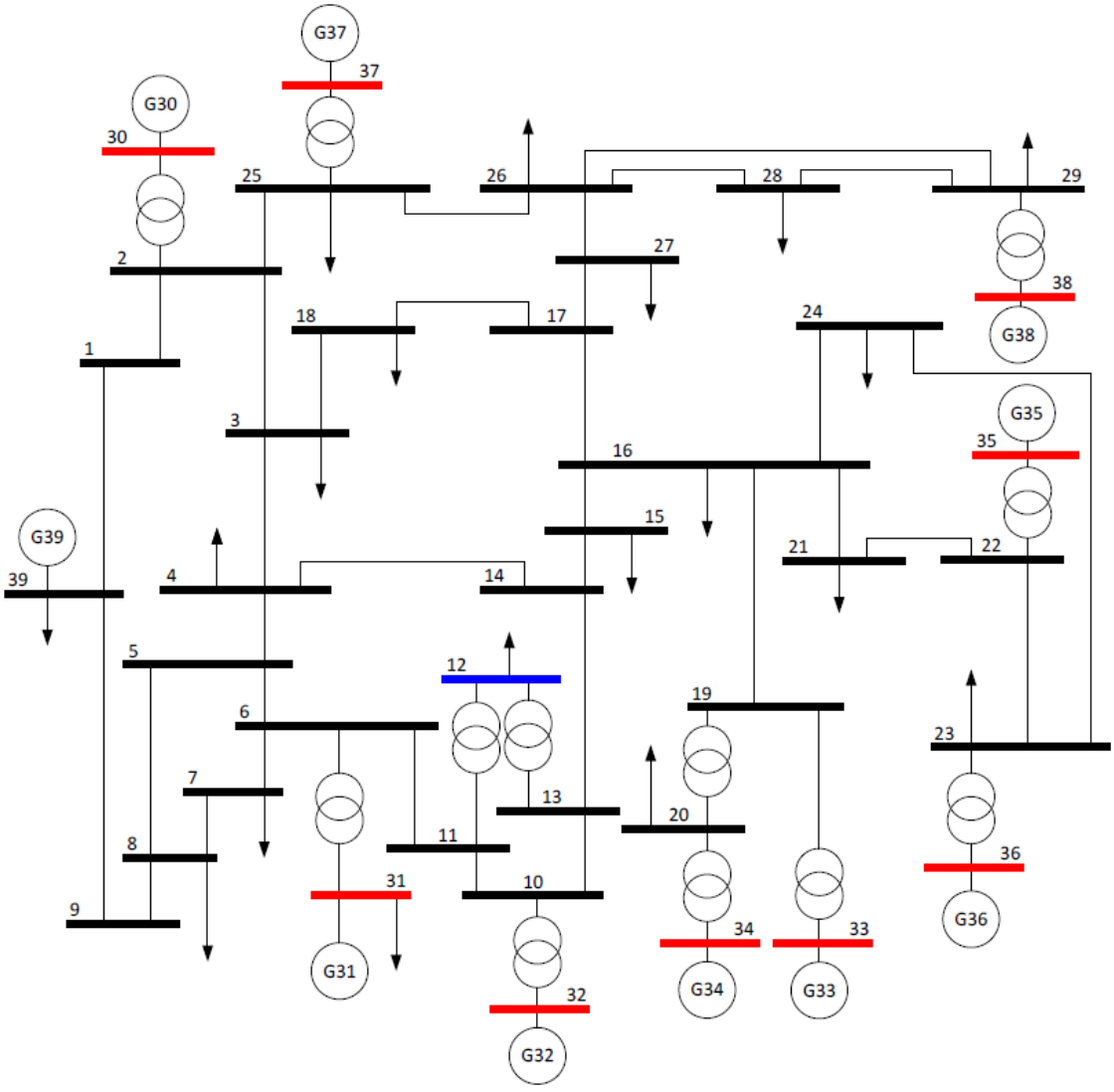

Figure A.3: IEEE 39 bus test system [2]

A.3.1 Machine Parameters

The synchronous machine parameters are in pu on the system base of 100 MVA.

Table A.12: Synchronous machine parameters of the IEEE 39 bus test system

Bus No.	$\mathbf{R_a}$ **(pu)**	$\mathbf{X_l}$ **(pu)**	$\mathbf{X_d}$ **(pu)**	$\mathbf{X_q}$ **(pu)**	$\mathbf{X'_d}$ **(pu)**	$\mathbf{X'_q}$ **(pu)**	$\mathbf{X''_d}$ **(pu)**	$\mathbf{X''_q}$ **(pu)**	**H (s)**	$\mathbf{T'_{do}}$ **(s)**	$\mathbf{T'_{qo}}$ **(s)**	$\mathbf{T''_{do}}$ **(s)**	$\mathbf{T''_{qo}}$ **(s)**
30	0.00125	0.0125	0.1	0.069	0.031	0.028	0.025	0.025	42.0	10.2	1.5	0.05	0.06
31	0.00125	0.035	0.295	0.282	0.0697	0.170	0.05	0.05	30.2	6.56	1.5	0.05	0.06
32	0.00125	0.0304	0.2495	0.237	0.0531	0.0876	0.045	0.045	35.8	5.7	1.5	0.05	0.06
33	0.00125	0.0295	0.262	0.258	0.0436	0.166	0.035	0.035	28.6	5.69	1.5	0.05	0.06
34	0.00125	0.027	0.67	0.62	0.132	0.166	0.05	0.05	26.0	5.4	0.44	0.05	0.06
35	0.00125	0.0224	0.254	0.241	0.05	0.0814	0.04	0.04	34.8	7.3	0.4	0.05	0.06
36	0.00125	0.0322	0.295	0.292	0.049	0.186	0.04	0.04	26.4	5.66	1.5	0.05	0.06
37	0.00125	0.028	0.290	0.280	0.057	0.0911	0.045	0.045	24.3	6.7	0.41	0.05	0.06
38	0.00125	0.0298	0.2106	0.205	0.057	0.0587	0.045	0.045	34.5	4.79	1.96	0.05	0.06
39	0.00125	0.003	0.02	0.019	0.006	0.008	0.05	0.05	500.0	7.0	0.7	0.05	0.06

A.3.2 Exciter Parameters

Table A.13: Exciter parameters of the IEEE 39 bus test system

Bus No.	$\mathbf{T_R}$	$\mathbf{K_A}$	$\mathbf{T_A}$	$\mathbf{V_{RMAX}}$	$\mathbf{V_{RMIN}}$	$\mathbf{K_E}$	$\mathbf{T_E}$	$\mathbf{K_F}$	$\mathbf{T_F}$	$\mathbf{E_1}$	$\mathbf{S_E(E_1)}$	$\mathbf{E_2}$	$\mathbf{S_E(E_2)}$
30	0	5	0.06	1	-1	0	0.25	0.04	1	3.54	0.08	4.728	0.26
31	0	6.2	0.05	1	-1	0	0.405	0.057	0.5	3.036	0.66	4.049	0.88
32	0	5	0.06	1	-1	0	0.5	0.08	1	2.342	0.13	3.123	0.34
33	0	5	0.06	1	-1	0	0.5	0.08	1	2.868	0.08	3.824	0.314
34	0	40	0.02	10	-10	1	0.785	0.03	1	3.927	0.07	5.236	0.91
35	0	5	0.02	1	-1	0	0.471	0.075	1.2	3.587	0.064	4.782	0.251
36	0	40	0.02	6.5	-6.5	1	0.73	0.03	1	2.8	0.53	3.8	0.74
37	0	5	0.02	1	-1	0	0.528	0.085	1.26	3.191	0.072	4.255	0.282
38	0	40	0.02	10.5	-10.5	1	1.4	0.03	1	4.257	0.62	5.676	0.85

A.3.3 Transmission Line Parameters

The transmission line parameters are in pu on the system base of 100 MVA.

Table A.14: Transmission line parameters of the IEEE 39 bus test system

From Bus	**To Bus**	**R1 (pu)**	**X1 (pu)**	**B1 (pu)**	**R0 (pu)**	**X0 (pu)**	**B0 (pu)**
1	2	0.0035	0.0411	0.6987	0.0473	0.1244	0.4411
1	39	0.0010	0.0250	0.7500	0.2331	0.0648	0.3691
2	3	0.0013	0.0151	0.2572	0.0053	0.0324	0.1656
2	25	0.0070	0.0086	0.1460	0.0101	0.0262	0.0919
3	4	0.0013	0.0213	0.2214	0.0067	0.0376	0.1489
3	18	0.0011	0.0133	0.2138	0.0045	0.0277	0.1416
4	5	0.0008	0.0128	0.1342	0.0041	0.0228	0.0900
4	14	0.0008	0.0129	0.1382	0.0041	0.0232	0.0916
5	6	0.0002	0.0026	0.0434	0.0009	0.0056	0.0284
5	8	0.0008	0.0112	0.1476	0.0040	0.0223	0.0883
6	7	0.0006	0.0092	0.1130	0.0032	0.0177	0.0701
6	11	0.0007	0.0082	0.1389	0.0029	0.0176	0.0898
7	8	0.0004	0.0046	0.0780	0.0016	0.0099	0.0504
8	9	0.0023	0.0363	0.3804	0.0114	0.0643	0.2552
9	39	0.0010	0.0250	1.2000	0.0118	0.0737	0.6143
10	11	0.0004	0.0043	0.0729	0.0015	0.0092	0.0471
10	13	0.0004	0.0043	0.0729	0.0015	0.0092	0.0471

13	14	0.0009	0.0101	0.1723	0.0035	0.0217	0.1109
14	15	0.0018	0.0217	0.3660	0.0075	0.0462	0.2369
15	16	0.0009	0.0094	0.1710	0.0114	0.0297	0.1039
16	17	0.0007	0.0089	0.1342	0.0029	0.0180	0.0918
16	19	0.0016	0.0195	0.3040	0.0065	0.0400	0.2048
16	21	0.0008	0.0135	0.2548	0.0136	0.0358	0.1579
16	24	0.0003	0.0059	0.0680	0.0020	0.0110	0.0433
17	18	0.0007	0.0082	0.1319	0.0028	0.0171	0.0875
17	27	0.0013	0.0173	0.3216	0.0173	0.0455	0.2009
21	22	0.0008	0.0140	0.2565	0.0139	0.0366	0.1613
22	23	0.0006	0.0096	0.1846	0.0098	0.0257	0.1133
23	24	0.0022	0.0350	0.3610	0.0109	0.0615	0.2440
25	26	0.0032	0.0323	0.5130	0.0108	0.0666	0.3425
26	27	0.0014	0.0147	0.2396	0.0050	0.0308	0.1576
26	28	0.0043	0.0474	0.7802	0.0040	0.0480	0.7861
26	29	0.0057	0.0625	1.0290	0.0209	0.1299	0.6787
28	29	0.0014	0.0151	0.2490	0.0052	0.0319	0.1630

A.3.4 Transformer Parameters

The transformer parameters are in pu on the system base of 100 MVA.

Table A.15: Transformer parameters of the IEEE 39 bus test system

From Bus	**To Bus**	**R (pu)**	**X (pu)**
12	11	0.0016	0.0435
12	13	0.0016	0.0435
6	31	0.0000	0.0250
10	32	0.0000	0.0200
19	33	0.0007	0.0142
20	34	0.0009	0.0180
22	35	0.0000	0.0143
23	36	0.0005	0.0272
25	37	0.0006	0.0232
2	30	0.0000	0.0181
29	38	0.0008	0.0156
19	20	0.0007	0.0138

A.3.5 Pre-Disturbance Load-flow Solution

The values (voltages, active and reactive power) are in pu on 230 kV and the system base of 100 MVA.

Table A.16: Pre-disturbance load-flow solution of the IEEE 39 bus test system

Bus No.	Voltage		Generation		Load		Bus No.	Voltage		Generation		Load	
	Mag. (pu)	Angle (deg)	P (pu)	Q (pu)	P (pu)	Q (pu)		Mag. (pu)	Angle (deg)	P (pu)	Q (pu)	P (pu)	Q (pu)
1	1.0474	-8.447	-	-	-	-	21	1.0318	-3.793	-	-	2.740	1.150
2	1.0487	-5.763	-	-	-	-	22	1.0498	0.656	-	-	-	-
3	1.0302	-8.608	-	-	3.220	0.024	23	1.0448	0.458	-	-	2.475	0.846
4	1.0039	-9.615	-	-	5.000	1.840	24	1.0373	-6.080	-	-	3.086	-0.92
5	1.0053	-8.618	-	-	-	-	25	1.0576	-4.373	-	-	2.240	0.472
6	1.0077	-7.956	-	-	-	-	26	1.0521	-5.537	-	-	1.390	0.170
7	0.9970	-10.13	-	-	2.338	0.840	27	1.0377	-7.506	-	-	2.810	0.755
8	0.9960	-10.62	-	-	5.220	1.760	28	1.0501	-2.025	-	-	2.060	0.276
9	1.0282	-10.33	-	-	-	-	29	1.0499	0.734	-	-	2.835	0.269
10	1.0172	-5.434	-	-	-	-	30	1.0475	-3.344	2.500	1.462	-	-
11	1.0127	-6.291	-	-	-	-	31	0.9820	0.000	5.212	1.983	0.092	0.046
12	1.0002	-6.251	-	-	0.075	0.880	32	0.9831	2.562	6.500	2.052	-	-
13	1.0143	-6.105	-	-	-	-	33	0.9972	4.183	6.320	1.099	-	-
14	1.0117	-7.665	-	-	-	-	34	1.0123	3.163	5.080	1.658	-	-
15	1.0154	-7.747	-	-	3.200	1.530	35	1.0493	5.618	6.500	2.124	-	-
16	1.0318	-6.200	-	-	3.294	0.323	36	1.0635	8.311	5.600	1.012	-	-
17	1.0336	-7.313	-	-	-	-	37	1.0278	2.411	5.400	0.004	-	-
18	1.0309	-8.235	-	-	1.580	0.300	38	1.0265	7.797	8.300	0.228	-	-
19	1.0499	-1.035	-	-	-	-	39	1.0300	-10.06	10.000	0.883	11.040	2.500
20	0.9912	-2.027	-	-	6.280	1.030							

Appendix B

Calculation of Protection Settings

This appendix outlines the procedures used to determine the settings for different loss of synchronism protection schemes.

B.1 Single Blinder Scheme Settings

Figure B.1 shows the impedance settings used by the single blinder scheme. The right and left blinders are symmetrical and the trip delay is set to zero. Blinder settings are calculated as shown in (B.1.1) and (B.1.2). δ is assumed as 120°. For simplicity in calculations, the system resistance (R_S) is neglected, making the reactance (X_S) equivalent to the impedance (Z_S).

$$78R1 = \left(\frac{X'_d + X_{TF} + X_S}{2}\right) \cdot tan\left(90 - \frac{\delta}{2}\right) \tag{B.1.1}$$

$$78R2 = -78R1 \tag{B.1.2}$$

Mho circle forward and reverse reaches were calculated as below.

$$78FWD = 2.5 \cdot X'_d \tag{B.1.3}$$

$$78REV = 1.75 \cdot X_{TF} \tag{B.1.4}$$

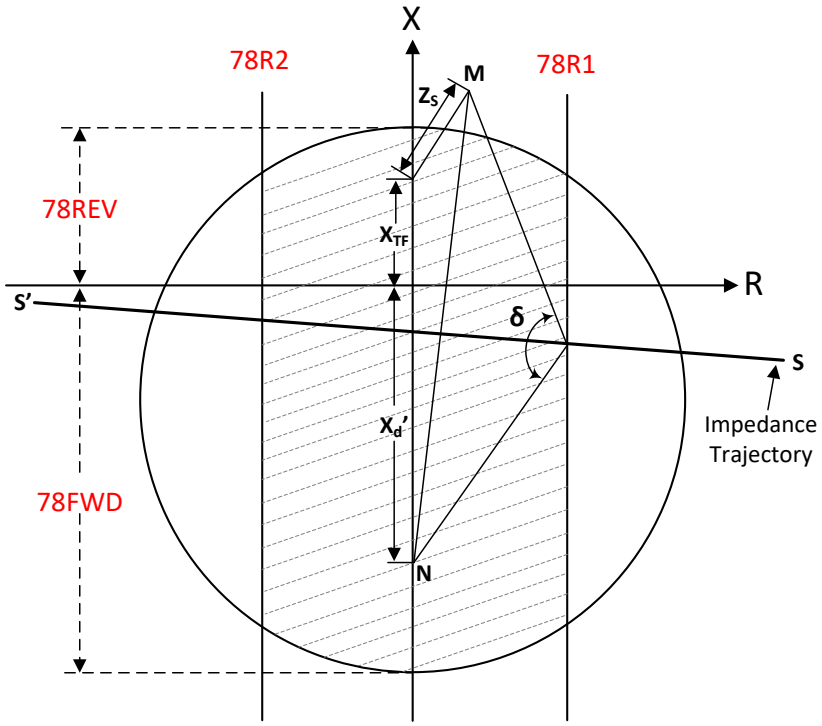

Figure B.1: Single blinder loss of synchronism protection settings

$78FWD$ = Forward reach

$78REV$ = Reverse reach

X'_d = Generator transient reactance

X_{TF} = Transformer reactance

Zs = System impedance

MN = Total impedance

SS' = Perpendicular bisector of line MN

δ = Angle between generator internal voltage and system at right blinder

B.2 Double Blinder Scheme Settings

Figure B.2 illustrates the impedance settings utilized by the double-blinder scheme. The right-side blinders are a mirror image of those on the left. The blinder settings are determined using (B.2.1) and (B.2.2), where δ is assumed to be 120°, and α, derived from a transient stability study, is set to 50°. The timer ($78D$) is set to 2 (60 Hz) cycles. For simplicity in calculations, the system resistance (R_S) is neglected, making the reactance (X_S) equivalent to the impedance (Z_S).

$$78R1 = \left(\frac{X'_d + X_{TF} + X_S}{2}\right) \cdot tan\left(90 - \frac{\alpha}{2}\right) \tag{B.2.1}$$

$$78R2 = \left(\frac{X'_d + X_{TF} + X_S}{2}\right) \cdot tan\left(90 - \frac{\delta}{2}\right) \tag{B.2.2}$$

Mho circle forward and reverse reaches were calculated as below.

$$78FWD = 2.5 \cdot X'_d \tag{B.2.3}$$

$$78REV = 1.75 \cdot X_{TF} \tag{B.2.4}$$

The outer blinder ($78R1$) and loss of synchronism timer ($78D$) should be set to satisfy the following:

- The outer blinder should not assert on maximum load.
- The outer blinder should lie outside the mho circle, to satisfy the relay logic.
- The outer blinder should separate from the inner blinder far enough to ensure that the $78D$ timer accurately times the loss of synchronism slip cycle.

Lets assume loss of synchronism relay processes the logic every half cycle of the system frequency - i.e. processing time step is 2 samples/cycles. To ensure that the relay times the loss of synchronism slip frequency accurately, the outer and inner blinders must be separated appropriately. For example, assume that the highest loss of synchronism slip frequency encountered is five slip cycles per second, which translates to 30° per cycle (60 Hz). Set the blinders with a 70° separation. This separation translates to a positive-sequence impedance travel time of 2.3 cycles between the two blinders, which should provide adequate timing accuracy. Set the 78D timer at approximately 0.034 seconds (two cycles), which ensures that 78D will pickup for swings travelling at 30° per cycle or less. The loss of synchronism slip frequency is a system-specific value. A transient stability study normally determines this variable and, therefore, the double-blinder settings.

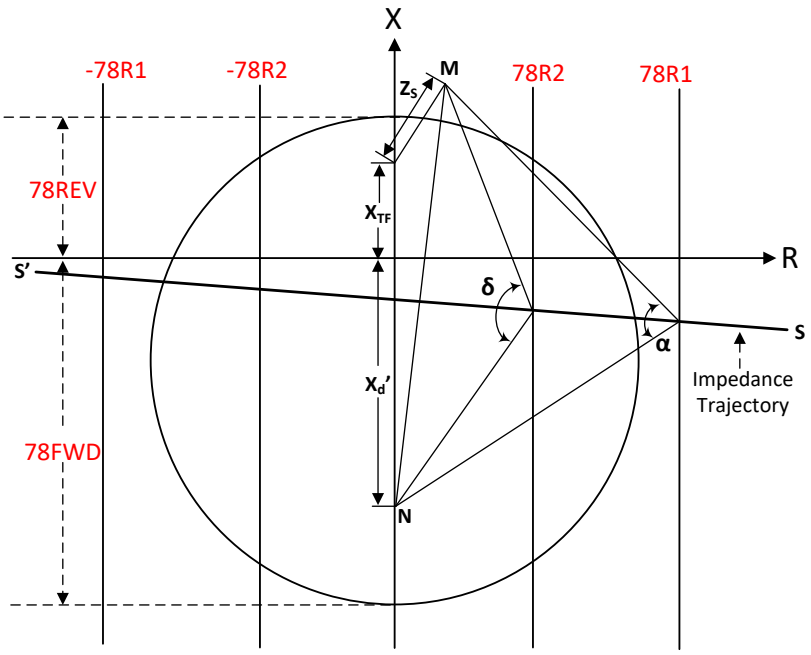

Figure B.2: Double blinder loss of synchronism protection settings

$78FWD$ = Forward reach

$78REV$ = Reverse reach

X'_d = Generator transient reactance

X_{TF} = Transformer reactance

Zs = System impedance

MN = Total impedance

SS' = Perpendicular bisector of line MN

α = Angle between generator internal voltage and system at outer blinder

δ = Angle between generator internal voltage and system at inner blinder

B.3 Loss of Excitation Scheme Settings

Figure B.3 shows the impedance settings used by the loss of excitation scheme. Zone 1 and 2 delays are set to 6 cycles (0.1s) and 30 cycles (0.5s), respectively.

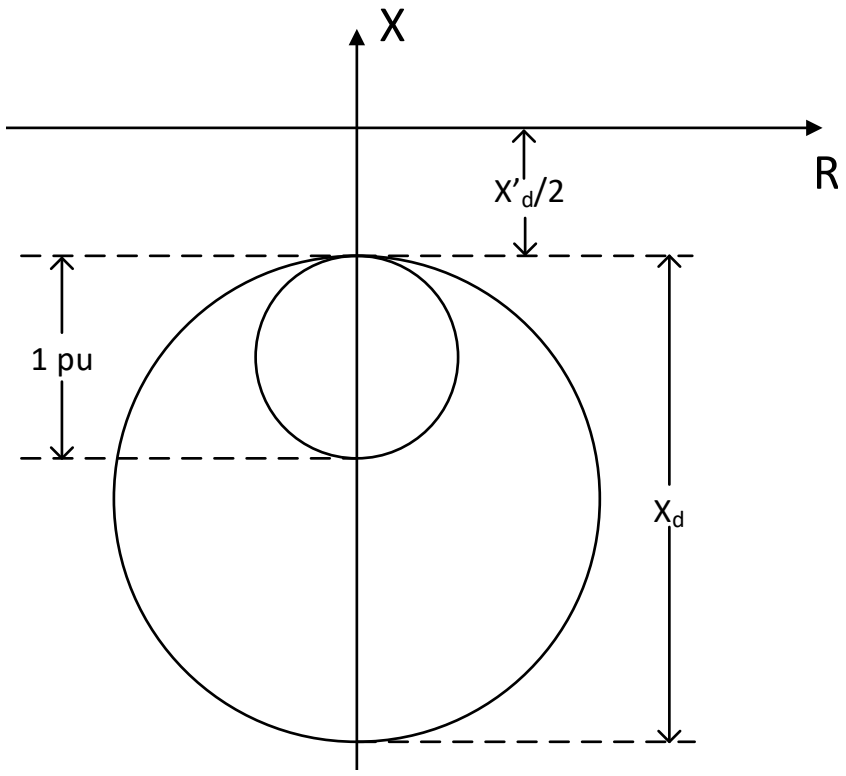

Figure B.3: Loss of excitation protection settings

B.4 ROCOV Schemes Settings

The stability boundary is illustrated in Figure B.4. It is established using two reference lines: a vertical line, AB, parallel to the *ROCOV* axis, positioned slightly outside the marginal stability point $B(x_1, y_1)$; and a horizontal line, CD, parallel to the ΔV axis, located just outside of the marginal stability point $C(x_2, y_2)$. The marginal stability point is obtained using a transient stability study performed by varying fault durations at different fault locations.

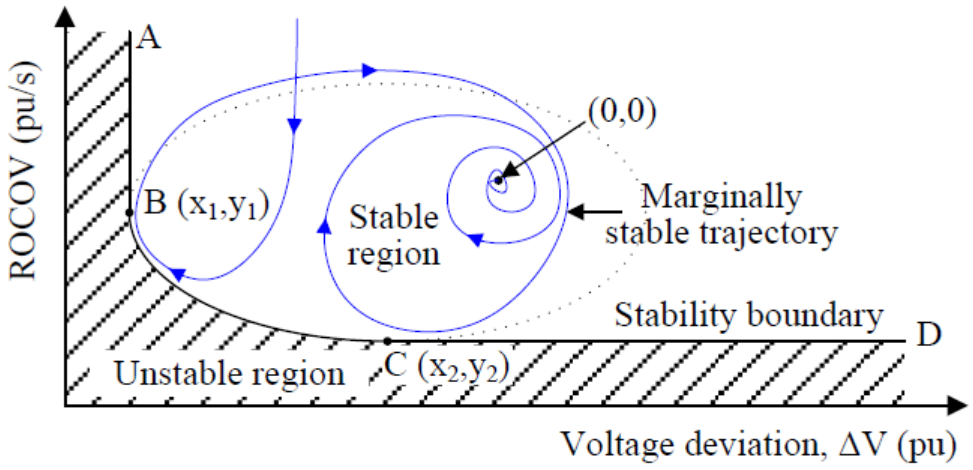

Figure B.4: Stability boundary on $ROCOV - \Delta V$ plane [3]

Appendix C

Development of IBR Models for Protection Studies

C.1 Introduction

This Appendix provides an overview of the IBR models developed to assess the sensitivity and security of the proposed Relative Speed (RS) based loss of synchronism protection scheme. The performance of generic IBR models were evaluated through fault ride through and immediate post fault behaviour.

C.2 Development of IBR Models

The dynamic behavior of IBRs can generally be divided into two primary categories: fully decoupled systems and partially decoupled systems [79]. Fully decoupled systems, such as those utilizing full converters, completely isolate the generator's me-

chanical dynamics from the grid through the power electronic interface. This allows for precise control over active and reactive power, independent of the grid conditions. An example of this type is a Type 4 wind turbine generator (WTG).

In contrast, partially decoupled systems, such as Type 3 doubly-fed induction generators (DFIGs), maintain a partial connection between the generator and the grid. The rotor of the DFIG is interfaced with the grid through a back-to-back converter, while the stator is directly coupled to the grid. This configuration allows for some level of control over the generator's operation but still retains a degree of dependence on grid dynamics.

Given these distinct characteristics, both Type 4 and Type 3 WTG models were selected to be used in protection validation studies. The following sections detail the modelling of these devices.

C.2.1 Doubly-Fed Induction Generator (Type 3) Wind Turbine Model

A high-level diagram depicting the interconnection of various controllers within the DFIG system is presented in Figure C.1. Type 3 wind turbine generator (WTG) controllers utilize d-q axis vector control to achieve accurate and efficient management of active and reactive power. The model includes both inner and outer current control loops, along with a novel discrete Fourier transform (DFT)-based phase-locked loop (PLL) described in Section C.3. Power dispatch signals for the WTGs are generated by the generic plant power controller (PPC) model, as outlined in Section C.4. All

controller components were implemented in PSCAD/EMTDC using a combination of standard control blocks and custom-developed Fortran routines.

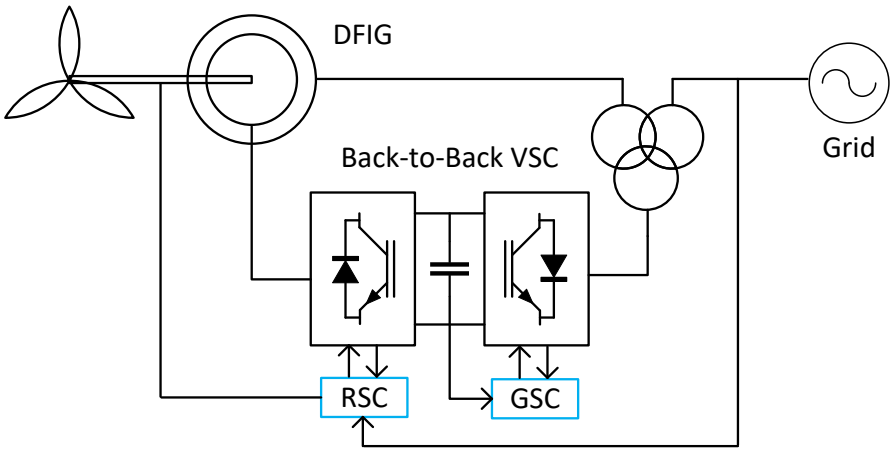

Figure C.1: Schematic of the doubly-fed induction generator based wind turbine system (Type 3) [4]

C.2.2 Full Converter (Type 4) Wind Turbine Model

A high-level schematic illustrating the connection between various controllers in the Type 4 WTG system is shown in Figure C.2. Vector current control is the primary control methodology used for regulating active and reactive power in a Type 4 wind turbine. Similar to Type 3 WTG model, this model also incorporates inner and outer current control loops, and the same novel DFT based PLL discussed in Section C.3. The power dispatch commands for the WTGs were issues by the generic PPC model discussed in Section C.4). Each controller was modelled in PSCAD/EMTDC using a combination of generic control blocks and custom Fortran codes.

During grid faults, vector control enables inner current loops (based on low voltage

ride through (LVRT) threshold settings) to provide reactive current to support grid voltage. This is achieved through a k Factor-based current injection scheme. For the protection validation studies, the k factor was set to 2, meaning that a 50% voltage drop would initiate maximum reactive current injection. Additionally, the system may temporarily reduce active power generation to prevent overcurrent and safeguard the IGBT switches.

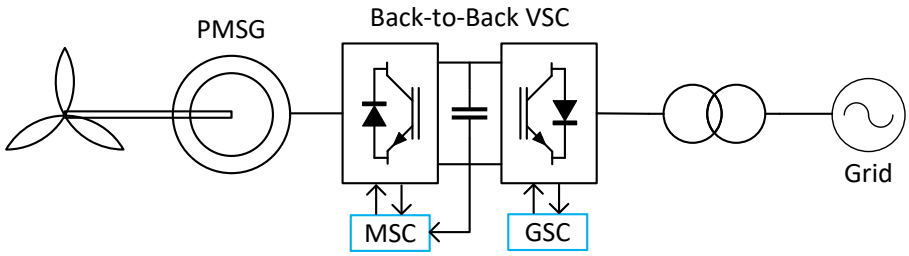

Figure C.2: Schematic of the permanent magnet synchronous generator (PMSG) with full converter wind turbine system (Type 4) [5]

C.3 DFT Based Phase Lock Loop (PLL) Model

One of the key component of the grid side controller is phase lock loop (PLL). The PLL is primarily used to synchronize the internal control of the inverter or generator with the grid voltage. It ensures that the generated power aligns with the grid's frequency and phase, enabling stable and efficient operation.

Grid disturbances, such as severe faults, harmonic distortion, or unbalanced voltages can affect PLL performance, leading to inaccurate phase tracking, specially in weak systems where loss of synchronism phenomena is commonly observed. In weak

grid scenarios (low short-circuit ratio), the grid impedance can vary significantly, causing the PLL to experience stability issues or fail to track the phase correctly. Weak grids are also prone to harmonic distortion, voltage fluctuations, and frequency instability, which worsen PLL performance issues.

Therefore, a PLL design based on Discrete Fourier Transformation (DFT) in aircraft electrical systems presented in [6], is implemented in PSCAD/EMTDC to achieve better performance. A block digram of this Novel PLL algorithm is illustrated in Figure C.3 and C.4. The DFT algorithm determines the amplitudes of three consecutive frequency domain components, which are utilized to estimate the frequency error. A PI controller is then applied to reduce the frequency error and compute the fundamental frequency. The estimated frequency is integrated to derive the phase of the fundamental component, which is subsequently fed back into the DFT algorithm for continuous refinement.

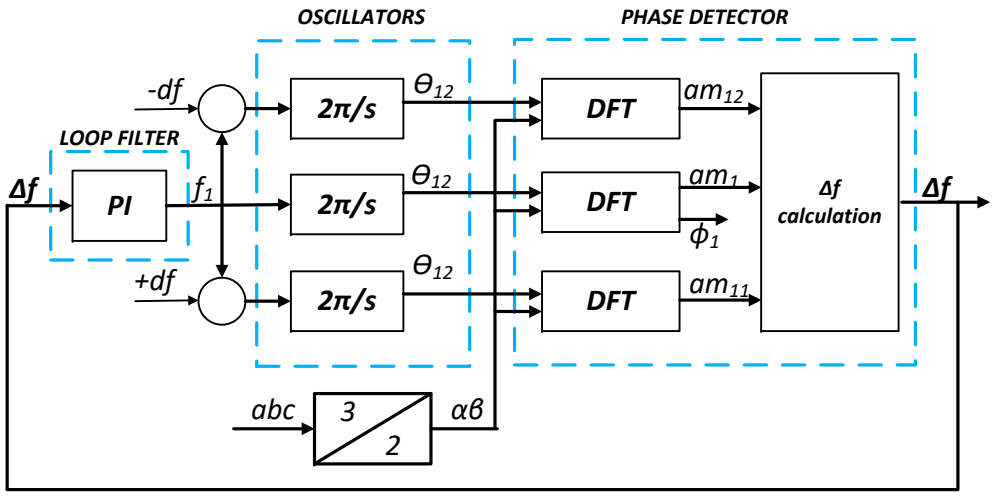

Figure C.3: Novel DFT based PLL algorithm [6]

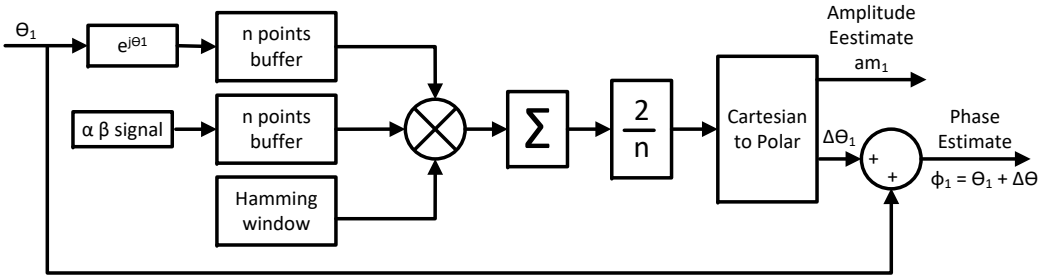

Figure C.4: Calculation of the DFT component am_1 and phase ϕ_1 in Figure C.3 [6]

This DFT based PLL algorithm operates on the principle that the fundamental component of a signal exhibits the highest amplitude in the frequency domain. If the exact fundamental frequency is not known, it can be identified within the constraints of frequency resolution by locating the highest amplitude in the voltage spectrum and determining the frequency associated with it.

In an electrical power system, where the frequency is typically approximately known, an initial estimate f_1 can be chosen. Based on this initial guess f_1, it is possible to estimate Δf, which represents the difference between f_1 and the actual fundamental frequency. The estimation of Δf relies on the amplitudes of three spectral components [80]: the component at f_1 and the two adjacent components at each side $f_1 \pm df$, where df represents the frequency resolution of the DFT. The calculation of Δf is given in (C.3.1).

$$\Delta f = \frac{1.5 \cdot df \cdot am_1 \left(am_{11} - am_{12}\right)}{\left(am_1 + am_{11}\right)\left(am_1 + am_{12}\right)} \tag{C.3.1}$$

where;

$$am_1 = \text{amplitude of the spectral line at frequency } f_1 \tag{C.3.2}$$

$$am_{11} = \text{amplitude of the spectral line at frequency } f_1 + df \tag{C.3.3}$$

$$am_{12} = \text{amplitude of the spectral line at frequency } f_1 - df \tag{C.3.4}$$

The value Δf is then used as an error signal for the PI controller that gives the estimated value of the fundamental frequency. The estimated frequency is then utilize to obtain the phase of the fundamental signal, and this is used to calculate the three amplitudes $am1$, am_{11}, and am_{12} using the DFT algorithm.

This model was implemented as custom Fortran code in PSCAD/EMTDC to enable efficient computations and was integrated into the current vector control framework to supply the phase angle reference required for ABC to DQ0 transformations.

C.4 Power Plant Controller (PPC) Model

Power Plant Controllers (PPCs) play a critical role in modern renewable energy systems, including wind, solar, and battery energy storage systems, as their dynamic behaviour greatly impacts the interaction between these plants and the power grid. While PPCs generally operate with slower response times compared to inverter-level controls, their influence on fast transients is minimal. However, the time constants of PPCs align closely with typical power swing frequencies in a system, which range from 0.1 Hz to 2 Hz. Consequently, accurately modelling of PPCs is essential for conducting reliable loss of synchronism protection validation studies.

The generic REPCA1 PPC model available in PSS/E [7] was implemented in PSCAD/EMTDC to represent the power plant controller. Figure C.5 illustrate the active and reactive power control algorithms utilized in the REPCA1 PPC model. The PPC model provides reference commands for active power (Pref) and reactive

power (Qref) to individual generators, ensuring active power delivery and voltage regulation at the POI.

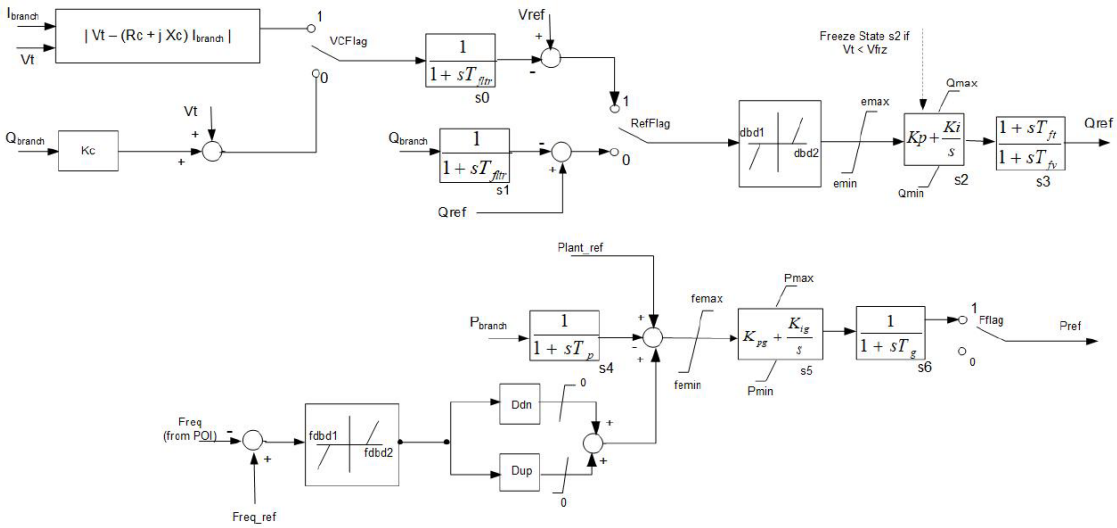

Figure C.5: Active and reactive power control algorithms of the main power plant controller (PPC) implemented in PSCAD/EMTDC based on PSS/E generic renewable plant control model REPCA1 [7]

C.4.1 Reactive Power and Voltage Control

REPCA1 PPC model can operate in different reactive power control modes, including:

1. Voltage control mode with droop: maintains the voltage at the POI by adjusting reactive power.

2. Reactive power control mode: directly regulates the reactive power output of the plant.

For protection validation studies, voltage control option is utilized with 4% voltage droop. Measurement filtering, dead bands, error limits, freeze states during Fault Ride

Through (FRT) and lead lag components are incorporated in the reactive power path in addition to proportional-integral (PI) controller to ensure smooth and accurate control. Reactive power algorithm is implemented in PSCAD/EMTDC using generic control blocks.

C.4.2 Active Power and Frequency Control

REPCA1 PPC model control the plant's active power output by adjusting the power dispatch level of individual units. Active power control function comprise with different features including:

1. Frequency Response: modulates active power response based on grid frequency changes.

2. Ramp Rate Limitation: limit the rate of change of active power outputs, preventing sudden changes that could affect both grid and IBRs.

For protection validation studies, frequency response of the controller was enabled with 4% droop. Similar to reactive power control algorithm, measurement filtering, dead bands, error limits, freeze states during FRT and lead lag components are incorporated in the active power path in addition to PI controller to ensure smooth and accurate control. Active power algorithm is implemented in PSCAD/EMTDC using generic control blocks.

C.4.3 Dynamic Response of Generic IBR Models

The control parameters of the generic WTG models (described in Sections C.2.1 and C.2.2), the novel DFT-based PLL model (detailed in Section C.3) and the generic PPC model (described in Section C.4), were adjusted to obtain overall realistic dynamic response. These performance tests were conducted using a single machine infinite bus (SMIB) system, where the grid was represented by a Thevenin equivalent with a short circuit ratio (SCR) of 4 and an impedance angle of 85°.

Various scenarios were analyzed, including different fault types, fault impedances, fault durations, and combinations of active and reactive power dispatch levels. Figures C.6 through C.11 illustrate the response of active power, reactive power, and voltage at the POI for three selected scenarios.

1. Scenario 1: A temporary 3LG impedance fault at the POI (retain voltage at the POI is approximately 0.5 pu) with 1s clearing time
2. Scenario 2: A temporary bolted 2LG fault at the POI with 1s clearing time
3. Scenario 3: A temporary bolted 3LG fault at the POI with 1s clearing time

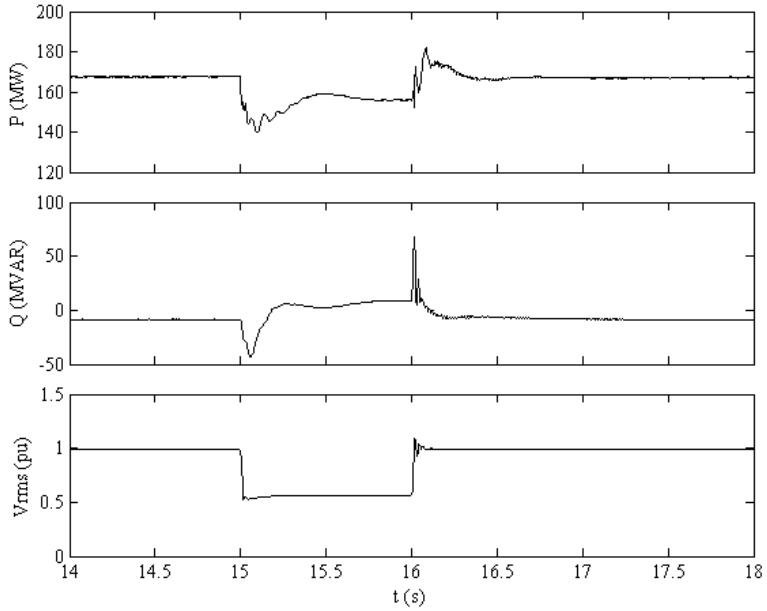

Figure C.6: Active power, reactive power, and RMS voltage at the POI of the generic Type 3 WTG model for a 3LG impedance fault (scenario 1)

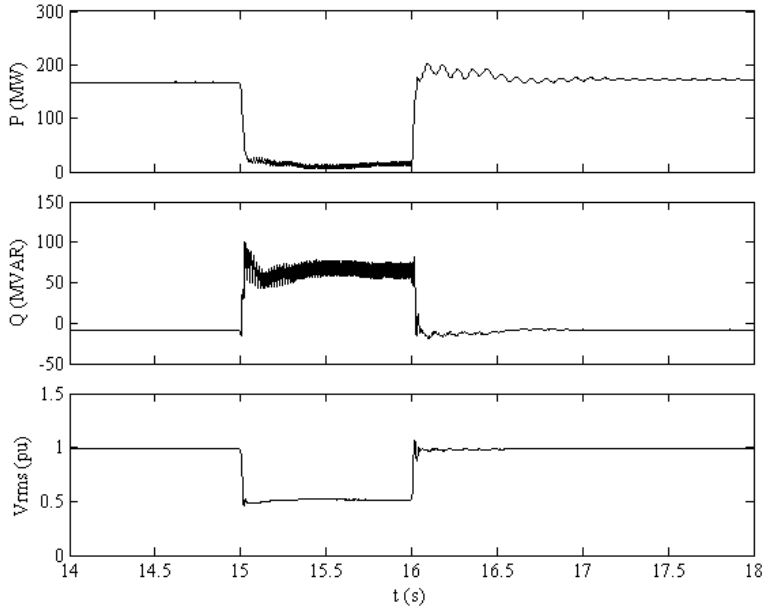

Figure C.7: Active power, reactive power, and RMS voltage at the POI of the generic Type 3 WTG model for a bolted 2LG fault (scenario 2)

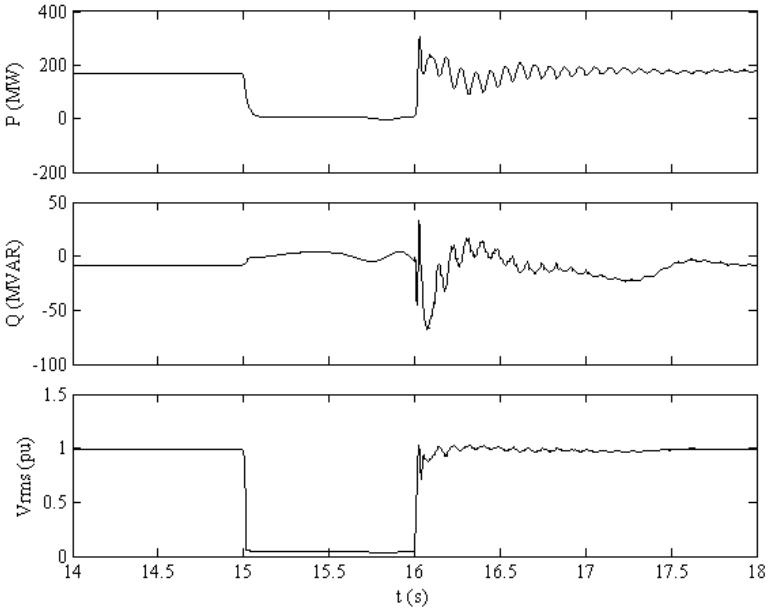

Figure C.8: Active power, reactive power, and RMS voltage at the POI of the generic Type 3 WTG model for a bolted 3LG fault (scenario 3)

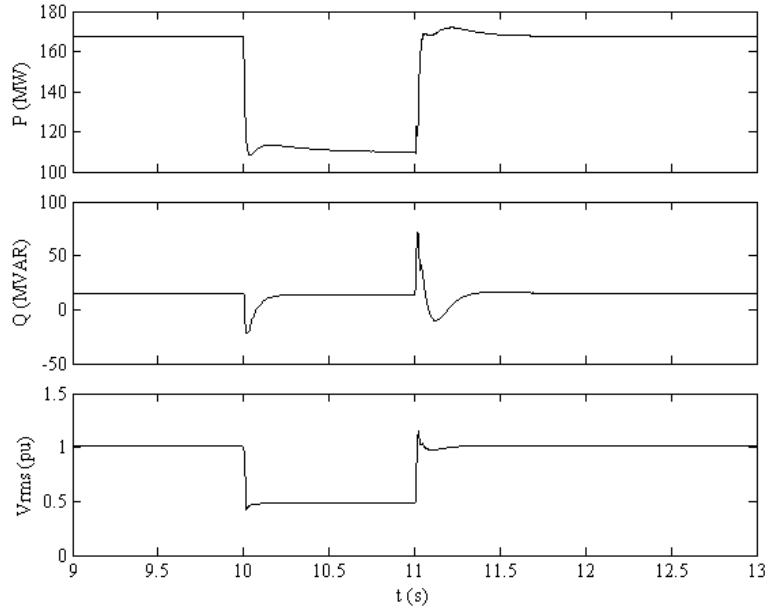

Figure C.9: Active power, reactive power, and RMS voltage at the POI of the generic Type 4 WTG model for a 3LG impedance fault (scenario 1)

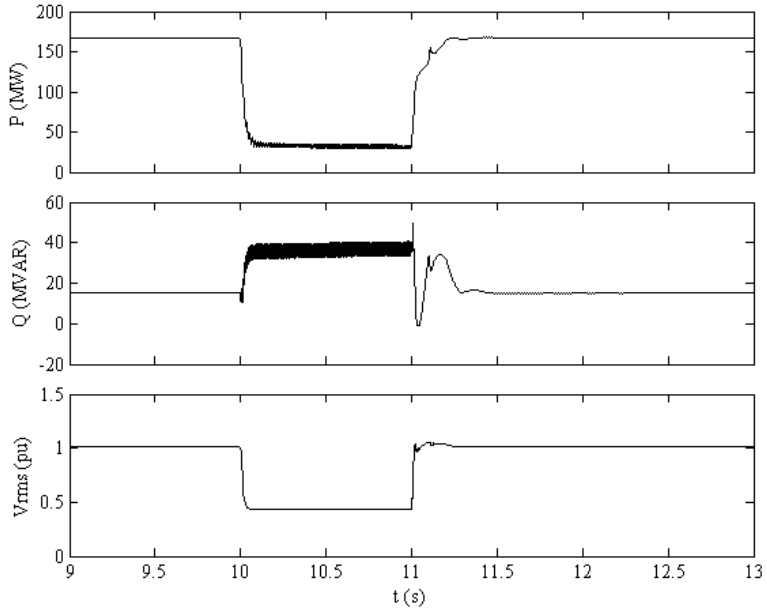

Figure C.10: Active power, reactive power, and RMS voltage at the POI of the generic Type 4 WTG model for a bolted 2LG fault (scenario 2)

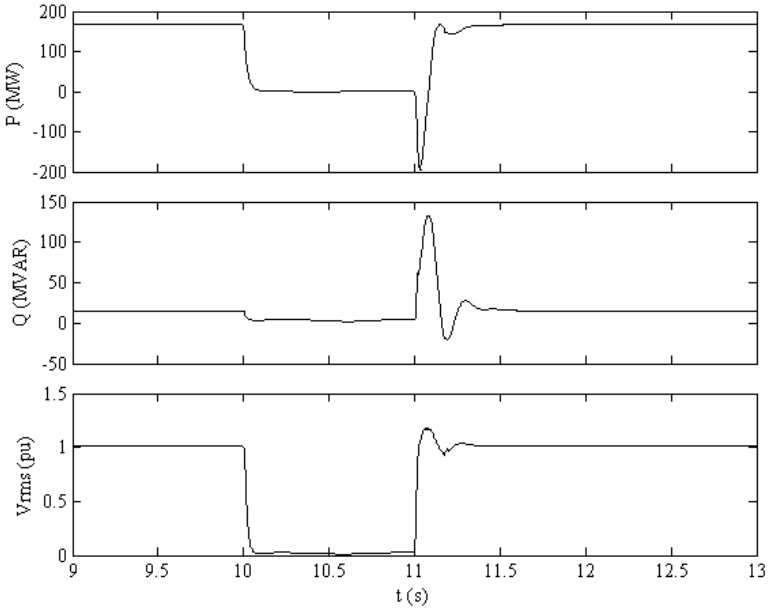

Figure C.11: Active power, reactive power, and RMS voltage at the POI of the generic Type 4 WTG model for a bolted 3LG fault (scenario 3)

The results presented in the above figures demonstrate that the generic WTG

models achieved satisfactory performance across all three operational stages: pre-fault, during the fault, and post-fault periods. The models were able to replicate realistic dynamic behaviours under various test scenarios.

However, some minor issues were observed, particularly in the transient response during fault conditions. These issues may be attributed to generic implementation of WTG controls, parameter tuning, or the inherent simplifications in the generic model compared to the commercial devices. For instance, the transient overshoot, settling time, or harmonic content may exhibit slight deviations, which could impact the accuracy of the generic model's performance under specific grid conditions.